UNIVERSITÀ DEGLI STUDI DI PARMA

DOTTORATO DI RICERCA IN SCIENZA E TECNOLOGIA DEI MATERIALI INNOVATIVI

Realization and Characterization of CZT X-Ray and gamma ray detectors

Laura Marchini

Coordinatore:
Prof. Anna Painelli

Tutor:
Dott. Andrea Zappettini

XXIII Ciclo - Gennaio 2011

Contents

Acknowledgments

First and foremost I would like to express my gratitude to my supervisor, Dr. Andrea Zappettini, for all his guidance and support throughout my student career. I was always amazed how he was able to took out some time of his busy schedule to discuss with me about the direction my research should take and encourage me in the experiments.

I would also like to thank the other members of my research group: Dr. M.Zha, Dr. D.Calestani, Dr. L.Zanotti, Dr. M.Zanichelli, Dr. M.Pavesi, Dr.E. Gombia and Dr. R.Mosca. I would also like to express my thank to the other students of the group who have all been a fundamental part of my graduate studies: Dr. N. Zambelli, Dr. G. Benassi and Dr. M. Villani, they were always there whenever I needed help.

I would like to acknowledge the help from the detector group of Dr. E. Caroli at INAF-IASF in Bologna for for their support and guidance during my work. I would like to express my sincere gratitude and appreciation to all the research group and especially Dr. N.Auricchio and Mr. A.Donati.

I would like to express my gratitude to Dr. R.James for giving me the opportunity to work with his team of talented scientist at BNL. Many thanks are due to Dr. A.Bolotnikov, Dr. G.Camarda, Dr. K.H.Kim, Dr. R.Gul, Dr. A.Hossain, Dr. G.Yang and Dr. Y.Cui. I am also thankful to Ms. B.Roland for helping me with all the paperwork.

Finally, I would like to extend my greatest appreciation to my family, my parents Dante and Daniela and my brother Luca, and my boyfriend Giacomo for their understanding and support.

CHAPTER 1

Introduction

Radiation detection is a very important tool for every application field that includes monitoring and detection of radiation sources. In the case of gamma and X-ray detectors, a wide number of application fields are involved in the detector developing, this list comprehends medical imaging, environmental monitoring, homeland security and astrophysics. Several detector technologies have been developed during recent years: proportional counters, scintillator detectors, photomultipliers and semiconductor detectors.

The radiation detector device has the specific objective to deliver information about the energy deposited by the incident radiation, the position of the radiation interaction, or about the time at which the radiation has arrived. Semiconductor detectors offer some advantages over the other technologies developed for this applications. The density, for example, is orders of magnitudes higher with respect to phototubes or scintillators, corresponding to a much higher stopping power for semiconductor based devices. Moreover with a semiconductor detector, unlike the photomultiplier tube, the radiation energy is directly converted into the signal. This involves an improvement in the energy resolution due to the large number of carriers generated for every event occurring inside the medium and hence a higher photo-sensibility.

For many years the high energy radiation detection field was dominated by Si and Ge. These two materials are able to produce devices with a very high energy resolution and the corresponding read out electronic was already developed. However the use of these material requires a cooling down to cryogenic temperatures, usually at liquid nitrogen (77 K). The need of making a device able to work at room temperature has pushed the research in the direction of

the exploitation of a new class of semiconductors characterized by a high and direct energy gap. Among semiconductors CdZnTe has emerged as a particularly suitable material in the realization of efficient detectors. CdZnTe owns many characteristics that make it particularly interesting for the radiation detector realization:

- A large band gap 1.6 eV, to permit room temperature operations
- High resistivity, that ensures low leakage current at high voltages
- A small pair creation energy, having a large amount of charge carriers to be generated and hence a high photosensitivity
- A high atomic number for a good radiation stopping power. The stopping power is proportional to a power of the atomic number: Z^n, n=4-5. CZT is effective as detector up to 1 MeV. This ensure also a high photoelectric absorption up to high energies
- Good transport properties to collect a large number of carriers, this is particularly true for electrons

CdZnTe is not the only material that was considered for the realization of room temperature devices.

Thallium Bromide (TlBr) and Mercuric Iodide (HgI_2) have both produced very efficient devices, with good energy resolution and high resistivity. However these two materials suffer from sever limitations. One one side they are both very hard to growth with a high single crystal rate. Secondly, they suffer for some problems intrinsically bounded to the device functioning. HgI_2 is highly unstable in air environment and requires a full encapsulation to preserve the device properties. TlBr is highly toxic and the applied bias causes a migration of Br atoms inside the polarized device. However CZT material suffers from some shortcomings that limit its wide spread use especially for large volume devices. One of the main drawbacks is the poor mobility of holes that results in a incomplete charge collection, this affects the spectral resolution producing a tail in the low energy side of the photopeak. Nowadays the hole degradation is limited by the realization of geometries that create a single carrier device. Crystal growth is another challenging field in the development of a large scale production of CZT devices. Obtaining a completely single crystal ingot is still difficult and also a high homogeneity of the characteristics is still not obtained.

Unlike other materials with a longer history, like Si or Ge, the electrode technology is still not completely developed. Several metals are currently studied for the realization of a stable, reproducible and low leakage current metal-CZT interface. The electrodes should not introduce polarization when biased

and produce a uniform electric field. An ideal metal contact would prevent any charge build up, in order to have a more uniform electric field profile.

Applications of CdZnTe as a radiation detector

Nowadays there is a large number of fields where CdZnTe can be employed as a X-ray and gamma ray detector. These include the medical imaging (SPECT, CT), homeland security (cargo and luggage control), environmental monitoring (control of the background radiation) and astrophysics (study of the X-ray emission of celestial bodies). Industrial research have recently discovered the potential of this material, and began to produce large scale devices based on this large band gap material that can operate at room temperature. CdZnTe properties make it a particular appealing material for the realization of portable and easy to handle devices, unlike other materials, like Si, that require cryogenic cooling. One of the fast growing application fields is the homeland security. The increasing fear of terrorist attacks related to airplane security, the constantly increase of the volume of traveling people and object shipping all over the world, made it a must to create a radiation device able to produce a fast and accurate response. Because of the importance of the traveling safety, this field has recently gained a lot of interest and attracted several financial supports. Body and luggage control find a huge market in the airport scanning equipment, and especially in this field, considering the number of people flying everyday from the main airports, the need of a response within a few second is necessary. The use of a highly sophisticated device, like CZT based detectors, reduces also the dose necessary to detect dangerous object in a luggage or on the passenger body (body scan). A second, but equally interesting application field is in the medical imaging area. The use of solid state devices reflects in the production of new medical devices, with far higher performances with respect to scintillators or other devices. SPECT (Single Photon Emission Computed Tomography) or CT (Computed Tomography) are techniques that are becoming more and more common in the preventative medicine or surgical applications and the use of such devices have been a great help in the cure and detection of diseases. Environmental monitoring is currently performed using Geiger Mueller counters, with this equipment it is not possible to acquire information about the nature of the contamination and the position of the X-ray source. The monitoring consist in two main types of applications: i) the control of the background radiation, controlling the natural X-ray emission by elements present in the soil and ii) the monitoring of the areas in the proximity of nuclear facilities, where the possible poisoning due to a malfunctioning of the facility needs to be controlled constantly. This field is of particular in-

terest in Italy today because of the possibility to build new nuclear sites on the Italian territory. With respect of other applications, astrophysics is more related to the academic research instead to the industrial production, but is as well interesting. CZT has always been a focus material in the detection of X-ray emission in the space. Astronomical equipment to be sent in the stratosphere or above, found it necessary to reduce the dimensions of the detection packet and to improve the photo-sensitivity of the device, in order to acquire the largest amount of information possible. CZT has been successfully used in many European (ESA) and Italian (ASI) flight campaigns.

Aim of this thesis

The aim and fundamental concept of this thesis is to produce a complete characterization and study of the material, in order to give a immediate feedback to the crystal growers of the group and implement the growth technology. For that the realization of devices with good spectroscopic characteristics and to develop a reliable and precise device fabrication technology is necessary, in order to obtain a good characterization of the properties.

The thesis is carried out at IMEM-CNR in Parma, under the supervision of Dr. Andrea Zappettini, head of the IMEM detector group. The IMEM detector group is a crystal growth group, focused on the development of CZT devices. It was therefore fundamental to have an intense feedback between the growth and the behavior of the detectors.

Some of the measurements presented in this work were performed at the Brookhaven National Laboratory (BNL), Upton, Long Island, at the Nonproliferation and National Security group were I have worked as a guest researcher for a 4 months period during the second year of PhD and one month during the third, under the supervision of Dr. R. James and Dr. A.Bolotnikov.

At IMEM, the detector preparation is followed in every single part of the technological process. Starting from the ingot, several slabs, slices cut along the growth axis, and wafer, cut perpendicular to the growth axis, are obtained and analyzed, in order to study the material homogeneity in both directions. During the thesis research period over 20 ingots were grown and all of them were deeply studied. This accurate study allowed the group to reach a lot of progress in these years, comprehending a strong improvement in the purity of the starting elements, an amelioration of the spectroscopic quality (energy resolution and reproducibility of the detector response) and higher transport properties. The contact deposition and the surface preparation treatments were

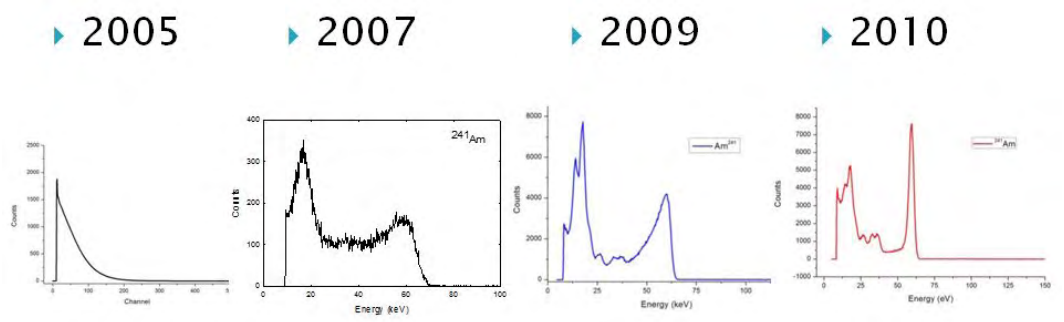

Figure 1.1: Evolution of the IMEM CZT detector response in presence of a ^{241}Am source

all studied for the obtaining of a low noise current-voltage characteristic, also for high voltages. This improvement is shown in the time-line, figure1.1 of the detector response to an uncollimated ^{241}Am X-ray source.

More then 100 samples were cut, polished and prepared. All of them were studied, the combination of all the information obtained with different studies allowed a better comprehension of the mechanisms of operation of the devices.

The first part of this work consist in the study of the as grown material. The ingot homogeneity is analyzed by means of the PL (Photo Luminescence) mapping, the near band gap emission is connected to the Zn concentration. By mapping the position of the peak in every point it is possible to reconstruct the Zn segregation profile. From the tip to the bottom of the crystal the ingot characteristics can vary and give completely different results in the final device. The PL mapping was also found to be extremely useful in the comprehension of the mechanisms occurring in the early stages of the nucleation. It was in fact found an unexpected behavior in the Zn profile, that suggests a poor control of the nucleation site inside the ampoule. The same behavior was found in several publication from a large number of groups that grow CZT ingots. The study of the material comprehends also the analysis with an IR (Infra Red) microscope of the most common secondary phase present in the CZT lattice, Te inclusions. The inclusions are present inside of the crystal structure because the excess of Te is trapped during the growth as droplets forming a Te rich secondary phase. The role of this inclusions on the functioning of the final device has been discussed longly in the literature, but currently it is assumed that Te inclusions have an active role in degrading the detector response, the broadening effect in the photopeak is related to the position inside the device and the dimension of the inclusion itself. This degrading mechanism was supported also by theoretical models. For this reason to have

a complete reconstruction of the density and the distribution inside the device of Te inclusions is very important to select the regions for the realization of high quality devices inside a large wafer. The measurement presented in this work were done in BNL, where two optical setup are available for the acquisition of IR images. It is however important to underline that, recently, also IMEM has developed a software for the identification, count and 3D reconstruction of the position of Te inclusions. Another important measurement that was done in BNL at the National Synchrotron Light Source (NSLS) is the white beam X-ray diffraction topography (WXDT). With this technique is possible to map the extended defects present inside a device. Extended defects like dislocations, grain boundaries and twins are locally degrading the detector response. In the case of a device with small pixels this means that some of them are not responding, giving a complete lack of signal. In a single electrode device the effect of the defects is summed to the overall response and can be detected as a prominent tail on the low energy side of the photopeak.

The second part of the thesis is focused on the comprehension and the study of the detector prototypes obtained from the grown ingots. The detector group in Parma owns the know how necessary to realize a completely functioning radiation detector starting from the bare cut wafers. The results obtained on the fabricated devices were used to improve the growth technology. The samples studied were cut in dimensions of about 7 x 7 mm^2 with a thickness varying from 1 mm to 4 mm. After a preliminary study of the current voltage characteristic to determine the resistivity and hence the possibility of the sample to operate at RT.

The spectroscopic response was studied at INAF-IASF, Bologna, where I had open access during the entire duration of the PhD. The measurements were performed under the supervision of Dr. E. Caroli and Dr. N. Auricchio. The The investigation was done with several standard X-ray sources: ^{241}Am, ^{109}Cd, ^{57}Co and ^{133}Ba. The experimental setup comprehends a charge sensitive preamplifier, the voltage supplier, an amplifier and the MCA. The samples were studied varying the applied voltage and varying the amplifiers settings. The detector spectroscopic response was also studied on a micron scale, at the NSLS. A X-ray beamline is dedicated to the study of the device punctual response. The setup allow a collimation of the beam down to 10 x 10 μm. The correlation of the results obtained with the ones others techniques was extremely useful in the determination of the role of defects in the detector functioning.

Another important parameter studied in BNL was the $\mu\tau$ (mobility-life time) product, that determines the transport properties of the material. The measurement of the $\mu\tau$ product is usually done by observing the shift in channel number of a X-ray emission with the applied voltage. The resulting data are fitted with the Hecht equation and the $\mu\tau$ product can be calculated for both charge carriers. The study resulted in a monotonous increase in the detector quality during the period of the thesis, the energy resolution ameliorated and the reproducibility of the good results was improved. Some collaboration were started, the electric field profile was studied by Dr. A. Cola, at IMM, Lecce, by means of the Pockels Effect, an electro-optical technique that permits to correlate the intensity of the electric field with the birefringence of the material. The metal-CZT interface and the presence of damaged layers under the electrode was studied in collaboration with Dr. E. Perillo and Dr. A. Raulo, at University Federico II, Naples. Two different techniques were combined the RBS (Rutherford Back Scattering) and XRF (X-Ray Fluorescence), the presence of multiple layer under the deposited electrodes was reported, the thickness of the deposited metal layer was also measured.

Thesis outline

For a practical convenience the experimental results were divided into two chapters, called material characterization and device characterization. The separation of the two is only finalized to a more practical organization of the results and data, but they are both aimed to the comprehension of the mechanisms dominating the device functioning and the measurement of the material characteristics, in order to push together all the results and improve the crystal growth. The device characterization contained the results obtained on the samples with deposited metal electrodes, the material characterization comprehends the data measured on the as grown material (polished and lapped, but with no device technology on it).

- Chapter 2: Material properties: contains a brief introduction to the material and provides information about structural properties, electronic structure, an overview of the main dopants used in the realization of X-ray detectors and the list of the most common defects present in the material.

- Chapter 3: Material and device characterization: theory and setup description of the characterization techniques presented in this work. The

used techniques are photoluminescense and PL mapping, white beam X-ray diffraction topography

- Chapter 4: Experimental results: Material characterization. As explained before, these last two chapters are part of the same concept, but divided for a better organization of the data. In this part the results obtained with PL mapping, X-ray diffraction topography and IR microscopy are shown.

- Chapter 5: Experimental results: Device characterization. This chapter contains the measurements done on the prepared prototype devices. The obtained results comprehends the IV measurements, the spectroscopic results, with uncollimated sources or with the X-ray response map setup, the $\mu\tau$ product measurement and the study of the electric field uniformity by means of the Pockels effect.

CHAPTER 2

THEORY: MATERIAL PROPERTIES

2.1 CdZnTe properties

2.1.1 Structural properties

Cadmium Zinc Telluride (CZT) is a semiconductor, it belongs to the commonly called II-VI group. Cadmium (Cd) and Zinc (Zn) are in the IIB group, while Tellurium (Te) is in the VI group. These three elements are characterized by a high atomic number: Cd is 48, Zn is 30 and Te is 52. Those numbers are quite high in between semiconductors. CZT structure is zincblende (figure 2.1). The crystal structure is formed by two Face Centered Cubic (FCC) shifted along the cube diagonal by a quantity equal to the fourth part of the diagonal itself. Every sub-lattice is respectively composed by all Te or all Cd atoms (or Zn according to the composition). This not centered crystalline structure implies the lattice planes 111 to be composed by one element only, this will be important during the fabrication processes of the detector, in particular this influences the properties of the metal contacts, that may change transport properties from one side to the other. The unit cell contains 4 atoms of Cd and 4 atoms of Te. The zincblend is the stable structure at atmospheric pressure and room temperature, but at high pressure conditions, 35 Kbar at room temperature, the structure changes from zincblende to wurtzite (hexagonal) [1]. Being CdZnTe an alloy, it is important to be accustomed to the common notation: $Cd_{1-x}Zn_xTe$, where x is the Zn molar fraction ranging from x=0 that correspond to CdTe and x=1, corresponding to ZnTe. It's possible to obtain, and hence to grow, solid CZT with every Zn composition.

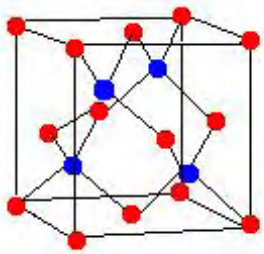

Figure 2.1: The zincblende structure for a binary compound. Different atoms are painted with different colors, the figure can easily be extended to a 3 component system (CdZnTe) considering the third atom replacing one of the species.

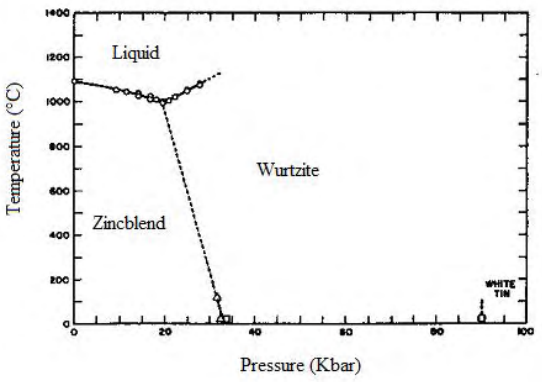

Figure 2.2: Temperature-pressure projection of CdTe state diagram [1].

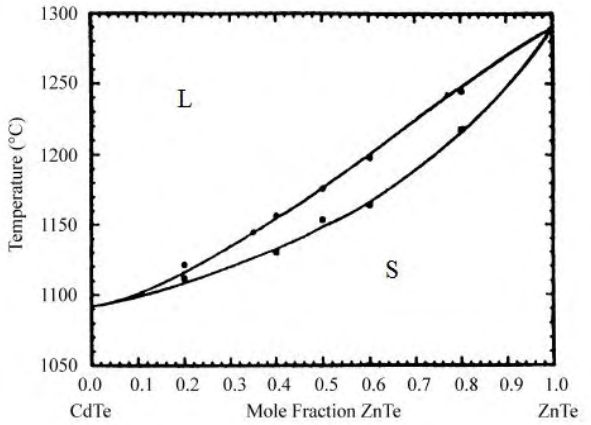

Figure 2.3: Solidus-liquidus pseudobinary diagram. Experimental point are from [8] and [9].

The use of CZT as a gamma and X-ray detector material implies usually a Zn composition in the range from x=0.05 to x=0.2, higher Zn fraction are commonly employed for the realization of IR windows. The lattice constant (a) depends on the stoichiometry of the semiconductor following the law:

$$a(x) = a_1(1 - x) + a_2(x) \tag{2.1}$$

where a_1 and a_2 are the lattice constants of CdTe and ZnTe, respectively. The average lattice constant can be determined by simple X-ray diffraction using Bragg's law. The lattice constant value for a CZT ingot of composition $Cd_{0.95}Zn_{0.05}Te$ is $a = 6.465$ Å[34].

2.1.2 Band structure

The band structure of CZT is a delicate issue. With the ternary compounds, in fact, the condition of periodicity is not satisfied, because of the local composition fluctuation. It can be a good starting point to study the band structure of CdTe and ZnTe: they are both direct bandgap semiconductors and their bandgaps at room temperature are 1.5 eV and 2.2 eV [10] respectively. To study the band structure of CdTe (in figure 2.4) is not too different from studying CZT. The band structure of ZnTe is qualitatively similar. The lines in the image are calculated using the pseudopotential method [3]. There are 4 valence bands, containing the 8 valence electrons of the unit cell. The heavy and light holes band and the degeneracy in k=0 of the split off band is removed by the spin-orbit interaction [4]. An important value that can be extracted from the band structure is the effective mass of holes and electrons.

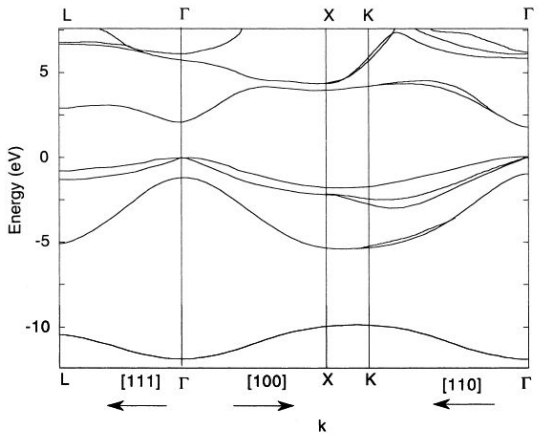

Figure 2.4: Band structure of CdTe calculated by the pseudopotential method [3]

Let us consider again the band diagram of CdTe. The constant energy surface is spheric, meaning that every value can be obtained from the reciprocal of the curvature in the k space, at k=0. Both CdTe and ZnTe have relatively low effective masses for electrons: $0.11m_0$ and $0.15m_0$ [10]. For holes, because of the separation in the valence band, there are more effective masses. In literature the values are 0.70 for heavy holes and 0.103 for light holes [7]. A common approximation for the CZT band structure is to consider the structure of the two binary semiconductors (CdTe and ZnTe) and made a linear approximation of the two characteristic, this technique is called virtual crystal approximation [5]. However this approximation is not very effective in the definition of the relationship between band gap and composition, in fact from this calculation, the dependence of E_g from the composition should be linear. In practice, it is always found to have a quadratic curvature. The coefficient of the quadratic term is the bowing parameter, and it is commonly associated with short-range disorder [6]. In table 2.1 some CdTe electronic constant are listed, those values can be used for CZT especially when the Zn content is near 0.1.

2.1.3 Defects and dopant impurities in CZT

A semiconductor crystal is often assumed to be a perfect periodic structure of atoms, real semiconductors however encounter many deviations from the ideal case. The most common deviation types are foreign impurities and structural defects. The use of semiconductor crystals in high tech applications implies a deep study and a strong control on lattice disorder. The number and type of defects present in the lattice structure influence the optical and electrical properties of the material. Those properties in fact depend on the localized

Table 2.1: Principal electronic properties of CdTe and ZnTe

CZT electronic characteristics	
Electronic effective mass: m^*_e/m_0	$0.11m_0$ (CdTe) $0.15m_0$ (ZnTe) [10]
Light hole effective mass: m^*_lh/m_0	$0.103m_0$ (CdTe) $0.154m_0$ (ZnTe) [7]
Heavy hole effective mass: m^*_hh/m_0	$0.7m_0$ (CdTe) $0.63m_0$ (ZnTe) [7]
ΔE between L and Γ in the conduction band (eV)	0.29 10^{-4} T (CdTe)

defect in the forbidden gap. The presence of extended defects, like dislocations, and their movement have instead influence on the mechanical properties [13]. A deep understanding of the role of dislocations on the crystal properties is very important, in fact it is extremely challenging to obtain a dislocation-free crystal. The causes that lead to the creation of dislocations are many, i.e. the collapse of point defects or the high thermal gradient at the solid-liquid interface. Seitz realized a complete classification of defects in 1952 [14] and it counts nine different kinds of defects. Here only the ones who have relevance on the crystal and device quality will be listed.

Point defects

Point defects can be grouped in:

- Intrinsic point defects: this group includes interstitials, vacancies and antisites
- Impurities: atoms that do not belong to the lattice, they usually act as dopants
- Combination of intrinsic point defects with impurities

In an undoped crystal the only charge carriers are electrons and holes present in the crystal structure. Those carriers fix the filling of the energy levels, but are not adding any additional level. On the contrary, new levels are formed whenever a perturbation in the lattice periodicity is present, those levels may be caused by a vacancy (vacant atom sites) or interstitial (atoms occupying sites which are normally vacant). The presence of these defects, the so called Frenkel defects, originates a set of discrete levels in the energy gap between the valence and the conduction band. In an undoped CZT crystal, the majority of defects is Frenkel kind and concerns Cd vacancies and interstitials. Cd

Table 2.2: Behavior of dopants in CZT, according to their group

Substituted atom	Group of the dopants						
	I	II	III	IV	V	VI	VII
Cd^{II}	A(1)	-	D(1)	D(2)			
Te^{VI}				A(2)	A(1)	-	D(1)

vacancies (V_{Cd}) can give two acceptors levels, V_{Cd}^{-} and V_{Cd}^{2-}, localized in the forbidden gap, they originate from the reactions:

$$V_{Cd} + e^{-} \rightarrow V_{Cd}^{-}$$

$$V_{Cd}^{-} + e^{-} \rightarrow V_{Cd}^{2-}$$

Similarly, Cd interstitial creates two donor levels:

$$Cd_i \rightarrow Cd_i^{+} + e^{-}$$

$$Cd_i^{+} \rightarrow Cd_i^{2+} + e^{-}$$

Another important defect, that strongly influences the electrical properties of the material, is Te antisite (Te_{Cd}). This defect is formed by Te occupying a Cd position in the lattice. Te_{Cd} is responsible of the mid gap level that, acting as a trap, is commonly assumed to be the reason of the high resistivity of CZT ingots. A completely different subject is the dopant impurities. Those atoms are intentionally introduced in the material in order to change the electrical properties. Dopants have the same behavior as structural defects, they introduce one or more levels in the band gap. In table 2.2 is shown the behavior of dopants for CZT, some of them replace Cd atoms, while others Te atoms.

The number between the brackets represents the number of levels generated for every dopant. For CZT dopants belong to group III and VII. Some common donor dopants are:

- Cl: substituent on Te, gives the donor level:

$$Cl_{Te} \rightarrow Cl_{Te}^{+} + e^{-}$$

- In: substituent on Cd originates as well a donor level, via the reaction:

$$In_{Cd} \rightarrow In_{Cd}^{+} + e^{-}$$

The third defect type is the combination of structural defects and dopants. In CZT Cadmium vacancies are often bounded to donor impurities, among all the possible combination the A center is the most famous and most important one. The A center is formed by a cadmium vacancy ionized two times and a ionized donor ($V_{Cd}{}^{2-}$ and X^{+}, being X a general dopant). A-center plays a main role in the auto-compensation theory, it origins a deep acceptor level that compensate the donor levels present in the material due to thermodynamics reasons.

Dislocations

Dislocations are present in CZT crystals as the result of several processes. One cause of formation is the collapse of point defects after cooling down (climb dislocations). Dislocations can also origin from thermoelastic stress relaxation due to large axial and radial thermal gradient at the solidus-liquidus interface during the crystal growth. This is the main dislocation formation process in CZT ingots grown by the Bridgman technique. This dislocations are moving along favorite directions in the crystal (glide dislocations). Inhomogeneities in the crystal composition can cause plastic deformation and hence origin dislocations. Dislocations are responsible of the formation of subgrain boundaries, in fact they are moving to form dislocation aggregates and then subgrain boundaries. Dislocations are most commonly found in crystal parts where the lattice deformation is higher: top and bottom of the ingots, due to a higher presence of impurities or precipitates. It's proved the relation between the dislocation formation and the lattice disorder. The presence of dislocation is alo connected to the presence of Te precipitates. Anyway, the dislocations generated by Te precipitates are just a small part. Dislocation are commonly studied using chemical etching solutions, X-ray topography, cathodoluminescence or a IR microscopy (dislocations originate birefringence in the crystal [20]).

Tellurium precipitates and inclusions

Te precipitates are a secondary phase formed in the CZT matrix in high temperature conditions. They originate from point defects clustering in the matrix. The principal point defects involved are Cd vacancies and Te interstitial. During the crystal growth, the temperature decreases and the Te solubility diminishes leading to the formation of precipitates. The size and distribution of Te precipitates vary considerably with the growth technique and the thermal gradient. The dimension of the inclusions is in the range between a few micrometers up to 50 μm [34]. From IR measurements it has been proved that Te

precipitates are usually associated with the presence of extended defects such as dislocations or grain boundaries. Extended defects act as nucleation points, this behavior leads to the formation of Te decorated defects. The presence of Te inclusions is instead due to instability near the solid-liquid interface. At the interface some Te rich droplets are present, during the growth the interface is moving and the droplets are incorporated in the solidus. Their size is bigger then the one of precipitates, and can reach tens of microns.

2.1.4 Compensation

For the application of CZT crystals as radiation detector material a high resistivity (higher then 10^9 Ω·cm) is required. The electrical characteristics of the crystals can be varied to fit the specific applications by changing the dopant type and concentration and by controlling the presence of intrinsic and extrinsic defects. The introduction of a dopant leads to the formation of levels and complexes. Those levels tend to compensate the material, in fact the excess of Te implies the presence of Cd vacancies. Ionized and doubly ionized Cd vacancies creates shallow acceptor levels in the forbidden gap that have to be compensated by the introduction of a proper dopant. Looking at the most common donor dopants in CZT (Cl and In), they behave almost in the same way, forming two shallow donor levels that don't differ much from each other. The former compensation theory was based on the autocompensation between the donor and acceptors levels. The two principal defects levels involved in the generation of the high resistivity were: for the donor the X^+, formed by a generic donor dopant X, and for the acceptors the V_{Cd}^- and the complex (V_{Cd}^{2-}, X^+). Now this model has been discarded and it's commonly accepted the modified compensation model proposed by Fiederle et al. [15], considering however that also the model proposed by Fiederle is not completely accepted. Some discussions are opened about the concentration of the mid gap level. The scheme of the band gap of CdTe or CZT crystals now the role of a near mid gap deep level is crucial in the obtaining of high resistivity material(figure 2.5), V_{Cd} plays now only a secondary, but necessary, role in the compensation mechanism. The mid gap level is pinning the Fermi level at the center of the forbidden gap. The nature of this level is mostly accepted to be Te antisite, Te_{Cd}, but an absolute identification of this level is still not obtained.

2.1.5 Crystal growth of CZT

The realization of CZT based radiation detectors implies some critical steps. Usually problems arise in the growth of a high resistivity single crystal of a

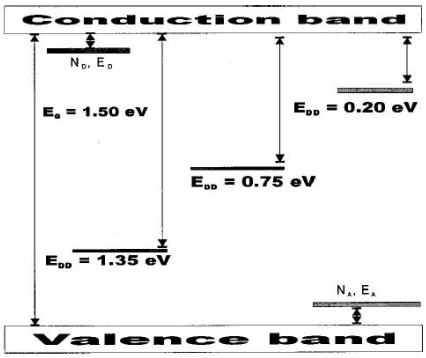

Figure 2.5: The energy gap schema for CdTe:Cl proposed by Fiederle [15]

sufficiently good quality, in order to ensure high efficiency radiation detection. Cutting and polishing are also critical points. The goal is to obtain a single crystal ingot, ideally free from extended defects and with high resistivity, in order to maximize the quantity of material that can be used to realize radiation detectors. For the realization of CZT ingots, many techniques were tried, with alternate success. High resistivity CZT is most often grown through the Bridgman technique. It is a normal solidification growth technique from the melt. The ampoule moves along the growth axis inside the furnace, where a temperature gradient is set, or, alternatively, the ampule is steady and the furnace is moving. Inside the ampule, the starting material lies inside a crucible, the shape of the crucible is expressly studied for a single starting point solidification, in order to reduce the polycrystalline part of the ingot. The Bridgman technique exists in various configurations: vertical Bridgman or horizontal Bridgman, depending on the direction of the growth axis; high pressure or low pressure Bridgman. An interesting variation of this technique is the normal gradient freeze, it consists of a modified Bridgman where a steady ampoule is positioned in a variating temperature gradient. Fundamental components of a Bridgman furnace are plotted in figure 2.6. The ampoule is moving along the growth axis, z axis, surrounded by the furnace wall, crossing the thermal gradient. Choosing the proper crucible is fundamental on the ingot quality, in fact it can be the cause of contaminations (for example it is well known that quartz releases oxygen at high temperature [16]). The crucible size, for CZT growth for research purposes, is usually 2-4 inches in diameter, but some companies are able to grow ingots with diameters up to 8 inches. One common feature of the growth of CZT with the Bridgman technique is the presence of Te precipitates and inclusions. The formation of this separate phase is caused by the decrease of the Te solubility related to the temperature reduction and the

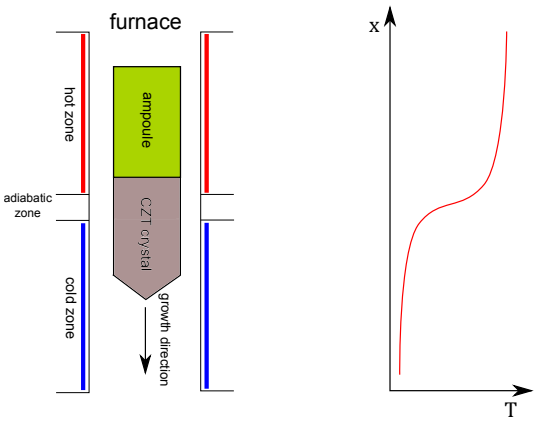

Figure 2.6: Scheme of a Bridgman furnace

contemporaneous evaporation of cadmium at the growth temperature, 1100 °C for Zn=0.1. Spatial distribution of Te inclusions can be disperse or segregated along dislocations or grain boundaries. The two distributions have different effects on the detector properties. In the first case Te inclusions are known to be effective on the charge collection, but have negligible effects on the electrical characteristics. Inclusions segregated along grain boundaries are, otherwise, responsible for the increase of leakage currents, creating lines along the material with lower resistivity with respect of the bulk. This is the reason why, Te inclusions and their effect on the detector performances are so deeply studied and a lot of efforts have been done to reduce the number and the size of the inclusions.

2.1.6 Modified vertical Bridgman technique

Boron encapsulated vertical Bridgman

Crystal growth a CdZnTe ingots at the IMEM-CNR is performed using an innovative Bridgman technique developed in the institute. The technique is basically a vertical Bridgman where the ampoule is not sealed, but the loss of the elements is avoided using an encapsulant (B_2O_3). In order to obtain high quality crystals, CdZnTe is synthesized starting from high purity elements (7N). Direct synthesis of the elements is carried out in high pressure (20-40 atm) of inert gas, all the elements are encapsulated in B_2O_3 [17]. The encapsulation helps to maintain the stoichiometry between the elements. Synthesis is performed in a quartz or Pyrolytic Boron Nitride (PBN) crucible, the elements are covered by solid boron oxide. The melting of B_2O_3 results in a complete encapsulation of the elements, the oxide can be easily removed using de-mineralized water. The synthesized material is then charged in a quartz

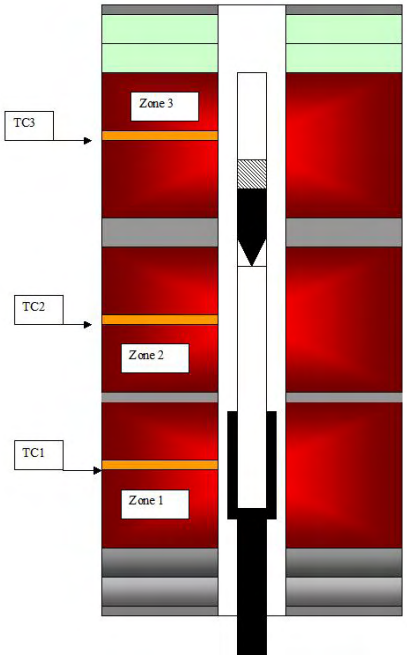

Figure 2.7: Scheme of the Bridgman furnace used at IMEM [18]

ampoule, located in the upper part of the furnace [18]. The furnace currently used at IMEM is set for the growth of ingots up to 3 inches, the crystal size is usually 2 inches. The furnace has three temperature zones, as shown in figure 2.7 with a thermal gradient of 10 °C/cm at the growth interface. The ampoule is then moved along the gradient axis with a speed of 1-2 mm/h toward the cold part of the furnace.

The ampoule is not sealed, contrary to the usual Bridgman technique, because the charge is protected by the melted boron oxide (the melting temperature of boron oxide occurs approximately at 550 °C). This avoids the presence of impurities due to the ampoule sealing procedure. The adhesion of B_2O_3 in the charge surface is produced by means of a moderate pressure (5-10 atm) of inert gas. Beside the higher purity provided by the boron encapsulation, an additional control on the stoichiometry is added by the restriction of free volume during the growth. The boron encapsulation also prevents the contact between the ampoule and the ingot. It's proved that the B_2O_3 is forming a thin molten layer that surrounds completely the charge as schematically illustrated in figure 2.8.

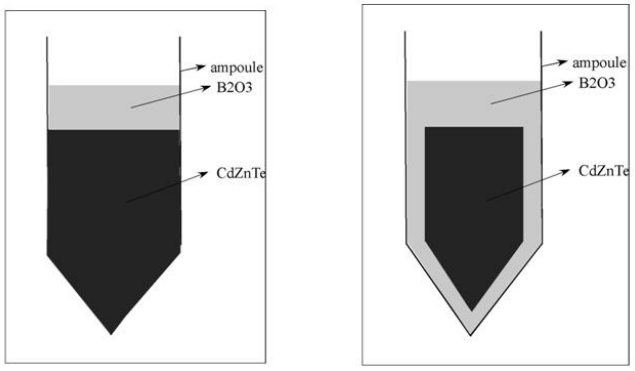

Figure 2.8: Effect of the boron encapsulation during the crystal growth

Low pressure vertical Bridgman

The standard low pressure vertical Bridgman technique has been also carried out at IMEM. The furnace is the same used for the Boron oxide encapsulated Bridgman growth, shown in figure 2.7, the main difference consists in the absence of Boron oxide during the entire process (synthesis and growth). The quartz ampoule in this case is sealed. The growth is preformed in low pressure of inert gas. All other parameters (growth velocity and temperature, etc) are identical to the Boron encapsulation case. The crystals grown with the low pressure Bridgman show a good crystal quality, with large single crystal grains 2.9.

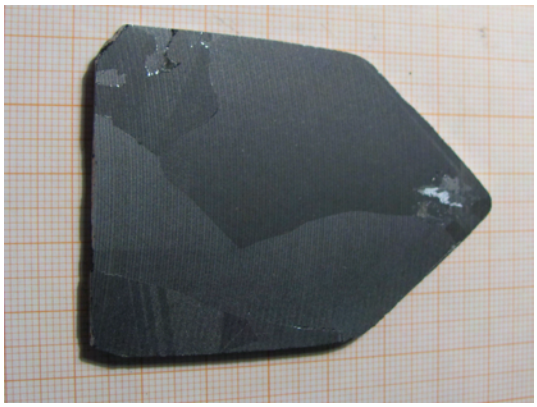

Figure 2.9: CZT slab grown without the Boron encapsulation

CHAPTER 3

Material and device characterization

3.1 Device preparation

3.1.1 Cutting and polishing

The 2 inches ingots grown at IMEM institute are cut into wafers (perpendicular to the growth axis) or slabs (parallel to the growth axis), depending on the measurements that are going to be done on the samples. Several ingots were first cut longitudinally and then on one half was cut perpendicular to the growth axis in order to have both characterizations performed on the same crystal. The cutting process is ideally a trivial procedure, but indeed it represents one of the critical steps in the realization of CZT devices. Every cut is in fact produces several damages that may have a large influence on the performances of the sample as a radiation detector. For the cutting it's used a diamond wire saw. This South Bay Tech. machine allows a regulation of the weight to be applied on the wire, so that an extremely soft cut is possible. The samples used for the characterization of the ingots have usually areas of 7 mm x 7 mm, so that many devices can be obtained from a single wafer. The samples are then polished. At IMEM polishing can be performed in two ways: with semi-automatic procedure, that is commonly used only when a small amount of material is available, and with the automatic polishing machine. The semiautomatic technique consists of a rotating support where sandpapers with different grains are mounted. The support is equipped with a water sup-

plier in order to have a better lubrication on the sandpaper. The selection of the grain size is committed to the user sensibility, however at IMEM we have developed a sort of standard procedure that is working fine with CZT samples. The first paper has a relatively large grain (p2500). The aim of this first stage is to remove a large layer of material in order to eliminate the cutting damaged region (usually 500 μm). The second paper has a p4000 grain SiC sandpaper. All the sandpaper sheets are lubricated with water. After the lapping, the polishing procedure starts. The sandpaper is replaced by polishing cloths. A set of abrasive diamond paste is used with diameters ranging from 3μm down to 0.1 μm. Instead of water a oily solution is used as lubrication. The automatic polishing machine functioning can be divided in two parts: a first polishing part, that consists in the removal of the cutting damaged layer, a p1000 sandpaper is used. The second part uses a combination of mechanical and chemical polishing. The automatic process requires a large number of samples in order to guarantee a homogeneous polishing. The entire process requires a couple of days for the two sides of the samples. The samples are then cleaned with three hot solvents: toluene, isopropanol and acetone.

3.1.2 Contact deposition

The development of a reproducible and high performance contact deposition technique has encountered some difficulties. The main problems are connected with CZT characteristics. CZT is fragile, especially near the edges, and a particular care especially with those techniques, like photolithography, that requires contact between the sample and the mask, with a consequent pressure on the sample. Moreover it's well known the poor adhesion of metals on the CZT surface. This limit can not be overcome with a thermal annealing, as it's usually done, because of the change of CZT properties with temperatures higher then 150 °C. In order to have a smooth surface the samples are etched with two Br based solutions: Br(2%)-methanol and Br(2%)-Lactic acid-Ethilen Glycol. The first etching solution has a higher etching rate, but leaves a Te excess on the surface [35]. Te quikly oxidise leaving a conductive Te oxide layer (TeO_2) [36] on the surface. The second etching solution removes the Te excess on the surface reducing the leakage currents.

Surface passivation

The reduction of surface currents is a main concern in the detector fabrication. Several solutions have been proposed in the literature, almost every solution is united by the presence of H_2O_2 as oxidizing agent [39, 35]. For the realization of our devices the solution proposed by [40] has been chosen. The solution of NH_4F + H_2O_2 has been tested with different oxidation times and it has been decided that a 7 minutes oxidation time is enough to ensure a reduction in the surface currents. After accurate IV measurements [55], it is evident that the detectors prepared on the oxidized surfaces show i) a reduction of the dark current by a factor of two, more evident at forward bias, and ii) a better symmetry of the I-V curves with respect to those prepared on the non-oxidized surfaces. The reduction of leakage currents can be ascribed to the increase of the surface resistance as a consequence of the oxide formation. The improved symmetry, that is evident by comparing the oxidized and non-oxidized thermally evaporated contacts,is a consequence of the increase of the surface stability [55].In fact, the contact evaporation is carried out at different times on the two side of the sample. The oxide layer formed by NH_4F-based etching was studied by optical ellipsometry by using a variable angle spectroscopic ellipsometer working in the range 200-1700 nm. The measured refractive index for the layer is compatible with that of an oxide resulting as a mixture of ZnO, TeO_2 and CdO (n=2.2 and n=2.5 at 1500 nm, respectively [56]). The passivation procedure can be performed on the sample before or after the contact deposition, it has been tested that the oxidizing solution does not affects or removes the metal layer. The two configurations completely change the metal-CZT interface: in one case the metal is in direct contact with CZT, in the second an oxide layer is present between the two.

Thermal evaporation gold contact deposition

Contact deposition using the thermal evaporation is performed in a ultra-high vacuum chamber. The samples are mounted in the chamber and then a primary vacuum is obtained using a zeolites pump (the average vacuum is 10^{-3} mbar). The secondary vacuum is achieved with a cryopump, at this stage the vacuum is $\approx 10^{-9}$ torr. The gold charge is positioned on a molybdenum melting pot and then evaporated by Joule effect. The vacuum chamber is equipped with a in-situ controlling system of the deposited layer. For CZT samples a 750 Ålayer of gold is deposited. Every contact geometry can be transferred on the sample surface by means of photolithography or mechanical masks. Mechanical masks allow only simple geometries and the resolution of the edges is quite poor with respect of other techniques. Photolithography can

instead be applied to any desired contact shape. The equipment present at IMEM uses a UV light to impress the photoresist (a polymeric material that changes its molecular weight after the exposition to the UV light). The masks can be made of quartz or polyacetate, this second type has a worst resolution but it's useful when a complex geometry of the contacts is not a must.

Gold electroless deposition

A very fast contact deposition technique is the electroless deposition. This technique does not require the ultra-high vacuum, in fact it works on the basis of chemical reactions between the sample surface and the metal solution. For the deposition of gold an aqueous solution of $AuCl_3$ in prepared, analogous solutions can be done for the deposition of Pt and Pd. Some drops of solutions are deposited on the surface or the sample itself is dipped in the solution. After 1 minute the reaction reach the maximum thickness and the sample is washed with DI water. The deposition time changes with different metals [38]. The main limitation of this technique consists in the poor control on the deposited thickness and the fact that it's hard to obtain a thickness higher then 600 Å[38]. Beside the fact that electroless deposition is an extremely versatile technique that can be used with several metals and can be coupled with photolithography, it shown a main advantage on the thermal evaporation, it has a better adhesion. The poor adhesion is in fact the factor that nowadays represents the main limit for the detector contact technology, in fact because of the adhesion the bonding procedure is challenging for metal deposition on CZT and the use of conductive paste is almost a must.

3.2 PL mapping of CZT ingots

3.2.1 Optical properties of CZT

Photoluminescence (PL) is a non-destructive optical technique that provides useful information in the characterization of semiconductor materials. The photoluminescence process consists in the emission of radiation by a material, in this case a semiconductor, irradiated with a light source. The emission

of radiation is due to radiative recombination path of photo-excited electron-hole pairs. Through the analysis of the luminescence spectrum as a function of different parameters (temperature, excitation energy or intensity, etc.) several informations on the material quality can be obtained. The success of photoluminescence is basically due to the advantages it has on other technique. It is a non destructive technique and only small quantities of material are needed. It does not require any particular preparation of the sample. It's possible to detect the presence of impurities even at very low concentration. It can give a fast characterization, if a quantitative analysis is needed. PL has also some disadvantages. First, it's not easy to obtain quantitative informations on the doping intensity or the impurity concentration. Moreover it only provides informations on the radiative transitions and it's not a bulk technique, the informations obtained are related only to the surface layers. The plot illustrating the radiative intensity (I) emitted by a semiconductor excited by a radiative source versus the frequency (υ) is the photoluminescence spectra.

Radiative and non radiative recombination

Optical transitions in direct band gap semiconductors are divided into radiative and non radiative recombinations. This two phenomena are competitive, thus the probability that one charge carrier pair in a excited state undergo one of the two events is related to the live time of radiative recombination T_r, the average time when the carrier exist in the excited state before radiative recombination occurs, and the live time of not radiative recombination T_{nr}, the same but for not radiative events. Radiative recombination is present in a spectrum originating a peak. The radiative efficiency in a semiconductor material is given by the quantity η, the internal quantic efficiency for the generation of photons:

$$\eta = \frac{\frac{1}{T_r}}{\frac{1}{T_r} + \frac{1}{T_{nr}}} \tag{3.1}$$

Non radiative events may occur with different events like Auger processes or recombination with emission of a phonon. It is clear that, despite many qualities that make the PL a particularly suitable technique for a fast study of the material, PL only provides informations on the radiative transitions. Non radiative events have only indirect effect on the spectrum and can be studied by looking at the quantum efficiency.

Basic relations between optical constants:

$$n(E) = \sqrt{\frac{1}{2}(\epsilon_i(E) + \sqrt{\epsilon_i(E) + \epsilon_r(E)})} \tag{3.2}$$

$$k(E) = \frac{\epsilon_i(E)}{2n(E)} \tag{3.3}$$

$$\alpha(E) = \frac{E}{c\eta n(E)}\epsilon_i(E) \tag{3.4}$$

$$R(E) = \frac{(n(E)-1)^2 + k(E)^2}{(n(E)+1)^2 + k(E)^2} \tag{3.5}$$

ϵ_i and ϵ_r are the imaginary and real part of the complex dielectric function
k and n are the real and imaginary part of the complex refraction index
α is the absorption coefficient
R is the refraction coefficient

LO Phonon coupling

CdZnTe, as others II-VI semiconductor, has a strong electron-phonon interaction. The electron-phonon interaction can lead to the simultaneous emission of one or more phonons, giving replicas or satellite of the main recombination peak in the PL spectrum displaced by the energies of the relevant phonon. Strong phonon coupling can lead to the observation of multiple order of phonon replicas. In CZT, the direct electron-phonon interaction is dominated by the longitudinal optical (LO) mode because of the associated polarization fields. Transverse optical (TO) are normally not observed in CZT PL spectra. In the first order approximation the probability of electron recombination and n phonon emission is given by:

$$P_n = e^{-s}\frac{S_n}{n!} \tag{3.6}$$

where S is the Huang-Rhys factor. This factor describes the strength of the electron-phonon interaction, representing the average number of phonon involved [24]. In CdTe the LO Phonon can couple with Huang-Rhys factor up to S= 3, 4. Since the distribution of replica intensities is not monotonous for S>1 the maximum PL intensity is not found for the zero phonon line for strong electron-phonon coupling constant. Considering a defect complex with a center of inversion, the quadratic distribution will be:

$$I_n \approx \frac{2n!}{2^{2n}(l!)^2}S'^{2n} \tag{3.7}$$

where I_n is the intensity of the n-th phonon replica.

S', the interaction strength, is a parameter. S' value is always less than 1, being the replicas intensities monotonously decreasing. In CdTe and as well in CZT, the individual LO Phonon replicas are separated by 21 meV [19].

Intrinsic transitions

Free excitons

A free hole in the valence band and a free electron in the conduction band are subject of a Coulomb interaction that forces the pair to act a composite particle called exciton. The energy states of the free exciton can be described by :

$$E_x = E_g - \frac{2\pi^2 m_r^* q^4}{h^2 \epsilon^2 n^2} \tag{3.8}$$

Where ϵ is the dielectric constant E_g is the band gap energy and m_r^* is the reduced effective mass of the electron-hole pair. m_r^* is given by:

$$\frac{1}{m_r^*} = \frac{1}{m_e^*} + \frac{1}{m_h^*} \tag{3.9}$$

The ground state is represented in equation 3.8 for $n = 1$, a series of peaks occurs at energies given by the number n ($n = 2$ represents the first excited state and so on). In CZT the binding energy of the free exciton is 10.8 meV [20]. The value for CdTe is about 10 meV and 13 meV for ZnTe [19]. In some high quality CZT the second excited state of free excitons has been observed, high order excited states merge into the conduction band due to the free exciton kinetic state.

Band to band transition

In direct band gap semiconductors, for a first approximation, band to band transitions don't change the wave vector k of the electron or hole involved in the transition. The starting state in the valence band and the arrival in conduction band are characterized by the same vector in the reciprocal space. Assuming the moment p slowly changing with k and assuming $p_{mo}(k) \approx p_{mo}(k = 0)$, the absorption coefficient direct band to band transitions is given by:

$$\alpha(x) = A\sqrt{E - E_g} \tag{3.10}$$

Where A is:

$$A = \frac{2\pi^2 e^2 \sum_{v.b.} (2m_r^*)^{3/2} |p_{m0}^2|}{3m_0^2 n \epsilon_0 c h^3 \upsilon} \tag{3.11}$$

The summation is necessary because of the degeneracy of the heavy and light holes band in $k = 0$

Extrinsic transitions

Bound excitons

When excitons are near a defect, the defect can either increase or decrease the biding energy of the exciton. When the effect of the defect is to decrease the total energy of the exciton, it will be trapped about the defect, leading to the formation of a bound exciton. This complex exists as a neutral defect. Since the bound exciton as no degree of freedom, the mean free path is very small, because usually recombination occurs. Bound excitons give rise to an emission at lower energy then that of the free excitons. The bound exciton emission line is narrower than the one showing the free exciton because of a higher localization. The typical energy of a donor bound exciton (D^0, X) is 4meV and for a exciton bound to a neutral acceptor (A^0, X) is between 6 and 16 meV [22, 23].In CZT excitons bound to donors and acceptors exhibit peak just below the free excitons emission line.

Bound to free

Bound to free transition occurs between acceptor and donor or between valence and conductance band. The energy balance must include the kinetic energy of a free electron/hole.

DAP recombination

CZT may contain both acceptor and donor impurities, these donors and acceptors can form pairs (DAP) and act as molecules embedded in the host crystal. The Coulomb interaction between the impurities will have an influence on the binding energy of the isolated impurities. This transition involves the transfer of electron between bound states of a donor and acceptor pair. The ΔE is given by:

$$\Delta(E) = E_g - (E_D - E_A) + \frac{e^2}{4\pi\epsilon R_{DA}} \tag{3.12}$$

R_{DA} is the distance between acceptor and donor. With assumption of random donor-acceptor pair distribution, for typical dopant concentration, the Coulomb term is about several meV. DAP has been often observed in the 1.4-1.5 eV region of CdTe spectra, a similar behavior is observed in CZT spectra, especially when Zn molar composition is low.

3.2.2 CZT photoluminescence spectroscopy

The first work that extensively studied the PL in CdTe samples is [69], this paper is focused on absorption and PL measurement at liquid nitrogen temperature. This work give rise of a number of studies in the 60 and 70 that soon explored the CdTe response at liquid helium temperature [25]. With this step most of the transitions known today were first seen and studied. Soon after also CdZnTe, in many compositions, became an interesting topic for PL study. A typical 4.2 K spectrum of CdZnTe is shown in figure 3.1. As reported by [20], for a better understanding and analysis, it's useful to separate the spectrum in four different regions (figure 3.1).

1. Near band-edge emission: free and bound excitons peak
2. Donor acceptor region: (D, A) transition and its 2 phonon replicas
3. A broad defect band centered at 1.4 eV, called A-center
4. A band centered at 1.1 eV, commonly ascribed in literature as Tellurium vacancies [20]

The first region contains some interesting information of the low temperature PL spectrum. The dominant peak is the (D^0, X), donor bound exciton. As reported in [20], in CZT ingots both (A^0, X) and (D^0, X) peaks can be the main contribution in the excitons region, the ration between the two peaks basically depends on the growth technique and the Zn composition.The dominant (A^0, X) peak is commonly seen in CdTe spectra and low Zn CZT, e.g. $Cd_{0.96}Zn_{0.04}Te$,[20]. The spacing between the two free exciton peaks can be used to determine the free excitons peak. The (D^0, X) peak is located 13 meV below the band gap energy [21]. From the position of this peak it's possible to calculate the bandgap position.

This property makes the PL mapping the ultimated technique for the study of crystal growth. From a deep study of the PL maps it's possible to extract many useful information about the growth interface and a good understanding of the growth processes. The energy gap value, and hence the energy gap peak position, is dependent on the Zn quantity and the temperature. During the PL

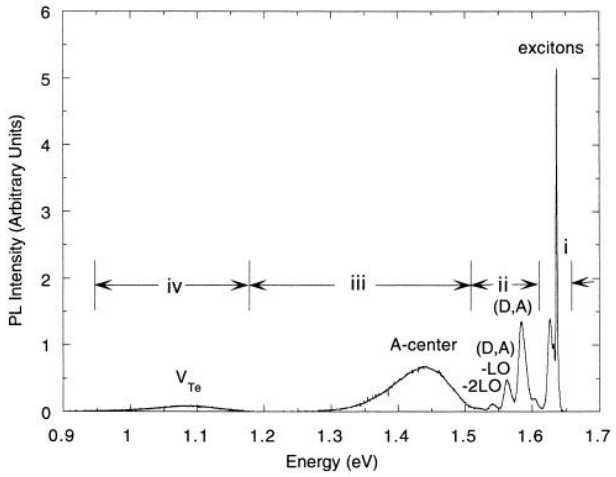

Figure 3.1: The typical 4.2 K spectrum of a CZT sample [21]

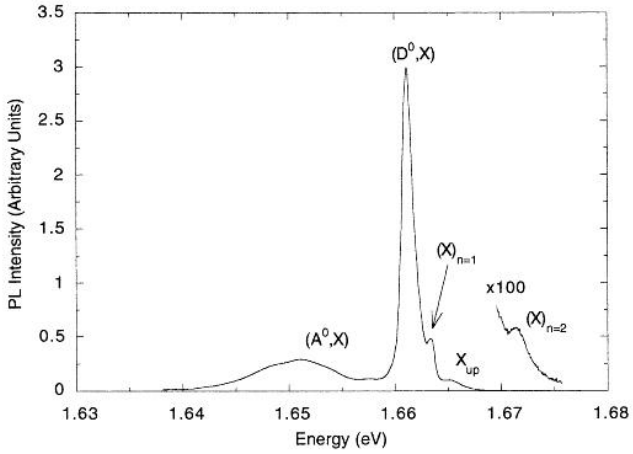

Figure 3.2: Near band edge PL spectrum of a CZT sample[60]

mapping measurement the temperature is controlled and maintained constant, through the use of a continuous liquid nitrogen flux. The position of the gap is therefore only dependent on Zn concentration. The DAP region in figure 3.1 show the DAP peak and two phonon replicas. In good quality materials, the DAP peak is also present, as a shoulder of the bound excitons contribution, at liquid nitrogen temperature In figure 3.2 the first excited state of the free excitons is clearly visible, together with the ground state. The presence of these two peaks is a proof of the good quality of the material.

3.2.3 The PL mapping set up

The PL mapping system must be tailored in order to acquire a sufficient number of spectra, in order to ensure a good resolution, and, at the same time, maintain a reasonable duration of the measurement. For this reason fast equipment is required together with an adequate choice of the measurement parameters. A PL map is basically a bi-dimensional grid, for simplicity the xy plane, and for every point of the grid a PL spectrum is acquired. The spectra can then be processed with the help of a program interfaced with the acquisition system. The measurement setup used for the PL mapping can be simplified into 5 blocks, as shown in figure 3.3:

1. The spectrophotometer FTIR (Fourier Transformate Infra Red spectrometer)
2. The laser source, is an Ar laser (λ=512 nm), the laser intensity can be tuned in the range between few mW up to 700 mW)
3. The cryostat
4. The automatic positioning system (xy stage)
5. The remote elaborating program, it is a commercial system created by Bruker: Opus 6.5

Spectra acquisition is carried out by spectrophotometer FTIR Bruker IF66. The functioning of the spectrophotometer is illustrated in 3.4.

The spectra is generated via the interferogram of the IR emission of the sample, the beam splitter divides the IR signal from the sample into two beams. Using a time changing optical path difference the two beams are interfering on each other, this path difference is created using the moving mirror. The

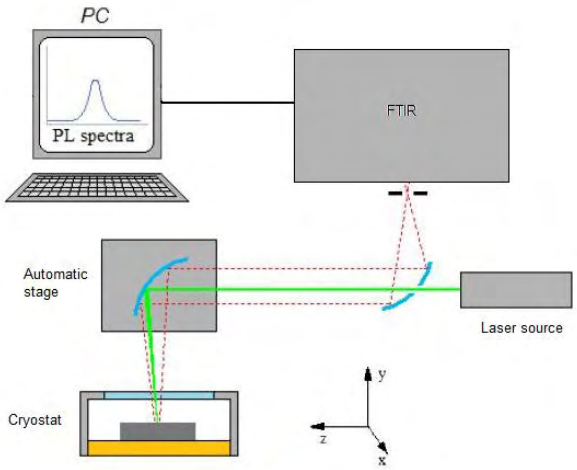

Figure 3.3: A scheme of the PL mapping set up, highlighting the 5 basic components

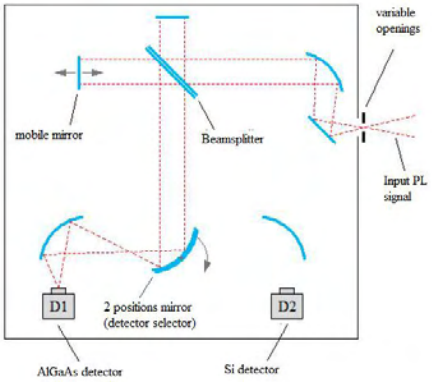

Figure 3.4: A scheme of the FTIR spectrophotometer

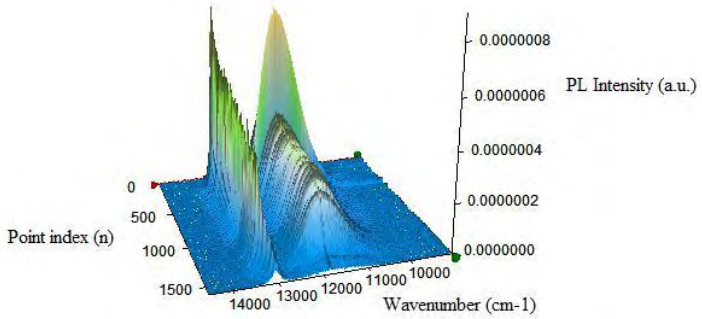

Figure 3.5: The *emis* spectrum resulting from a PL mapping measurement

beam resulting from the interference is then impinging the detector, that which measures the intensity of the beam creating the interferogram.

The detectors used for the CZT PL measurements are two:

- A InGaAs detector operating between 5800 and 11000 cm^{-1}
- A Silicon (Si) detector operating between 9000 and 15000 cm^{-1}

The cryostat is able to operate at both liquid nitrogen and liquid helium temperatures, as well as it's set for a heating system. For the PL mapping set up it's fundamental an automatic movement in the xy plane, the plane where the sample is lying. The movement range of the xy stage in 5 cm in each direction, the movement is basically limited by the size of the sample holder-cryostat. The movement of the xy stage is controlled by the PC, using the Bruker 6.5 program. This program is extremely versatile and offers several tools for the spectrum analysis, e.g. the peak peaking function or the spectrum integration. The acquired spectra of the map are all saved in a single file that includes the emission spectrum, called *emis*, and the interferogram. In figure 3.5 is shown a *emis* spectrum acquired with the Si diode, every calculation is carried out starting from this spectrum. Every spectrum is positioned sequentially on the point index axis after the acquisition, for every shift in the xy plane. The other horizontal axis represent the wavenumber (expressed in cm^{-1}), both the near band edge emission and the A-center are clearly visible. The vertical axis is the PL Intensity. Every spectrum represents a point on the sample surface. Every operation on the *emis* spectrum generates a new file, called trace. If several operations are performed on the same spectrum, this will generate a series of independent files, each one corresponding to a operation performed on the spectra file. The file resulting from the operation is called *trace*.

3.3 Synchrotron White beam X-ray diffraction topography

X-ray topography (XRT) ([26, 27]) is an indispensable tool in the study of a diverse number of important areas in crystal characterization. XRT present some advantages, that make it a particularly appealing technique for the study of the structural defects. XRT is a non destructive technique, it does not require any specific surface treatment or preparation of the sample. The sample size can vary between a few millimeters up to several centimeters, depending on the sample-source distance. In X-ray topography the samples are illuminated with an X-ray beam and images of the diffracted beams are recorded on a X-ray sensitive film. Two cases are distinguished: the Bragg, or reflection, case and the Laue, or transmission, case. In the Bragg case the diffracted beam leaves the crystal trough the entrance surface, in the Laue case, if the absorption is small enough, the beam is emerging from surface opposite to the entrance one. All the information are obtained by studying the contrast differences in the X-ray sensitive film , in fact the topography image is the result of X-ray wave fields interfering each other inside the sample. For a perfect crystal the topography image will then result in a perfectly homogeneous diffraction spot of the sample. The defects in the crystal are not present as themselves in the image, but the lattice deformation surrounding the defects produces an intensity variation (and thus a contrast variation) between the perfect region and the defect region. The use of a synchrotron radiation instead of a conventional X-ray source provides high brightness and high intensity (many orders of magnitude more then common X-ray sources), high natural collimation, widely tunable in energy with the help of monochromatization, high resolution on the X-ray film. Synchrotron XRT fits many diffraction geometries.

- Transmission geometry
- Back reflection geometry
- Reflection geometry
- Grazing incidence geometry

The informations obtained vary from geometry to geometry. In figure 3.6 four diffraction geometries are shown. In the reflection (Bragg) geometry the topographic image highlights the structure of the near-surface region (usually from 10 up to 100 μm, depending on the energy of the impinging beam). In the transmission geometry bulk information are instead present. In fact,

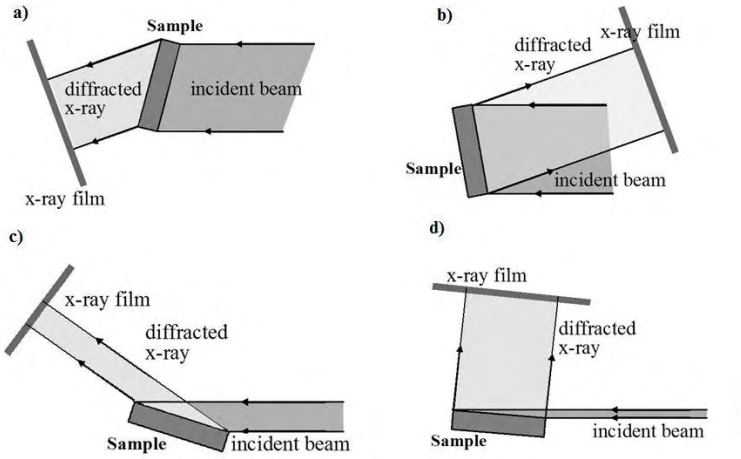

Figure 3.6: Schematic illustration of the different geometries that are commonly used in XRT: a) transmission geometry, b) back-reflection geometry, c)reflection geometry, grazing incidence geometry.

provided the sample has a good crystal quality, a transmitted image can be recorded through several millimeters in the material. The information that can be obtained by the XDT include: the distribution of dislocations (most common defect), the distribution of lattice strains, sub-grain structure (misorientation angles), the presence of secondary phases and twins. No information can be obtained about the 0D defects (point defects). When a white (polychromatic) X-ray beam is impinging the surface of a crystal, many diffracted spots appear on the X-ray film. The use of a white beam is particularly simple, in fact it's not necessary to adjust the sample position. Many reflections will fulfill the reflection condition at the same time. The position of the spots follows the Bragg equation:

$$\lambda = 2dsin\theta_B \tag{3.13}$$

where λ is the incident wavelength and θ_B is the Bragg angle. This 2D diffraction spot constitutes the X-ray topography image. As it was mentioned before, the understanding of the topographic image formation arise from the contrast. A detailed analysis of the contrast can be found in many available resources, Tanner (1975), Bowen and Tanner (1998) or Kato (1996). Two categories of contrast are distinguished:

- Orientation contrast. Orientation contrast originates when parts of the sample have different orientation, so that they don't satisfy the Bragg law and therefore they are not diffracted. The zero intensity area correspond to the geometrically misoriented part of the sample. For a white radi-

ation source however different wavelengths are diffracted in differently oriented regions leading to a displacement of their diffracted image in a different part of the film. The orientation contrast arises with two main mechanisms: the misorientation exceeds the divergence of the beam, resulting in a lack of diffraction, or the diffracted beam from two parts of the crystal takes different directions in the space. In figure 3.7 the two different mechanisms for a monochromatic and a continuous radiation are shown. For a monochromatic beam, as explained in example a) the misorientation exceeds the divergence of the incident X-ray beam, giving a zero intensity zone. In the second case, b), is shown a diagram in the case of a continuous radiation, in this case there is a gain or loss of intensity in the boundary of the misoriented region.

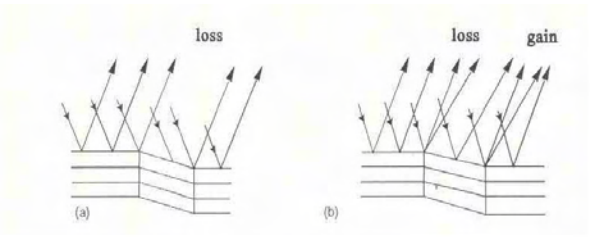

Figure 3.7: The scheme proposed by Tanner [28] for the explanation of the orientation contrast. In a) is shown the behavior of a monochromatic beam, in b) the case of a white beam

- Extinction contrast. This contrast origins from a difference in scattering power near the defect with respect of that of the perfect crystal. Extinction contrast is described by means of kinematical or dynamical theories of X-ray diffraction. There are three types of contrast, that are schematically represented in figure 3.8 by Tanner. The image is divided in two cases: a large strain gradient (figure *a*)) or a small strain gradient (figure *b*)). For a specific wavelength the reflecting range of a perfect crystal is very small, the peak reflectivity is close to 100% and the scattering power is proportional to the structure amplitude of the Bragg reflection $|F|$. For an imperfect part of the crystal the reflecting range is broader, the reflectivity is less than 100% but the integrated reflectivity is proportional to $|F|^2$. There are three kind of extinction contrast, in figure 3.8 a) it's shown the mechanism of their formation. The direct image, shown in the picture as *1*, is the result of the diffraction of x-rays that don't satisfy the Bragg condition in the perfect crystal. The formation of

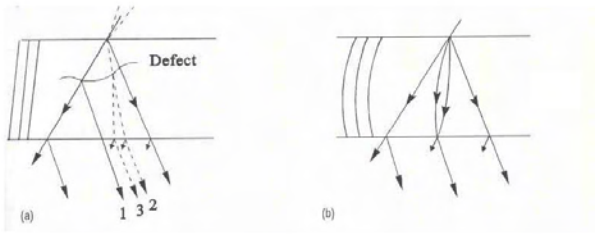

Figure 3.8: Extinction contrast, image by Tanner [28]. Two cases are studied: a) when the strain field gradient is high, and b) when the strain field gradient is low

a direct image is the most common mechanism [28] and it's characterized by an enhanced intensity that appear darker with respect to the perfect crystal. The dynamical image, indicated as *2*, is formed by the change of intensity in the Bloch wavefields propagating through the perfect crystal, it is most commonly seen in high absorption conditions. The intermediary image, number *3*, is formed by the interference by those wavefields and the new wavefields originating at the defect, it is seen in conditions of moderate absorption and small inclination of the defects. It provides informations on the structure factor.

3.3.1 CZT White Beam X-ray Diffraction Topography

CZT ingots are commonly affected by the presence of defects. Some of them have a severe influence on the detector performances, and thus it's necessary to find a way to remove them. Other defects don't affect the properties and detector response in such a heavy way and thus can be tolerated, provided that the concentration is low. The most common defects in CZT ingots can be seen by the white beam X-ray diffraction topography (WXDT) analyzing the orientation and extinction contrast of the images. WXDT is an extremely useful tool for the characterization of the devices. The material is cut in slices or slabs and then the samples are obtained by cutting the wafer into parts of the suited dimensions. The selection of a "good" or "bad" part on a wafer is crucial for the device properties. Some defects can be seen by naked eye and then avoided during the cutting process, like twins and grains with different orientation. Other defects are instead impossible to be detected without a topography image. A WXDT image can give information on

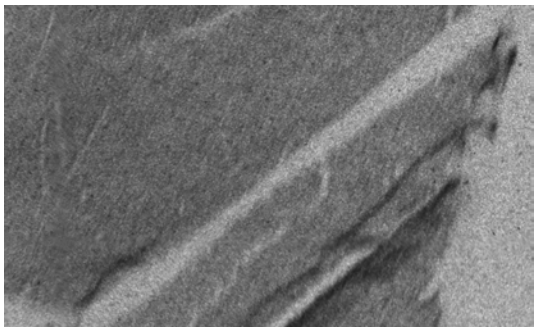

Figure 3.9: Grain boundaries in a CZT sample

- 1 dimensional defects: such as dislocations (that are also the most common defect)
- 2 dimensional defects: grain boundaries, twin boundaries. It's important to underline that this kind of defect can be easily detected by watching the surface only if the misorientation is high. For low angles the topography image is necessary
- 3 dimensional defects: inclusions and precipitates. Point defects are not visible in WXDT, but when they cluster to form a precipitate or inclusion they give a characteristic contrast image. They can appear dark or bright depending on the absorption condition of the measurement and on the position of the precipitates (close or far from the entrance surface). Those defects are also very common in CZT ingots

No information is obtained on point defects (0 dimensional defects). From the WXDT a lot of information can be extracted, to determine the crystalline quality of a CZT ingot. Grain boundaries and twins are well known defects affecting the growth of CZT, despite all the efforts performed for limiting the presence of such defects, so far it is still impossible to obtain an entire ingot completely free of defects. In figure 3.9 grain boundaries are present. As expected from the orientation contrast theory, the region with a different orientation appears white in the image, being the result of a lack of diffraction. A clear effect of the extinction contrast in a topography image is present in figure 3.10 The dark lines are a network of dislocations.

3.3.2 White Beam X-ray Diffraction Topography set up

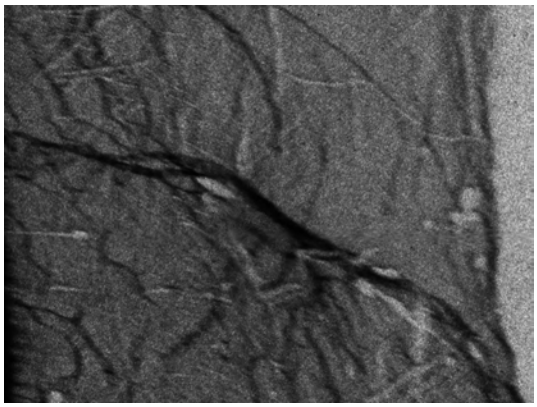

Figure 3.10: Dislocation walls, WXDT on a CZT sample

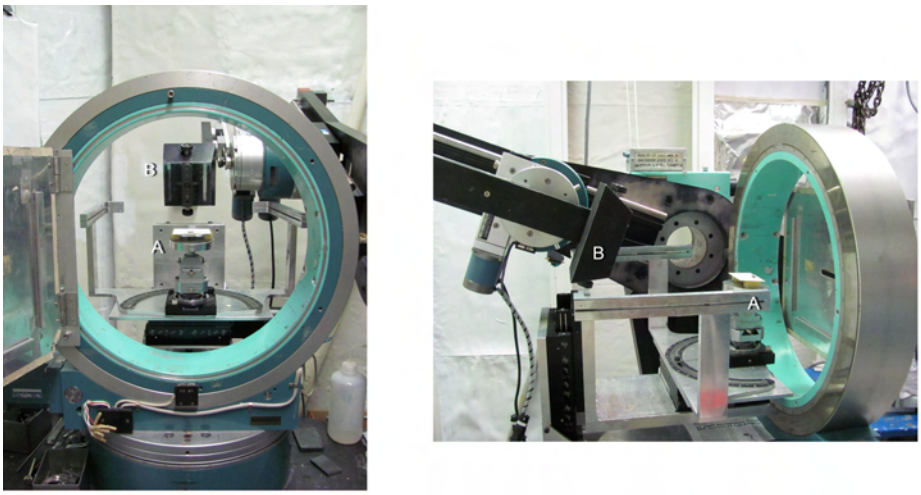

Figure 3.11: Side picture of the WXDT beamline hutch, the letter A indicates the sample holder, the letter B indicates the position of the X-ray film. The beam is impinging from the right side of the image on the right

The WXDT measurement were performed in the Brookhaven National Laboratory (BNL), Upton, NY. The National Synchrotron Light Source (NSLS) is a research facility in BNL, the accelerator is producing synchrotron light from the UV range up to the X-ray range (100KeV). The beamline equipped for the WXDT has a spectral range up to 35 KeV, the beam is white, in order to avoid the sample alignment necessary when the beam is monochromatic. The source size is small: 300μm x 100μm.

The hutch is quite large, so it's possible to have a distance of 25 m between the source and the specimen. All the measurement were done in reflection geometry. The beam is impinging the surface of the sample and then is reflected on a X-ray sensitive film. The sample size can vary between few mm and 4 cm.

The sample size is basically limited only by a lead slit (it is present in figure 3.11) that is positioned before the sample, the purpose of the slit is to avoid uncontrolled reflections by the objects present in the hutch. In figure 3.11 are shown two pictures of the WXDT set up. The first picture is a side image: the beam is impinging from the left side. In the picture are shown the sample holder and the X-ray film holder. The second image shows the direction of the beam, the sample position and the film holder. The beam needs to be shaped in order to have almost the sample size, this is necessary to obtain a better contrast in the spots.

3.4 IR Microscopy

High resistivity in CZT crystals is usually obtained by contemporary doping with group-III or VII elements and using Tellurium deviated charge [18]. The latter condition is responsible for the presence in the crystals of a large number of Tellurium inclusions. These can be incorporated at the growing interface or can be formed during cooling as a result of the retrograde behavior of the liquidus curve [29]. Unfortunately, inclusions severely limit the performances of CdZnTe-based detectors, particularly in the case of imaging devices [33]. Te inclusions are responsible of a considerable charge loss in the CZT based detectors. In fact inclusions act as traps for electrons and it has been calculated to represent the 10% of the lost charge [32]. In a recent work [33] it has been estimated the total number of inclusions and the maximum size allowed before the detector properties are compromised. Te inclusion presence can be revealed by means of different techniques. One of them consists of the determination of equilibrium vapor pressure of samples at high temperature: if the Tellurium phase is present, the total pressure is dominated by Tellurium partial vapor pressure and the overall stoichiometry deviation can be determined [61] and [62]. However, every information on dimensions and distributions of the inclusions is lost. Inclusions can be revealed also by optical transmission in the near-infrared. Tellurium and Cadmium inclusions are actually opaque in the infrared, in the transparent region of the material. A relation between the infrared extinction spectra and inclusion density was found [63]. However, this technique suffers the same from limitation as that of the latter. The study of the contrast in the IR image provides informations on the concentration and size of Te or Cd inclusions [29]. To determinate the concentration of inclusions is not an easy task. The scanned area is limited by the field depth of the microscope, that is determined by the magnification. The field depth is much narrower than the sample thickness (usually some millimeters), so only a layer

of the sample will be on focus in the final image. The numerical aperture of the objective lens, that depends on the constructor parameters, is related to the depth of field (P) with the formula:

$$P = \frac{n\lambda}{2NA^2} \tag{3.14}$$

where n is the refraction index of the material and λ is the wavelength of the radiation. In order to overcome this limitation a number of image processing tools have been developed; the aim is to reconstruct the entire thickness of the sample by taking a set of picture at different depths. The final picture is commonly called *collapsed image* or *extended depth of field*[30]. While calculating the number of pictures necessary for a good image the refraction index of the material should be taken into account, in fact considering a movement Z$'$ of the sample results in an effective movement Z given by:

$$Z = nZ' \tag{3.15}$$

The *collapsed image* is able to provide an image of the entire thickness but is still affected by some limitations. It is not possible to distinguish two inclusions in the same position but at different depths, in this case only one inclusion will be counted (the concentration is always affected by deficiency). The second limitation is the loss of the 3D position of the inclusion. With the extended focus the pictures representing all the layers are in fact added to form one single picture that is the sum of all the depth. The inclusions can be identified with dimensions down to 1 μm.

3.4.1 IR Microscopy set up

At Brookhaven National Laboratory two IR microscopy systems are used: one is dedicated to the acquisition of large images, the other is used for the calculation of size and concentration of Te inclusions. For the large images,a Nikon optical microscope is used, equipped with an automatic *x*-*y*-*z* movement system (3.12 part b)). For the acquisition of near IR images the microscope has been equipped with a Si camera connected to the PC. The Si camera is suited for the detection of Te inclusions in CZT and CdTe, for different materials a different camera should be chosen. A commercial software is used for the image processing: the creation of a large area picture, as well as a scan in the Z axis (perpendicular to the sample surfaces are all controlled and managed by the software. This instrument is able to use the limited field depth, that is an intrinsic characteristic of the microscope, for the creation of a 3D image of

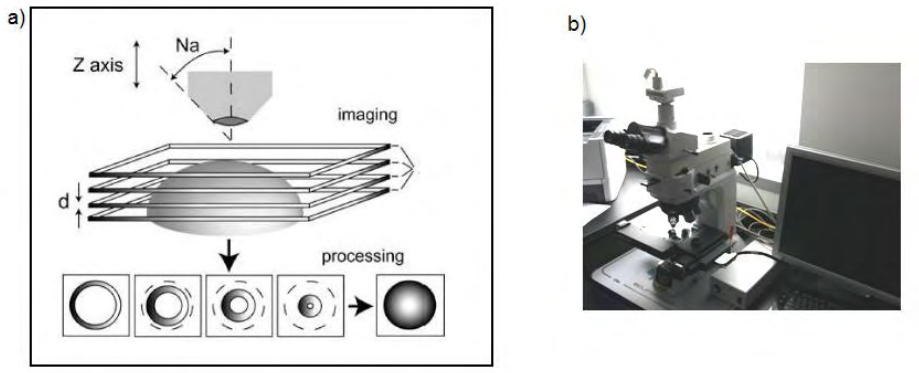

Figure 3.12: Scheme of the operation of a IR microscope. N_a is the numeric aperture and d is the field depth (or axial resolution) [32].

the sample: several images are acquired at different depth and then combined to form the final 3D image

In figure 3.12 a) the basics of the IR microscope functioning are shown. The direction of the z axis is shown, the movement in that direction is automatically controlled. A set of picture are acquired, each of them scans a depth indicated as d in the image. Every picture contains a part (d) on focus and the rest results as fuzzy. Using a specific software it is possible to extract from the picture just the focus part and discard all the parts out of focus. The final image is a 3D map of the sample pointing out the spatial position of every inclusion. It is possible to decide for every measurement the required number of images necessary for the 3D imaging, provided that the sample thickness, the objective lens and the material refraction index are given. The system for the analysis of the Te inclusion density and size distribution is a optical bench composed by: A) the light source (a Edmund MI150 fiber optic illuminator), B) the sample holder with an automatic translator stage, C) the objective lens (usually a 5x magnification lens is used) and D) the CCD camera, connected to the PC, the resolution of the camera is 1 μm. The images are processed using a specific IDL routine. The contrast of the IR picture is analyzed and then using the reverse map (the lack of transmitted light produced by the Te inclusion correspond to a maximum in the reverse map) the size and concentration is calculated. The IDL routine is able to discard the contribution of the surface features, as scratches, that also produce dark spots in the image by selecting events with a circular shape in the x-y projection. The event selection can be tuned manually, in order to have the control on the selection of every feature.

A set of images in the z axis (perpendicular to the sample surfaces) is acquired and then elaborated in the same spot, for the 5x magnification lens

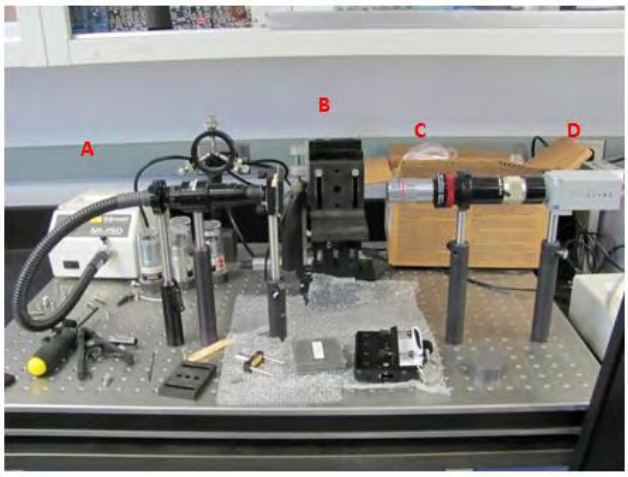

Figure 3.13: Optical bench for the study of the Te inclusion density and size distribution. The basic components are highlighted in the image: A) the light source, B) the sample holder, C) the objective lens, D) the CCD camera

the spot size is 1.1 mm x 1.5 mm. The IDL routine is able to manage up to 5 spots for every run. The result of the elaboration is a histogram where in the x axis is reported the dimension of the inclusions (in μm) and in the y axis is reported the number of features. The routine also produces a 3D reconstruction of the inclusion in the spot, the reconstruction process does not take in account the refraction index of CZT and hence the 3D image looks elongated. The output produces 4 3D images rotated by 90 °C in the surfaces plane. The typical result of the IR transmission set up is shown in figure 3.14, in a) is shown the histogram for the size distribution of Te inclusions and in b) one of the four 3D images generated in the 3D reconstruction, the scanned volume is 1.1 x 1.5 x 2 mm^3.

3.5 I-V Measurements

Current-voltage (I-V) measurement represents the principal tool for the determination of the electrical properties and the resistivity of the material. Considering a metal-semiconductor interface, for an n-type semiconductor, the equilibrium is given by:

$$q \cdot \Phi_{bn} = q \cdot (\Phi_m - \chi_s) \tag{3.16}$$

Φ_{bn} is the potential barrier, Φ_m is the metal work function and χ_s is the electronic affinity of the semiconductor. In the case of an ideal contact in

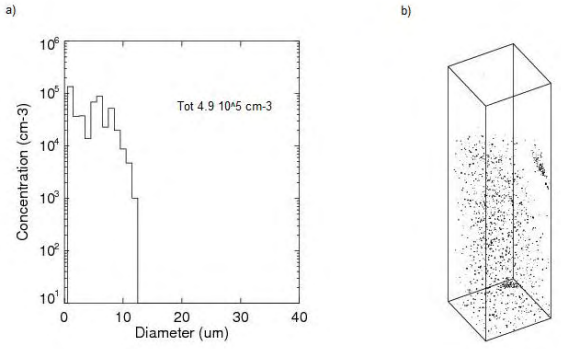

Figure 3.14: a) Te inclusion size distribution histogram and b) space distribution of the inclusions in the same position

principle it's possible to fix the Schottky barrier height by changing the metal, and thus the metal work function. The V_{bi}, built in potential is given by the difference between the work function of the metal and the one of the semiconductor:

$$Vbi = \Phi_m - \Phi_s \tag{3.17}$$

For a n-type semiconductor when $\Phi_m > \Phi_s$ the contact assumes a rectifying characteristic and when $\Phi_m < \Phi_s$ the contact is ohmic. Measurements on the barrier hight have demonstrated that this relationship is not always respected because of the presence electronic states on the surface, that change the band curvature. The most common contacts on CZT are Au and Pt, both are forming a rectifying contact. The current-voltage characteristic passing trough a Schottky barrier can be explained using the thermionic emission theory:

$$J = J_s(exp(\frac{qV}{nKT} - 1)) \tag{3.18}$$

n is the ideality factor, and for a good diode its value is between 1 and 2. J_s is the saturation current density of the diode. When $qV << nKT$, and that means $J << J_s$, equation 3.18 can be written as:

$$J = J_s(\frac{-qV}{nKT}) \tag{3.19}$$

In equation 3.19 the relationship between current and voltage is linear. Considering the influence of the surface currents in CZT samples, the resistivity of CZT detectors cannot be measured with the 4 tips method. In a recent work Szeles [41] proposed a method for the calculation of resistivity from the I-V characteristic. The detector device is considered as a diode with a series

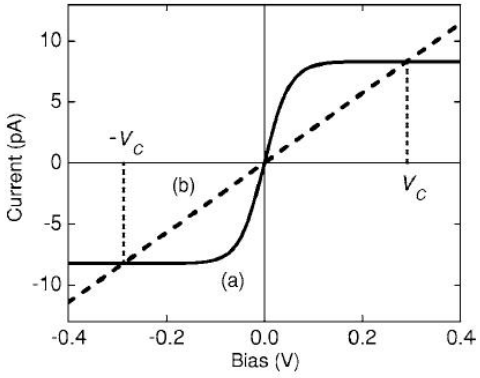

Figure 3.15: The low voltage I-V characteristic of the back-to-back configuration [41].

resistance, the thermionic emission theory can still be used to explain the system with some modifications:

$$I = I_s(exp\frac{q(V_B - IR_S)}{KT} - 1) \tag{3.20}$$

I_S is the reverse saturation current and R_S is the semiconductor series resistance. When the current is low, it is possible to obtain the R_S value:

$$R_S(I \to 0) = \frac{V_B}{I} - \frac{KT}{qI_s} \tag{3.21}$$

in 3.21 the second part of the equation can be divided into two contributions: the first one represents the contact resistance R_C, the second one is just a small correcting contribution and can be derived from the I-V curve. The I-V characteristic, for a CZT detector with two identical planar contacts on the surfaces, is the one of two diodes in the back-to-back configuration. As it's shown in figure 3.15 in the low voltage range the curve is linear.

In this range the currents are dominated by the bulk contribution. In this ohmic-like trend the saturation current is limited by the resistance of the material. If the bias is lower then $\pm V_C$ the resistance of the semiconductor can be extracted from the I-V curve. Obviously, this model works only in case of high resistivity materials, otherwise the contact resistance of the contacts is too high with respect to the resistivity of the semiconductor.

3.6 Electric field measurement by means of the Pockels effect

The electric field distribution can be calculated in some semiconductor devices by means of the Pockels effect. Birefringence can be natural or can be caused (mechanically or electrically) in piezoelectric or isotropic materials. The electric field induced birefringence is called Pockels effect.

The linear electro-optic effect is the change in the indices of the ordinary and extraordinary rays that is caused by an applied electric field. This effect exist only in crystals that do not posses inversion symmetry as cubic crystals of the zincblende class such as GaAs [51], InS and CdTe [48, 50]. The effect of the birefringence on the orthogonal polarization directions can easily be described by the index of ellipsoid. This index describes the geometrical properties of the crystal with respect to the principal indices along the crystallographic axes (x,y,z). Any change of these geometrical properties of the crystal, introduced by the application of an electric field transverse to the direction of the light, cause asymmetry that changes the indices of refraction. Applying an electric field parallel to the <111> orientation, 3 new refractive index can be defined : n'_x, n'_y and n'_z. After travelling trough the crystal, the light components undergo a phase shift proportional to the change in the refractive indices, resulting in the transmitted light to be modulated.

$$n'_x = n_0 + \frac{1}{2\sqrt{3}} n_0^3 r_{41} E \tag{3.22}$$

$$n'_y = n_0 - \frac{1}{\sqrt{3}} n_0^3 r_{41} E \tag{3.23}$$

$$n'_z = n_0 + \frac{1}{2\sqrt{3}} n_0^3 r_{41} E \tag{3.24}$$

where n_0 is the principal, field free refractive index in all three directions, r_{41} is a component of the linear-optic tensor and E is the applied electric field.

The optical arrangement shown in figure 3.16 consists of a polarizer before and a polarizing analyzer after the sample. The sample is biased at different biases, with values up to 1000V. An incoming unpolarized light produced by a tungsten lamp is polarized by passing trough the first polarizer. By crossing the sample the polarized light is split into two orthogonal plane waves, one parallel and one perpendicular to the applied field. The light intensity emerging from the analyzer is then recorded by the CCD connected to the PC. Several filters (800-1500 nm) are used to change the intensity of the impinging light.

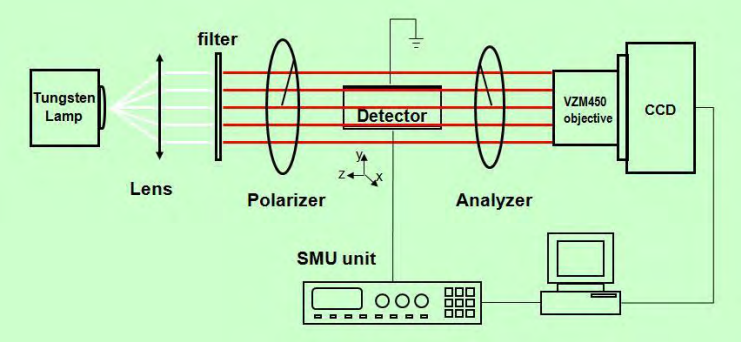

Figure 3.16: Scheme of the setup used for the electric filed measurement by means of the Pockels effect

The maximum in the transmitted light is obtained when the two polarizer are parallel and no electric field is applied to the crystal. The transmitted intensity of the light trough the crystal can be related to the applied electric field by a sinusoidal function

$$\frac{I}{I_0} = sin^2\left(\frac{sqrt3\pi n_0^3 r_{41} E d}{2\lambda_0}\right) \tag{3.25}$$

The measurement of the ratio $\frac{I}{I_0}$ can determine the value of the average electric field applied perpendicular to the direction of the light propagation.

3.7 The Co.Re.Ma. system

Previously it was illustrated a method for the measurement of the resistivity that does not require a specific equipment beside the I-V setup. However a more precise measure can be obtained using the Co.Re.Ma. technique. The contact-less Resistivity Mapping (Co.Re.Ma.) instrumentation can measure point to point the resistivity of high resistivity materials. A detailed description of the technique can be found in [42]. The concept of this technique is to measure the dielectric relaxation time of the semiconductor τ.

$$\tau = R_S C_S = \epsilon\epsilon_0\rho \tag{3.26}$$

This equation is valid only in case of low contact resistivity between the plates of the capacitor and the semiconductor, it's not easy to satisfy this condition. Therefore the capacitor is positioned at a distance d_{a1} and d_{a2} away from the semiconductor (figure 3.17 part a).

In figure 3.17 a) a scheme of the sample and capacitors is shown, the two distances d_{a1} and d_{a2} are clearly visible, this forms a parallel capacitor C_A that is the result of the two air capacitors in series. In the second part of the image

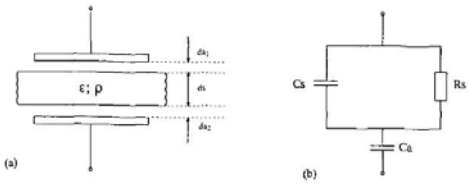

Figure 3.17: the schematic image of the capacitor and the the block scheme of the circuit proposed by Stibal [42]. C_A is the two air gap capacitors illustrated in a), C_S and R_S are the capacity and resistance of the investigated material

the block scheme of the circuit is shown. The quantity τ can be evaluated by measuring the circuit response in the time domain after a step excitation [42]. Both the capacitors C_S and C_A are supposed to be uncharged. At time t=0 a signal step is applied resulting in a charging in the capacitors. For t>0 the capacitor C_S is starting to discharge because of the voltage crossing the capacitor and simultaneously more charge is transported to C_A. The resistivity can be obtained by measuring the charge Q(t) flowing into the capacitors, by means of a charge sensitive amplifier. The relation between the resistivity and the charge is:

$$\rho = \frac{Q(0)\tau_e}{Q(\infty)\epsilon\epsilon_0} \tag{3.27}$$

Where τ_e=$R_S(C_A+C_S)$, this quantity can be obtained by the measurement of the time dependent charge distribution. The measurements on IMEM CZT samples were done by the Physics department in Prague under the supervision of Dr. E. Belas.

3.8 CZT Spectroscopy

Charge transport inside a semiconductor detector is characterized by a large number of parameters like drift velocity, charge carriers mobility, trapping and detrapping time. All these parameters contributes to the device quality. The operation of a radiation detector depends on the way the radiation interacts with the detector itself. The main interaction mechanisms for a gamma ray with a radiation detector are:

- Photoelectric absorption : in this mechanism the photon undergoes an interaction with the absorber atom and it completely disappears. In its place a photo-electron is generated from one of the atom bond shells

- Compton scattering : the Compton scattering is the predominant interaction for gamma ray energies typical of radioisotope sources. The photon interacts with an electron of the absorber.

- Pair production : the pair production process is only possible if the gamma ray energy exceeds twice the rest mass energy of an electron. It's not seen in with the standard radiation sources.

By crossing the absorber material the photon interaction with the medium produces an exponential attenuation. The attenuation is given by μ called the linear attenuation coefficient. The exponential decay is given by

$$\frac{I}{I_0} = e^{-\mu t} \tag{3.28}$$

where I is the number of transmitted photons, I_0 is the photon incident flux on the surface and t is time. The photon can also be characterized by the mean free path:

$$\lambda = \frac{\int_0^\infty x e^{-\mu t} dx}{\int_0^\infty e^{-\mu t} dx} = \frac{1}{\mu} \tag{3.29}$$

The mean free path represents the average distance traveled trough the detector before the interaction takes place, it is equivalent to the reciprocal of the attenuation coefficient.

3.8.1 Energy resolution

For radiation detectors working at low temperatures the energy resolution is dominated essentially by the statistical fluctuation on the charge carrier generation. Noise is important only when working at low energies. For CZT, the contribution of noise is present also at higher energies. The various contribution to the peak broadening can be summarized as:

- Amplifier and detector noise, due to the electronic noise and the detector leakage currents

- The stochastic nature of the charge generation process

- Trapping - detrapping. Is the most important contribution for CZT detectors. The effect of trapping is constituted by a tail on the low energy side on the peak. In CZT, being the diffusion length for holes much smaller then the one of electrons, the trapping contribution is mostly

due to holes. The FWHM of a detector at a certain energy E_0 is given by:

$$FWHM = K(1-\eta)E_0 \tag{3.30}$$

Where K is a constant and η is the defect of a photon of energy E_0.

The first factor, the electronic noise, is independent of energy. Concerning the second, the statistical contribution is proportional to the square root of the energy of the incident photons. The third term is more complicated. In the case of low energy photons the interactions occur in a shallow region near the electrode, the charge collection is almost completely due to a single carrier type (usually electrons). In this case the contribution to the broadening of the photopeak is mostly due to surface recombination and trapping-detrapping in the inhomogeneous region near the contacts. At higher energies trapping is the most influent factor determining the peak. Once the charge carriers are generated inside the detector they will tend to migrated under the influence of the applied electric field until they reach the electrode or recombination takes place. Some impurities present in the material introduce energy levels in the forbidden gap far from the valence and conduction band and they are therefore classified as deep impurities. These impurities act as traps for charge carriers, the electron or holes are kept in the trap for a relatively long time. Even if the trap eventually releases the carrier, the time delay is sufficient to prevent the charge carrier contribution to the pulse shape. For a CZT detector the peak broadening at low energies is essentially due to the detector noise, at higher energies the incomplete charge collection is the most important contribution. Anyway the effect vary from device to device and it's strongly influenced by the contact deposition method (due to a different electric field profile) and the metal itself. For energy up to 100 KeV the FWHM is usually a good indicator of the detector performances, for higher energy it's also used the peak to Compton ratio, this is the ration of the maximum counts/channel in the photopeak to the average counts/channel in the Compton shelf. Another parameter used for determining the quality of the X-ray detector is the peak to valley ratio.

3.8.2 Pulse shape for a planar detector

If the charge carriers are generated within the active volume there will be a specific collection time for each kind of carriers, because each species must travel a fixed distance before it's collected. While calculating the shape of the leading edge (consisting of the induced charge as a function of time), it will be assumed that:

- All the charge carriers are created at a fixed point inside the active volume of the detector
- The effect of trapping and detrapping are ignored
- The electric filed is assumed to have the expected value inside the entire thickness of the detector
- The electric field is sufficiently high to ensure the full collection of the charge carriers

For a planar geometry detector irradiated with a radiation source the absorbed energy dE is given by the motion of a positive charge trough the potential difference $d\varphi$

$$dE = -q_0 d\varphi \tag{3.31}$$

In terms of electric field $\epsilon(x)$=- $d\varphi/d$x this is

$$\frac{dE}{dx} = -q_0\epsilon(x) = q_0\frac{V_0}{d} \tag{3.32}$$

where V_0 is the applied bias and d is the detector thickness. after the integration between the point x_0 where the charge are generated and the point x where the latter are collected. The drifting charges give rise to an induced charge on the electrodes that reduce the device voltage from the applied value V_0. The signal voltage will be:

In terms of electric field $\epsilon(x)$=- $d\varphi/d$x this is

$$\Delta V_R = \frac{q_0 V_0}{d} = \frac{q_0}{C}\frac{(x - x_0)}{d} \tag{3.33}$$

The induced charge will be

$$\Delta Q = C\Delta V_R = q_0\frac{(x - x_0)}{d} \tag{3.34}$$

The signal pulse can be hence described by the growth of a time dependent induced charge. The induced charge can be separated in two contributions, the hole and the electron part.

$$Q(t) = q_0(\frac{v_e}{d}t + \frac{v_h}{d}t) \tag{3.35}$$

considering the case where both electrons and holes are still drifting at the time t. After all the electrons and holes have been collected, the collected charge reach the saturation value q_0.

3.8.3 Charge Collection Efficiency

The induced charge at the electrodes is given by the contribution of the collected electrons and holes. One of the great advantages of CdTe compared to other high-Z materials is its relatively high electron mobility ($1100\frac{cm^2}{Vs}$ at $300K$). The hole mobility, on the other hand, is about 10 times lower. The CZT case is quite similar: the electron mobility is comparable to that of CdTe, while the hole mobility is lower. Despite the hole limited transport properties, CZT offers the advantage of an increased resistivity. The low value of hole mobility is nowadays one of the main limitations to the exploitation of CZT devices as gamma and X-ray detectors. Beside mobility, the $\mu\tau$ product (respectively mobility and life time of the charge carriers) is a good indicator of the transport properties of the detector. The poor transport properties affect in particular the high energy peaks, above 100 KeV, since those photons tend to cross the entire device, especially for thin samples,because of the exponential absorption of photons. The corresponding peak width is severely degraded with the increase of the energy since the attenuation coefficient diminishes and thicker devices are required [75] in order to reach a good collection efficiency. The degradation of the spectrum with the photon energy can be listed as follow [76]:

- the photopeak is not symmetric
- a tail is present on the low energy side of the photopeak
- the peak to valley ratio diminishes
- the photofraction decreases

All these effects are described by the Hecht equation [58] that expresses the collected charge fraction $\eta(x)$ as a function of the interaction depth x inside the detector:

$$\eta(x) = \frac{\lambda_e}{D}(1 - exp(-\frac{(D-x)}{\lambda_e})) + \frac{\lambda_h}{D}(1 - exp(-\frac{-x}{\lambda_h})) \tag{3.36}$$

where D is the device thickness and λ_e and λ_h are the mean free path for electrons and holes respectively. The interaction depth, x, is measured from the negative electrode. λ_e and λ_h can be expressed in terms of $\mu\tau$:

$$\lambda_e = (\mu\tau)_e \frac{V}{D} \tag{3.37}$$

$$\lambda_h = (\mu\tau)_h \frac{V}{D} \tag{3.38}$$

where V is the applied bias. The Hecht equation can then be correlated to the $\mu\tau$ product:

$$\eta(x) = \frac{V}{D^2}[(\mu\tau_e)(1 - exp(-\frac{(D-x)}{\frac{(\mu\tau_e)V}{D}}))] + (\mu\tau_h)(1 - exp(-\frac{-x}{\frac{(\mu\tau_h)V}{D}})) \quad (3.39)$$

The charge collection efficiency depends not only on λ_e and λ_h, but also on the interaction point, x, inside the device. Since the interaction point inside the device are essentially casual, depending on the exponential absorption law, the peak experiences a broadening essentially due to $\frac{\lambda_e}{D}$ and $\frac{\lambda_h}{D}$. To achieve an experimental evaluation of electrons and holes transport properties the most common method is to fit with Hecht equation the response of a planar detector under α-particle irradiation, on varying the applied bias, in condition of single-photon counting rate. Because the penetration depth of α-particles is only a few microns we select a single kind of carriers (either electrons or holes), then, fitting the data, we can use the single-particle Hecht relation [21]:

$$\eta(x) = \frac{V}{D^2}[(\mu\tau_e)(1 - exp(-\frac{(D^2)}{(\mu\tau_e)V}))] \quad (3.40)$$

By inverting the bias polarity we can select either electrons or holes, and, from the fit procedure, achieve the $\mu\tau$ product value. This procedure is also implemented with gamma and X-ray spectroscopy, but in this case, according to the radiation penetration length, we will use either the single carrier or the complete (two carriers) Hecht relation.

3.8.4 Gamma and X-ray spectroscopy set up

The study of the spectroscopic characteristics for IMEM grown CZT ingots has involved the preparation and the testing of more then 100 devices, representing a crucial part of the work in the understanding of the material properties and the implementation of the preparation technologies. The measurement were performed at INAF-IASF in Bologna under the supervision of Dr. E. Caroli. The samples were studied using the planar configuration, two symmetrical electrodes where deposited on the two surfaces covering the entire area in order to minimize the field distortion. A second configuration was studied consisting in the preparation of a planar contact on one side of the detector and the realization of a square contact surrounded by a guard ring on the other, the effect of different biases of the guard ring on the spectroscopic quality was studied.

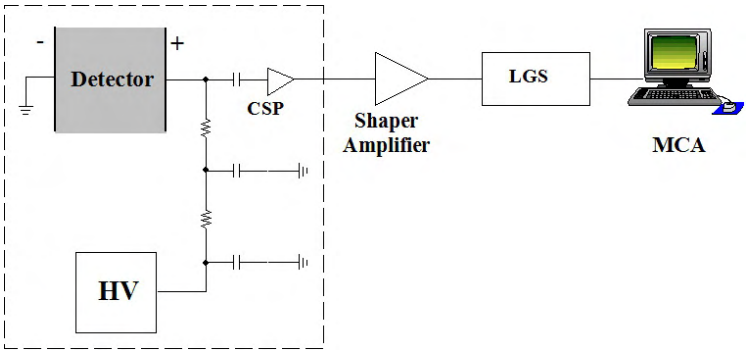

Figure 3.18: Schematic representation of the experimental set up for the spectroscopic characterization

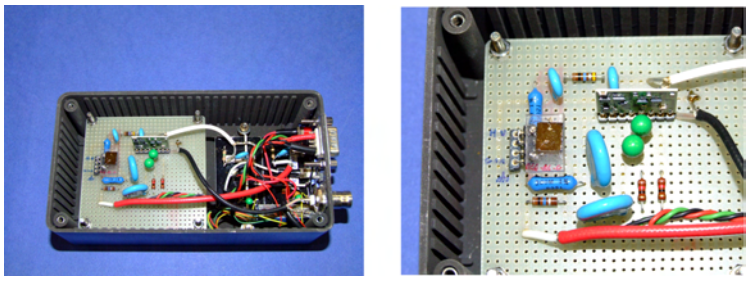

Figure 3.19: Schematic representation of the experimental set up for the spectroscopic characterization

The spectroscopic characteristics of the detectors were tested using a standard set up as illustrated in figure 3.18. The basic components are the CSP, charge sensitive preamplifier, a commercial eV-509 component, the amplifier, Ortec model 450, the LGS (linear gate and stretcher) Ortec model 442, the HV, and the MCA , multi channel analyzer. The sample is mounted inside a box, together with the preamplifier, in order to minimize the path of the signal before it reaches the preamplifier. The box used for the characterization is shown in figure 3.19, on the right is shown a photograph of the sample inside the measurement box. The box has particular support that allows the mounting of the sample in two configurations: the planar parallel field (PPF) and the planar transverse field (PTF). In figure 3.20 are shown the two configurations. The two differ for the way the radiation interacts with the detector material. For the PPF configuration the beam impinges the top surface and interacts with the material generating an exponential decay and it's fully stopped at a certain distance from the entering electrode depending on the photon energy.

In the PTF configuration instead, the events are generated at every depth in the sample thickness. In this case the exponential decay occurs in the direction parallel to the surface area. The photons are generated in every position of the

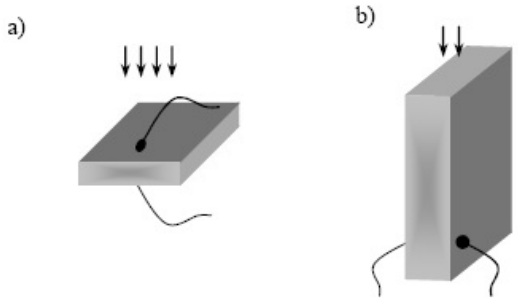

Figure 3.20: Two measurement configurations: planar parallel field (PPF) and planar transverse field (PTF)

thickness independently of the photon energy. In this configuration the carriers need to travel not a fixed distance before they are collected at the electrodes. In the case of the PPF configuration, for low energy photons, the carriers are generated near the entering electrode and the pulse height is composed mostly by one kind of carriers, the one that drift trough the device. In the second configuration, both species are contributing to the peak formation. The radiation sources used for the spectroscopic characterization are covering the energy range up to almost 400KeV.
The ^{241}Am source has several X-ray emissions between 13.9 and 20.7 KeV with intensities up to 9.6 %, and a gamma emission at 59.5 KeV with intensity of 35 %.
The ^{109}Cd source has two very intense emissions very close to each other at 21.9 and 22.2 KeV (the sum of the two intensities is 85.2 %), the second intense emission is a gamma of energy 88 KeV with a lower intensity, 3.5 %.
For the ^{57}Co source the X-ray emissions are at very low energies (circa 7 KeV) and their contribution is covered by the noise, the gamma emissions are instead visible: 14.4 KeV, 122 KeV and 136 KeV, the most intense one is the 122 KeV that reaches 85 %.
A ^{133}Ba source was also used, the emissions of Ba are at higher energies with respect to the other. The most intense X-ray emissions are at 30.6 and 30.9 and the emission at 34.9. The gamma emissions are at 81 KeV, 276 KeV, 302 KeV and 384 KeV. At these energies the Compton shelf is present and it's possible to see the efficiency of the detector with this different interaction mechanism.
The spectra acquisition was performed without the collimation of the sources, The source was positioned at a distance between 3 and 5 cm to the top of the measurement box. In this configuration the entire surface of the sample is illuminated during the measurement. The same setup and measurement box

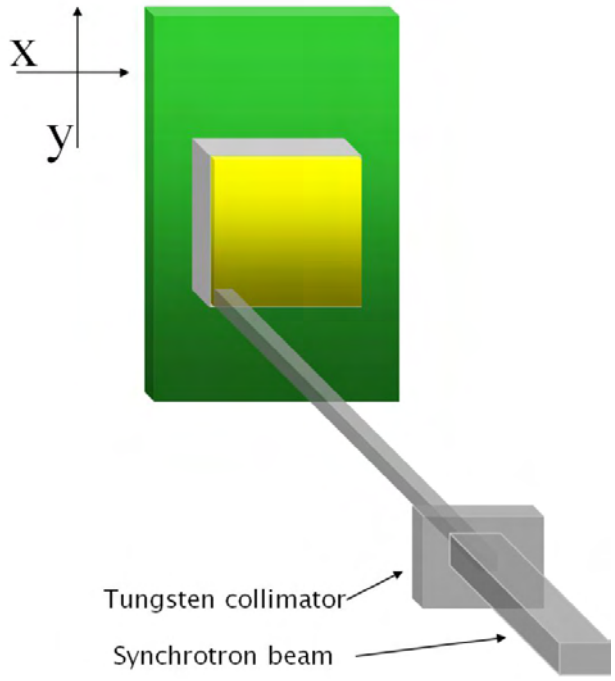

Figure 3.21: Scheme of the measurement setup at NSLS, for the X-ray response map acquisition. The beam energy is between a few and 30 KeV, the collimation is usually 20 x 20 μm or 10 x 10 μm [77]

was also used for the $\mu\tau$ product measurement. The transport properties were measured mainly with an alpha particle source, but the same measurement were performed using the 22KeV emission of the ^{109}Cd source. This particular X emission is at very low energy and hence, and as for the alpha particles, the approximation of the carriers to be generated at the electrode is satisfied.

3.8.5 X-ray response mapping set up

At the National Synchrotron Light Source (NSLS) facility in BNL, a beamline is dedicated to the study of the devices inhomogeneities. The aim of the measurement is to measure for every point interrogated the peak position, and hence the charge collection efficiency, of the device. For a single electrode the result is a map of the response, if the electrode design is more complicated,like a multipixel geometry, the measurement can also give information about the electric field inhomogeneities by looking to the distortion in the reproduction of the contact geometry in the X-ray image. The experimental setup is represented in figure 3.21. The sample is mounted inside a holder, on one side a berillium window allows the illumination of the sample. The X-ray beam is collimated with a tungsten collimator, with dimensions down to 10 x 10 mi-

cron. The movement of the sample is automatically controlled from the PC in the x-y-z directions. The X-ray beam can be tuned from a few up to 30 KeV. In every point interrogated an X-ray spectrum is acquired for 0.5 seconds, this time is sufficient for the creation of a well defined photopeak, since the synchrotron flux is high. The preamplifier is a commercial eV-550 low noise charge sensitive device. The main amplifier used is a Ortec 672. The applied voltage can be tuned from tens of volts up to 1200 V for very thick devices.

CHAPTER 4

Experimental results: material characterization

4.1 PL mapping

4.1.1 Zn segregation

The growth mechanism of the CZT requires particular attention and a careful study of the thermodynamic of the system. One of the key factors is the study of the Zn composition along the crystal axis. For every impurity the concentration in the melt and in the solid is given by:

$$K = \frac{C_s}{C_l} \tag{4.1}$$

K is the segregation constant and depends from the ratio between the concentration in the solid and the melt. In CdTe, considering the Zn element, K≠1 [54], so the concentration of Zn in the crystal is not constant, but it changes following the normal gradient freeze equation:

$$x(g) = Kx_0(1-g)^{K-1} \tag{4.2}$$

In equation 4.2 g=z/l is the crystallized molar fraction of the material, while x_0 is the starting Zn concentration in the liquid. This equation is also known as the Pfann equation [44]. By observing the curve, it's clear that the last to freeze part present a high compositional gradient and it's hence a particularly not uniform part in the ingot (regarding the composition). This characteristic has a strong influence in the selection of the material for the realization of radiation detectors, being the properties in the ingot dramatically different from the tip to the bottom part of the crystals.

CZT alloy stoichiometry is not uniform along the ingot, being Zn segregation coefficient larger then 1 (1.35 as indicated in [52]). The near band edge emission of the Pl spectra can be helpful in the identification of the Zn composition for every point in the ingot. The position of this peak is in fact related to the energy gap value and hence to the Zn via the empirical relation [43]:

$$E(x, 77K) = 1.586 + 0.5006x + 0.2969x^2 \tag{4.3}$$

The bowing parameter deduced in 4.3 is obtained from the FWHM of the principal bound exciton peak in the PL spectrum. First, some PL single spectra will be shown, for a better understanding of the PL mapping building mechanism. A 4.2 K spectrum acquired at IMEM institute from a CZT In doped Crystal is shown in 4.1. In the near band edge region, for IMEM samples (A_0, X) is the tallest peak, this is probably due to the growth technique and the doping concentration. Because of the great degree of alloy broadening with x=0.1, with respect to lower Zn concentrations e.g. x=0.04 [20], the free excitons are not resolved in the plot . In the second region are present the (D, A) peak and two phonon replicas. The third region shows the typical A-center band. Although low temperature PL can give extremely useful informations on the crystal quality and the defect structure, for a large scale mapping of the ingot a 77K spectrum is sufficient for the calculation of the Zn content. In fact the error due to the convolution of the (D_0, X) and the (A_0, X) peaks is negligible. The typical spectrum obtained from one IMEM grown CZT sample at 77K is shown in figure 4.2.

The near band edge region presents a dominant peak, representing the bound excitons contribution, and a (D,A) peak, very close to the main peak. The A-center is clearly visible in the lower energy region. this spectra are used for the mapping of the samples. For the realization of a PL map, the ingots are cut parallel to the growth axis, in order to have complete information of the entire length of the ingot. The surfaces of the samples are carefully polished in order to obtain a homogeneous surface quality. The slabs are then positioned in the cryostat. The adhesion of the sample to the Cu cold plate is crucial for the homogeneity of the sample temperature and hence the response. The adhesion is ensured by the use of Cu pins, a strong increase of the PL intensity has been related to the use of Cu pins, moreover by avoiding the use of grease the presence of impurities is minimized. The cryostat used in the the PL set up allows measurements of samples up to 5 cm x 5 cm. This size fit perfectly the dimensions of the 2 inches diameter CZT ingots grown at IMEM. In the PL set up in IMEM the laser is moved, while the sample is steady. The Bruker "OPUS 6.5" software is connecting the FTIR to the computer interface,

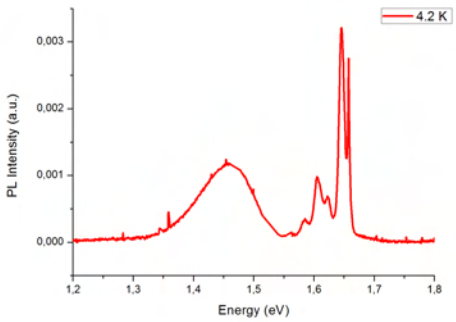

Figure 4.1: The peaks identified as the first region in 4.1, at 4.2K, are now a convolution centered in between the (D_0, X) and the (A_0, X) position. The contribution of the second region, dominated by the (D,A) is present as the shoulder of the main peak. The big band centered around 1.4 eV is the A-center. The 1.1 eV band is not present in this spectrum, because the Si diode is not detecting in that area. From measurements using the InGaAs detector, it emerged that only a small number of IMEM samples shows the 1.1 eV peak.

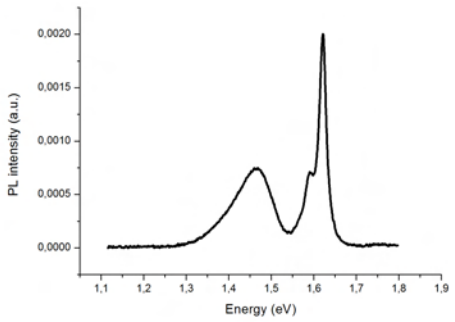

Figure 4.2: A 77 K spectra of an IMEM sample. The spectra acquired at liquid nitrogen temperature are used for the realization of PL maps

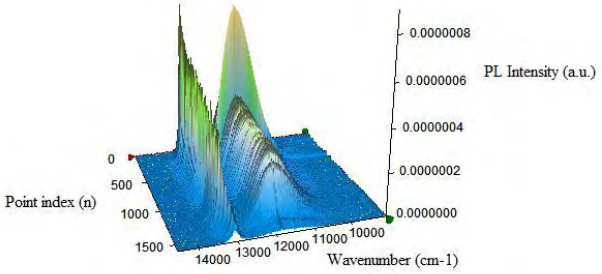

Figure 4.3: The result image of the PL mapping without any elaboration

the software also controls the movement of the laser. By running a macro, the software acquire the PL intensity spectra from a defined area of the sample, the parameters of the measurement (number of scans and the energy range) are also controlled with the "OPUS 6.5". Since the measurement should be the shorter possible, in order to minimize any possible effect of heating generated by the laser, the number of scan per point chosen is 10, the resulting spectrum shows a low level of noise. The software output plots all the spectra in chronological sequence, as shown in figure 4.3.

The *Opus 6.5* software contains many functions for the spectra processing: integration, peak picking, spectrum subtraction and several others mathematical tools. For the calculation of the Zn fraction, a near band edge emission area is selected and a peak picking routine is run on that specific area. The peak picking selects the maximum in the chosen region for every spectrum and then reconstruct a map. This map has in the x-z plane the actual sample size and in the y axis the position of the maximum of the near band edge peak. By using the 4.3, the position (in eV) of the peak can be easily transformed in the Zn composition, usually expressed in %. In figure 4.4 the radial segregation is calculated, from a wafer cut perpendicular to the growth axis. The radial homogeneity is very good, the differences in Zn concentration present in the image are due to a poor alignment between the crystal axis and the cutting wire. In fact the gradient is not form the center toward the walls, but from one side to the other of the wafer. In 4.5 is shown a PL map of a slab, after the elaboration. The Zn concentration is calculated on the entire length of the ingot. For time reasons, only half of the slab is measured: in fact the other part should be symmetrical.

In the first to freeze part, the top in the left image of 4.5, the Zn profile does not follow the normal freeze equation. In fact an increase of the Zn concentration is observed in the first to freeze part, up to 2-2.5 cm from the tip

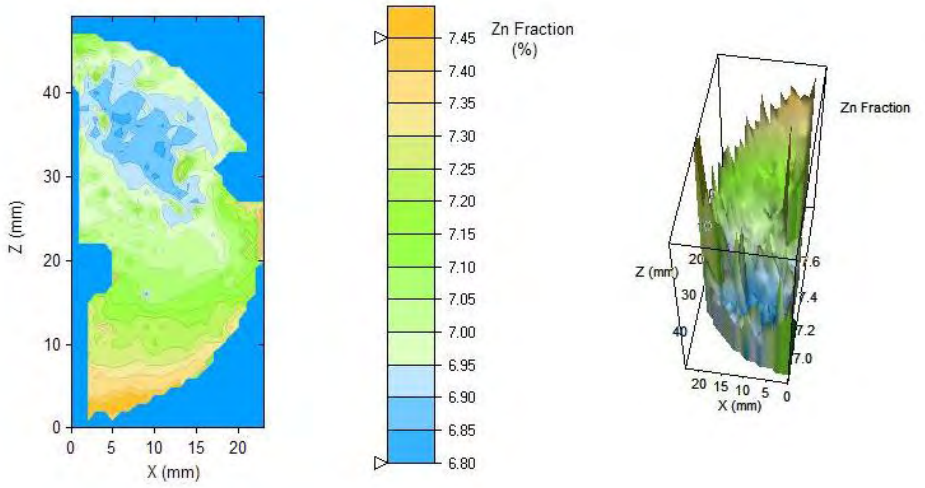

Figure 4.4: 2D and 3D image of a CZT wafer, the radial segregation is absent, the inhomogeneity is due to a misalignment between the growth axis and the saw during the cutting procedure

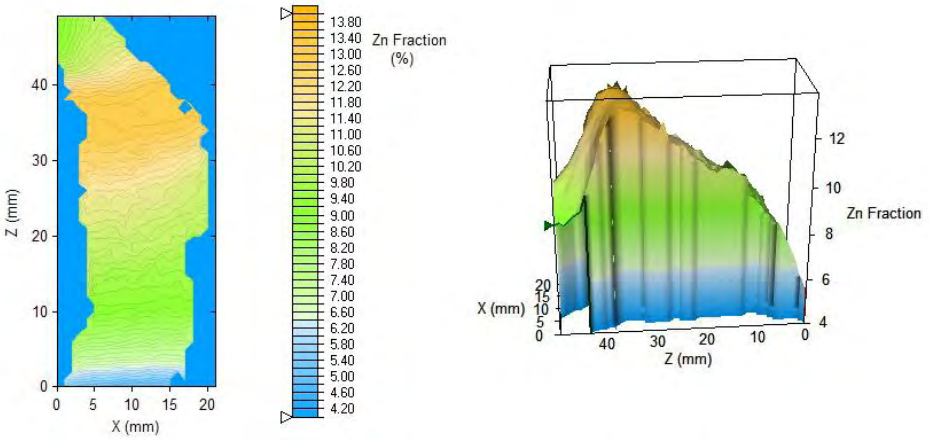

Figure 4.5: Zn concentration in a CZT ingot, the program creates a 2D and 3D image

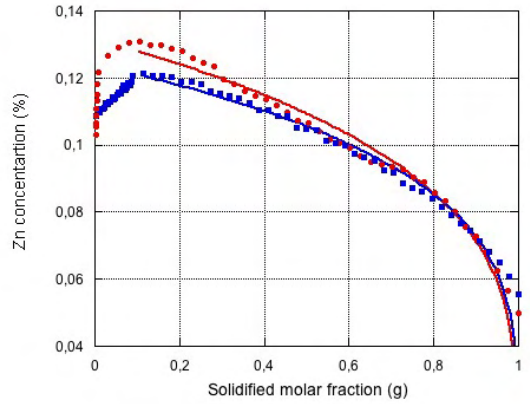

Figure 4.6: Comparison of the Zn profiles obtained for two different ingots

[49]. This behavior can not be explained with the normal freeze equation. Several slabs were measured, this characteristic is present independently from the growth technique: with or without the boron oxide encapsulation. The same profile has been reported by several authors, in literature [72, 73, 46, 74, 20]. It is usually explained as a supercooling effect occurring in the early stages of the growth. A seeded growth for CZT crystals is not possible, when growing from the melt, due to tellurium structures, called *polymers*, present in the melt. Before the growth starts superheating is necessary in order to remove tellurium structures, that are known to be present in the melt. This means that the growth starts from a superheated melt. The supercooling of the melt is about 20°C, before the crystal growth starts. Being the typical thermal gradient of the CZT growth about 10°C per cm, the effect of the supercooling is supposed to appear in the first 2 cm of the ingots. The crystal growth is very rapid, the Zn concentration does not fit with the phase diagram (1.35 times the concentration in the melt), but is equal to the Zn concentration in the melt. After that, the equilibrium is established and the theoretical behavior is followed. Since the first part is grown in such unstable conditions and the growth is very fast, supercooled growth is characterized by a highly polycrystalline structure. Some of the authors are actually reporting that the crystal structure in the first part of the crystal is polycrystalline. However, studying the data in figure some comment should be done. The Zn concentration in the first points of the tip is not exactly the one of the melt: in 4.6 the Zn concentration in the melt was 10% and 9% but they both start the the growth at about 7%. The same feature can be found in the data reported by other authors, but it's never explained or discussed. The melting temperature increase monotonically with

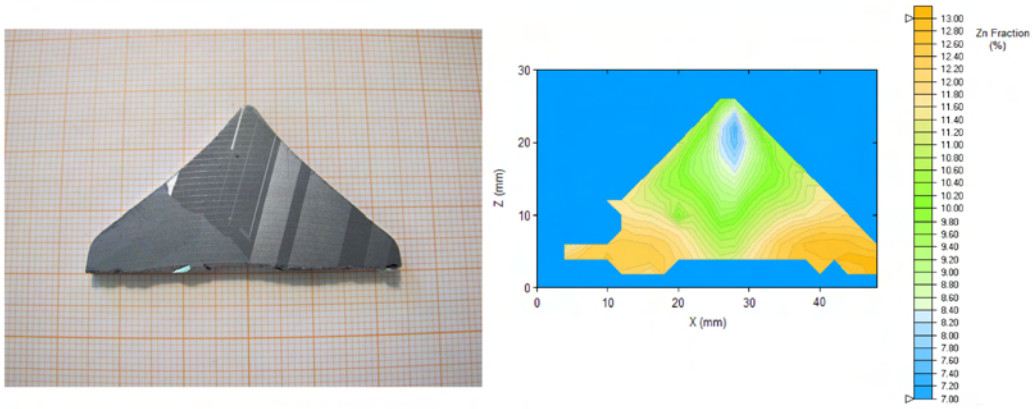

Figure 4.7: A photo and a PL map of the tip of a CZT ingot.

the Zn concentration in the CZT alloy, so there is no reason why the tip should be solidified with a concentration lower then the melt. For a better study of the first to freeze part of the ingot, some maps were acquired only on the tip of the ingots. In figure 4.7 is shown the PL map of a CZT tip. As shown on the left part of 4.7, the tip of the ingot does not shows the typical crystalline shape of the undercooled melt. The tip is in fact almost all single crystal, with the presence of some twins, starting from the near tip region. It is very difficult to image that that grain has developed under supercooling conditions, the fast growth origin a dendritic growth.

A supercooled tip is like the one shown in figure 4.8, the first part of the growth is so fast that the crystal is completely polycrystalline. Moreover, if the tip undergo a supercooling, the Zn profile should present a step-like dependence. Eventually, due to solid state diffusion, the step could be softened as described in figure 4.9. The final curve should be in any case concave. On the contrary the experimental data show a convex shape (figure 4.6). Again the same convex shape was present in the work of other authors. These comments on the Pl maps and Zn profiles cannot be explained as effects of the supercooling. A possible explanation can derive from the occurrence of a not uniform distribution of the zinc in the melt before crystal growth starts. This phenomenon can be related to the Soret effect, this effects concern gas and liquids mixtures. When several elements are present in a liquid and a thermal gradient is imposed to the system, the elements react differently to it. In the case of CZT Zn is a lighter element, with respect to Cd, so it tends to move away from the cold part, usually the tip of the ampoule. However, Soret effect is usually observed only in particular conditions, like in microgravity, when the effect of convection can be neglected [45]. In the case described in the paper,

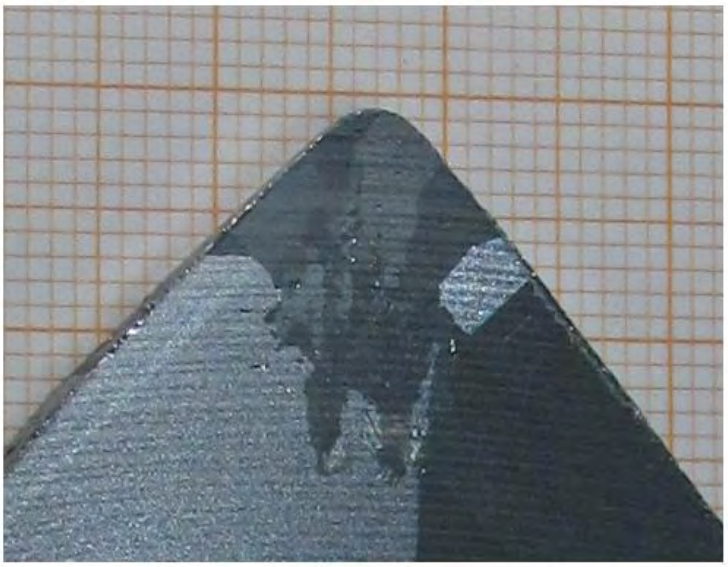

Figure 4.8: Dendritic structure resulting from the supercooling occurring in the early stages of the growth.

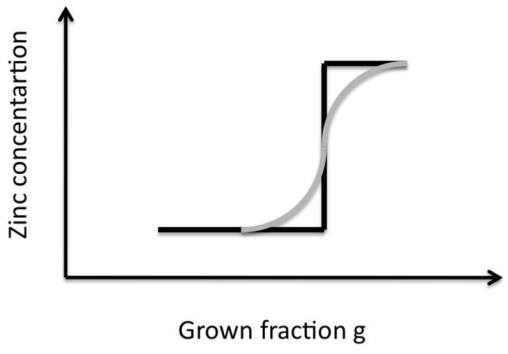

Figure 4.9: Expected dependence of the Zn concentration on the growth fraction according to the supercooling model taking and not taking into account the solid state diffusion (respectively gray and black line).

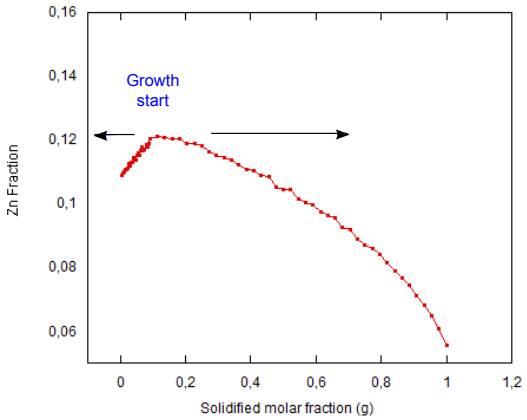

Figure 4.10: Explanation of the observed Zn profile: the growth starts at the maximum and then proceeds in two directions, toward the bottom and toward the tip of the crystal.

the thermal gradients used are much larger then the one used for the CZT crystal growth. Moreover the Zn-Cd mass difference is not so high to explain such a dramatic effect. The Zn profile can be described by formulating the hypothesis that the first nucleation does not start, as expected, form the tip of the ampoule, but from the ampoule wall, in correspondence of the maximum in the Zn concentration. This explanation can describe the convex shape of the first part of the Zn profile. In fact the growth starts from the walls, where the ampoule changes from cone to cylinder, and then continues in the two directions: toward the bottom and toward the tip 4.10. This also explains why the growth starts at a Zn composition different from the equilibrium composition in the melt. According to the normal freeze equation it is possible to have a final concentration lower then the the starting concentration in the liquid phase. Moreover, since the supercooling is not dominant at the beginning of the growth, there is no reason why the growth should start whit an almost single crystal as shown in 4.7.

If we assume that the growth starts from the walls, it is possible to observe multiple nucleation sites on the walls 4.11. This behavior is also reported by other authors [46].

The first solidification seems to start in almost all the crystals that were studied from the same position in the ampoule: where the shape of the ampoule changes from cone to cylinder. Two possible reasons where suggested: first, at high temperature the energy is mainly enhanced by light, the quarts wall acts

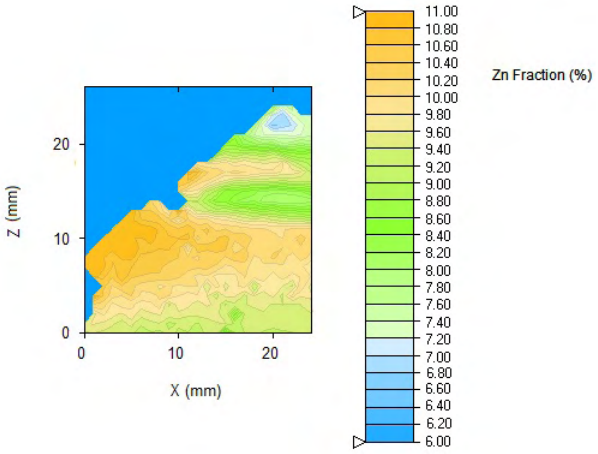

Figure 4.11: Crystal tip showing multiple nucleation sites on the ampoule walls.

therefore as a waveguide for the radiation, the tip of the ampoule is on the contrary a singular point where the radiation experience a large reflection. The hypothesis is that the tip is for this reason overheated. The second hypothesis is that the ampoule thermal gradient is influenced by the support on witch the ampoule is positioned. this effect is larger if the support is made of a material with a high thermal conductivity. This second hypothesis is supported by recent studies on the influence of the material employed for the support of the ampoules. [47]

4.1.2 Study of the interface shape by using the PL mapping system

The PL mapping system can be also used for the study of the growth interface. Crystals are grown at IMEM using two different variations of the Bridgman technique. In the first case boron oxide is introduced in the ampoule before the crystal growth starts, boron oxide melts and encapsulates the molten CZT. In the second case the growth is performed in low pressure condition, with a closed ampoule. In the first case the sealing of the ampoule is not necessary because the boron oxide prevents the evaporation of the volatile elements (mostly Cadmium) and a good stoichiometry. A scheme of the two growth methods can be found in figure 4.12.

The furnace is the same for both the techniques. It is well known the importance of the growth interface on the single crystal yield, in fact, due to convection and the small thermal conductivity of CZT, the creation of a concave interface is encouraged. Near the walls the wetting is instead dominant:

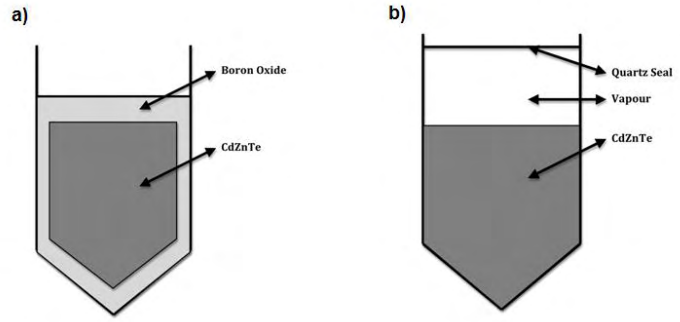

Figure 4.12: Scheme representing the growth ampoule for : a) Boron oxide encapsulated vertical Bridgman technique, b) Low pressure vertical Bridgman

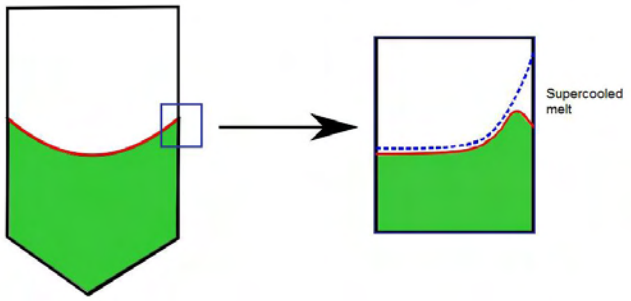

Figure 4.13: The wall-melt interface may produce a superccoled melt region, leading to the formation of polycristalline crystals

in this case a convex interface is favored. If the melt interface is mostly concave, the wetting is creating a supercooled zone of melt near the walls. This situation promotes a polycrystalline growth 4.13.

The interface shape can be studied by analyzing the same PL maps used for the Zn segregation study. In fact the Zn concentration change corresponds to an increment in the solidified fraction. The lines connecting the points with the same Zn content are also representing the growth interface at that point of the growth. Several IMEM grown CZT ingots were studied. The influence of the boron oxide encapsulation was deeply studied and it was found that the boron oxide melts and completely cover the molten CZT during the crystal growth. This has a strong effect on the growth interface because a separation is present between the melt and the vapor phase.

In figure 4.13 is shown a PL map acquired on a half slab of a CZT ingot. The maps is showing the Zn profile and hence the growth interface. The ingot was grown with the boron oxide encapsulation. The interface is clearly convex. The same shape can be found in all the CZT ingots grown with the same technique.

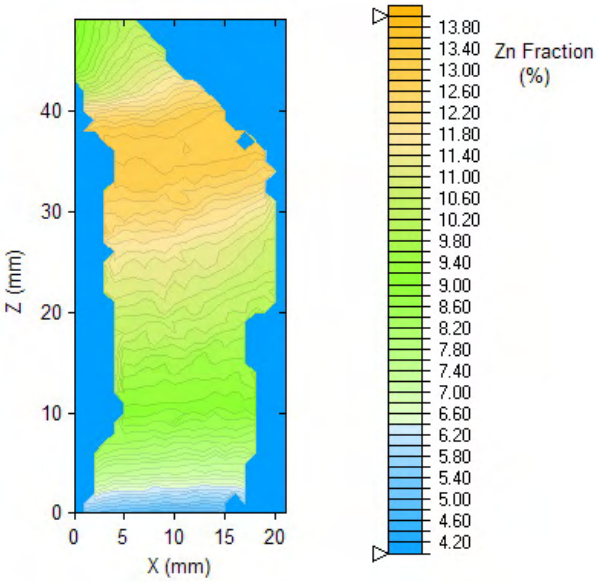

Figure 4.14: PL map of a CZT ingot grown by the boron oxide encapsulated technique. The growth interface is convex

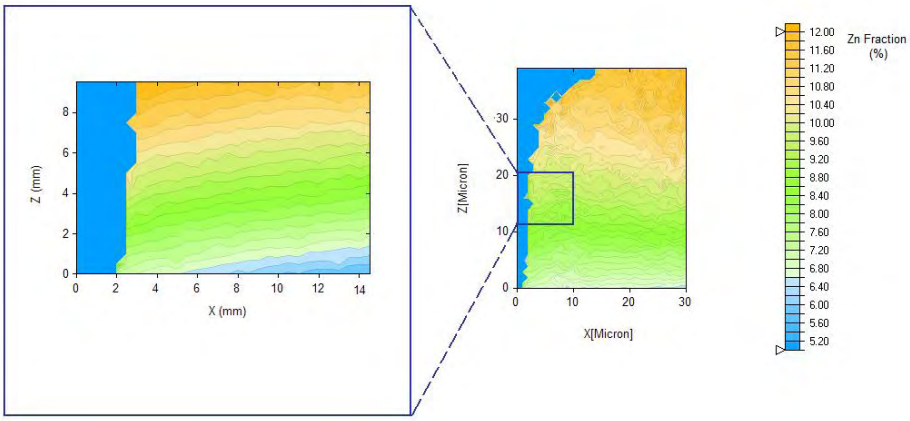

Figure 4.15: A PL map of a CZT ingot grown with the low pressure Bridgman technique. The growth interface is concave, on the left of the picture, is shown a magnified region near the ingot surface

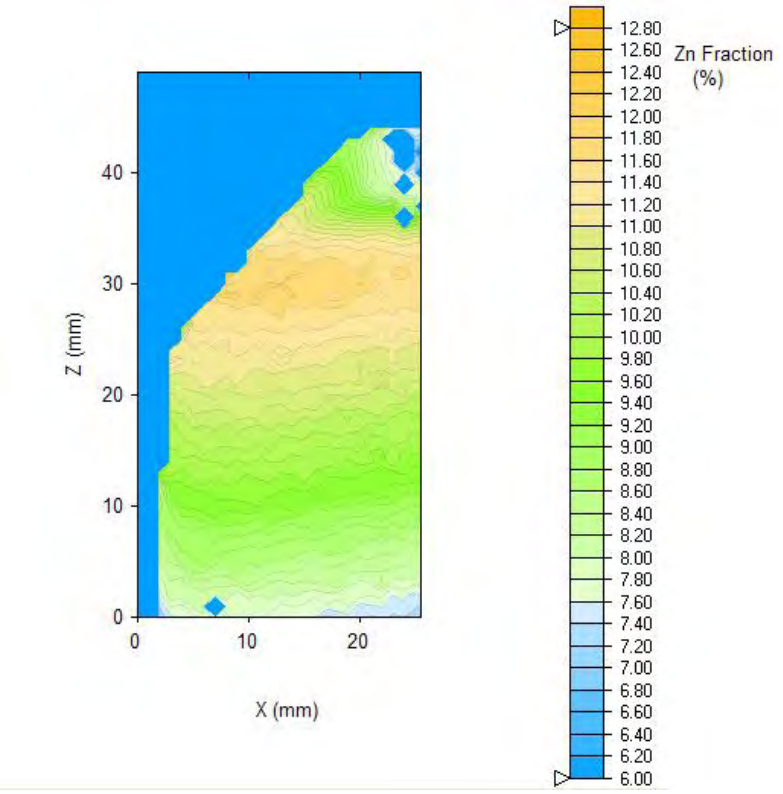

Figure 4.16: A PL map of a CZT ingot with the introduction of a quartz disk on the top of the melt. The influence of the separator is highlighted by the chance of the growth interface from concave to convex

For the crystals grown with the low pressure Bridgman technique, the behavior is different: the interface is concave, the same behavior was found for all the ingots. In this case there is free volume on the top of the charge. The growth interface seems to be strongly influenced by the presence of a layer on the top of the melt. The reason why the interface changes can be ascribed to the higher thermal conductivity of the boron oxide with respect to the one of the vapor or to the separation, done by the boron oxide, between the melt and the convective fluxes in the vapor phase. These experiments confirm however that it's possible to control the growth interface by changing the growth conditions. As a confirmation of the influence of a separator on the growth interface, the crystal growth was performed with a quartz disk on the top of the melt. This acts as the boron oxide by separating the vapor. In figure 4.16 the growth interfaces of a ingot grown with the quartz disk is shown: the interface is convex.

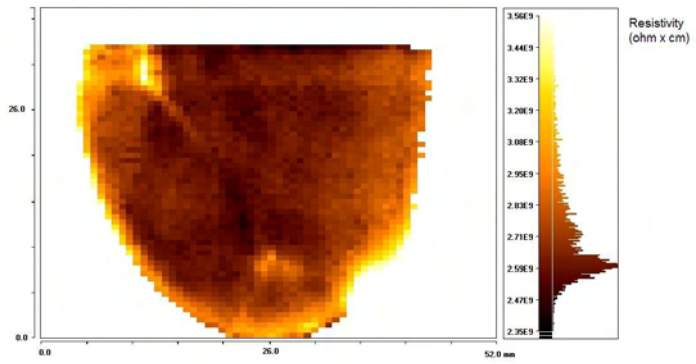

Figure 4.17: Co.Re.Ma. map of a CZT half wafer. By cutting the samples perpendicular to the growth axis the resistivity homogeneity is good. The lines present in the maps correspond to grain boundaries

4.1.3 Comparison between the Co.Re.Ma. map and the PL map

The Zn segregation along the growth axis implies a change in all the crystal properties. This has a strong effect on the homogeneity of the final device properties. It is very important, when a material characterization needs to be done, to analyze the material from different parts of the ingots, because the characteristics could depend on the position where the sample was cut. It is not easy to ensure a high degree of homogeneity also on the same slab. The Zn segregation profiles that were studied in the previous sections have a strong effect on the detector characteristics. By looking at equation 4.3 it is clear that the dependence of the gap on the Zn molar fraction is also influencing the resistivity of the material. The resistivity homogeneity can be studied by using the Co.Re.Ma. technique. A profound description of the technique is not provided in this thesis work, an accurate study of the method can be found in [42]. The measurements were performed in Prague at the Charles University in collaboration with the group of Jan Franc. The sample analyzed were cut in two geometries: parallel and perpendicular to the growth axis.

In figure 4.17 in shown a Co.Re.Ma map of a half wafer. The resistivity wafer is not very high ($310^9\ \Omega \cdot$ cm) because this wafer was cut from the middle of the ingot. The resistivity homogeneity is high, but several features are present. By comparing the Co.Re.Ma measurement with the wafer it's possible to correlate the lines present in the map with grain boundaries. The wafer in fact was not a single crystal. The Co.Re.Ma measurement is also confirming

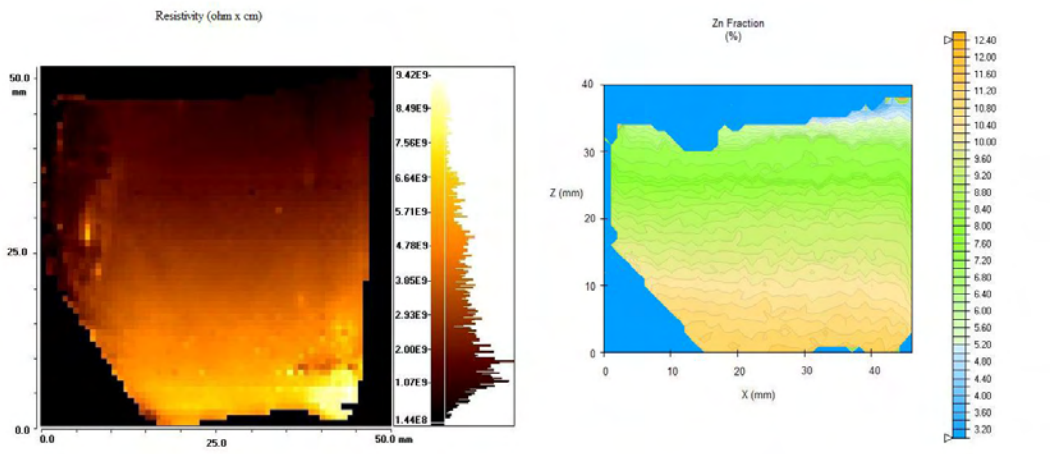

Figure 4.18: Co.Re.Ma. and PL maps of a CZT slab. The Zn gradient visible in the PL map correspond to a resistivity gradient in the Co.Re.Ma.

that there is no radial segregation in the ingots, since the only inhomogeneity can be ascribed to the poly-crystallinity of the wafer. The different contrast present near the wafer edge can be described as a border effect and has no physical meaning.

In figure 4.18 are shown the Co.Re.Ma and the PL map of a partial CZT slab. The area of the slab is about 5 cm x 5 cm, it does not contain the borders of the wafer. The two images show some similarities. In fact the Zn concentration decreases in a similar way with respect to the resistivity profile. The resistivity profile is following the E_g equation 4.3 and for this reason it's similar to the Zn profile, but the resistivity is also influenced by the dopant introduced in the growth. The compensation is in fact responsible for the high resistivity of CZT ingots. The dopant, as every impurity, has a segregation coefficient that determines the concentration along the ingot. CZT IMEM crystals are doped with In, the segregation coefficient for In is 0.11 [34] so it should give a contrary profile with respect to the one of Zn, giving a higher concentration of In in the last part of the ingot. The effect of Zn is much higher, also because the doping concentration of In is lower, so the resistivity follows mainly the E_g shift. In figure 4.18, in the Co.Re.Ma. map some features are present. Also in this map the features can be ascribed to the presence of extended defects, probably grain boundaries, these defects seem to have no influence on the Zn concentration.

4.2 X-Ray diffraction topography

X-ray diffraction topography is a very useful tool to understand the factors limiting the performances of CZT detectors. The technique is used to investigate the configuration of the lattice planes near a defect and the lattice misalignment in the presence of a differently oriented grain. CZT ingots are affected by the presence of several defects (Te inclusions, dislocations, grain boundaries, etc.), with the X-ray diffraction topography the crystal structure inside a sample can be studied with the acquisition of high resolution images. CZT samples were characterized using a X-ray beamline available at National Synchrotron Light Source (NSLS) at Brookhaven National Laboratory (BNL). The beamline uses a white beam with energy up to 50 KeV. As explained in the description of the X-ray diffraction topography measurement configuration, the images can be acquired by using several geometries, for every geometry different information can be obtained. The main differences in the X-ray diffraction topography response are between the images acquired in reflection or n transmission. The two configurations of the technique vary also in the energy used: for the transmission in fact a higher energy is required. Since the beam has to penetrate inside the entire thickness of the sample (for X-ray and Gamma-ray detectors the samples are usually between 1 and 10 mm), the energy should be at least 200 KeV. For the acquisition of reflected image usually a 50 KeV is sufficient to scan a region of about 40 microns near the surface of the sample. In the reflection geometry the images contain less information, with respect of the transmission, but are easier to analyze. In the transmitted image in fact the information belonging to all the thickness are diffracted in the same spot, resulting in the superimposition of too many features. For this reason the samples were studied only in the reflection geometry, moreover for IMEM samples the thickness is usually 1 or 2 mm, so by acquiring images on both sides a considerable region of the sample is studied. The sample does not require any particular preparation, the surface just needs to be accurately polished, since the technique is very sensitive to the presence of defects or non-uniformities near the surface that can change the local scattering power. The sample size can vary between a few millimeters up to 3-4 centimeters. For a better contrast in the image it's very important to tailor the beam area on the sample size and thickness, after the alignment the measurement is very rapid, it takes only 3-4 seconds. The diffracted spots are acquired by a high resolution X-ray sensitive film. The film is a 8 inches by 10 inches AGFA photographic film. The development of the impressed film follows a standard chemical photographic procedure. In figure 4.19 is shown a typical X-ray diffraction film, several diffraction spots are present, according

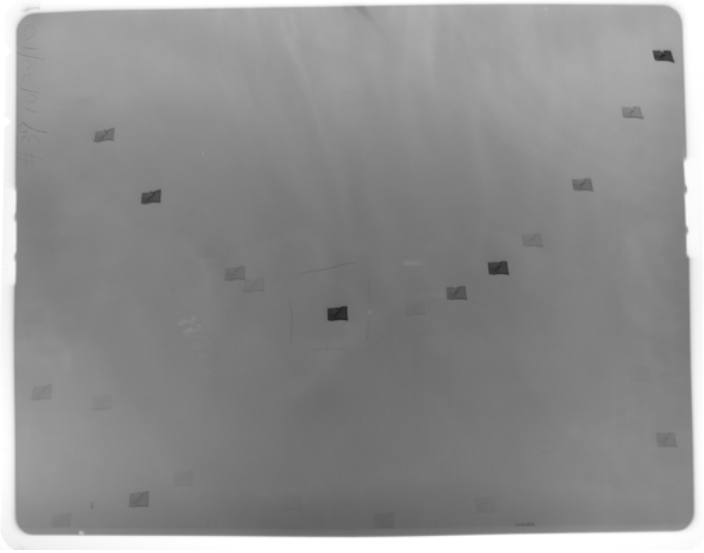

Figure 4.19: A X-ray diffraction film. The area of the film is 8 inches by 10 inches, the image was acquired in reflection geometry.

to the Bragg law of diffraction.

The diffraction spot with the best contrast is then selected and a magnified image of the spot is studied.

Grain boundaries and twins

In figure 4.20 is shown the diffraction topography of a CZT IMEM sample. The sample size is 7 x 7 mm, the thickness is 2 mm. The sample has a large grain boundary, that appear bright in the upper image. The grain is misaligned with respect to the rest of the sample and hence is satisfying the Bragg equation for a different angle, resulting in a shift of the diffraction spot. The diffracted grain boundary is visible on the right part of the sample, overlapped to the main diffraction. In the lower image of 4.20 the entire diffracted image of the sample is obtained by combining the two diffracted spots. The big features in the middle of the image correspond to the damaged introduced by the pin-hole for the IV measurement. Some distortion in the sample shape is present: this means there is unreleased stress in the crystal structure, probably due to a not uniform composition or to a damage introduced by the cutting procedures. An X-ray topography image showing the effects of the stress accumulated in the crystal is shown in figure 4.21.

The crystal structure of the sample is completely distorted by the stress accumulated in the sample. This type of topography image is found in ev-

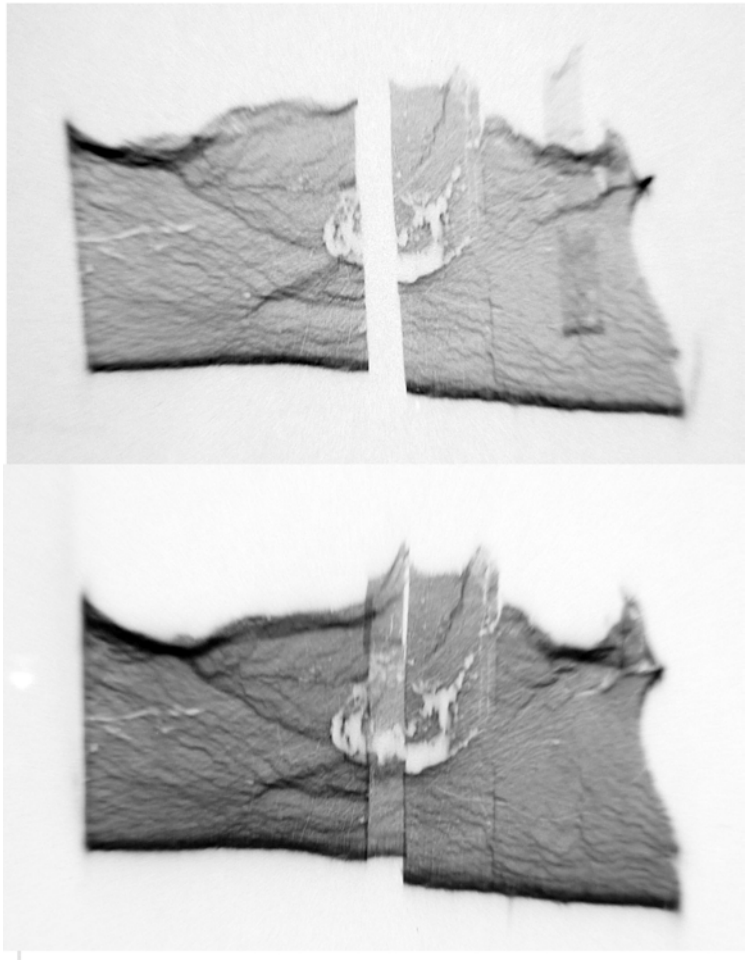

Figure 4.20: X-ray diffraction topography image of a IMEM sample. The white line in the upper image correspond to a lack of diffraction due to the presence of a grain with different orientation. The part corresponding to the grain boundary is reflected in a different position (it's visible on the left part of the sample, superimposed to the main reflection). In the lower image a combination of the two diffraction spot gives the entire image of the sample.

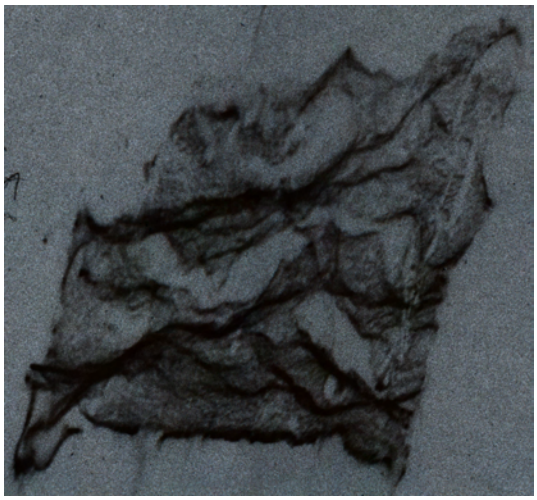

Figure 4.21: X-ray diffraction topography image of a IMEM sample showing the effect of the stress on the diffraction spot.

ery sample grown with the boron encapsulated technique, while the effect of stress is less severe for the samples grown with the low pressure Bridgman (for example 4.20). This strong deformation seems to be related with the growth technique, it can be probably be related to a fluctuation of the composition in a short range. The deformation is very uniform, covering the entire area of the sample. In such image the identification of defects is very difficult, since all the effects of grain or subgrain boundaries are covered by the distortion. On the theoretical point of view, the defects that can be identified with the X-ray diffraction topography are one-dimensional defects (dislocations) , two-dimensional defects (grain boundaries, see 4.20) and tri-dimensional defects (secondary phases, like Te inclusions and precipitates). In a real X-ray topography image, however, some of these contributions are very difficult to be identified. A single dislocation is in fact giving a contribution to the contrast that is too small to be seen in the image, the change in the scattering power near the defect is negligible. Anyway, the effects of dislocations can be seen in the topography image when the latter are arranged within surfaces and walls, originating a two-dimensional structure. The structures formed by multiple dislocation are usually called subgrain boundaries. The identification of such defects is very important for the properties of the final devices. These two-dimensional defects have in fact a severe effect on the charge collection properties, dislocations are usually electrically charged and can attract impurities and secondary phases. Subgrain boundaries trap carriers in a similar way as point defects do, by creating potential barriers and trapping the charge. Subgrain boundaries can be identified, in the X-ray topography image, because

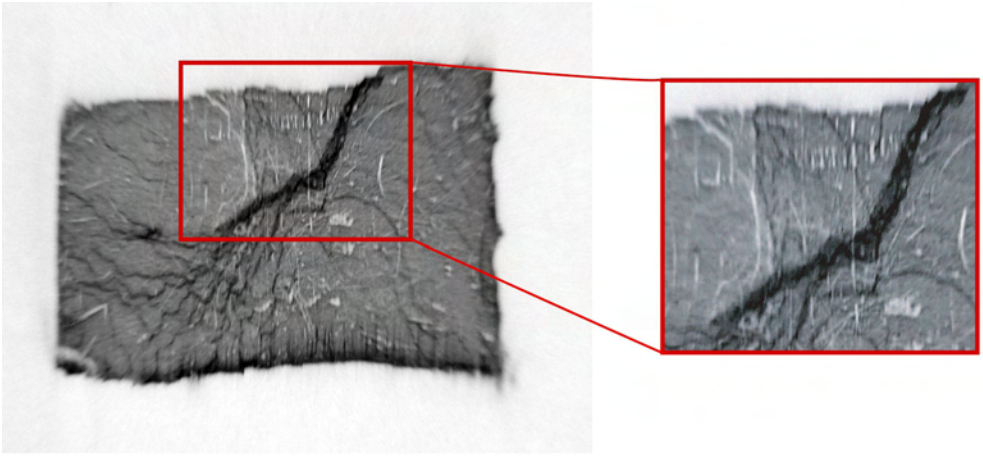

Figure 4.22: X-ray diffraction topography image of a IMEM sample, the well defined dark line in the middle of the sample is a subgrain boundary

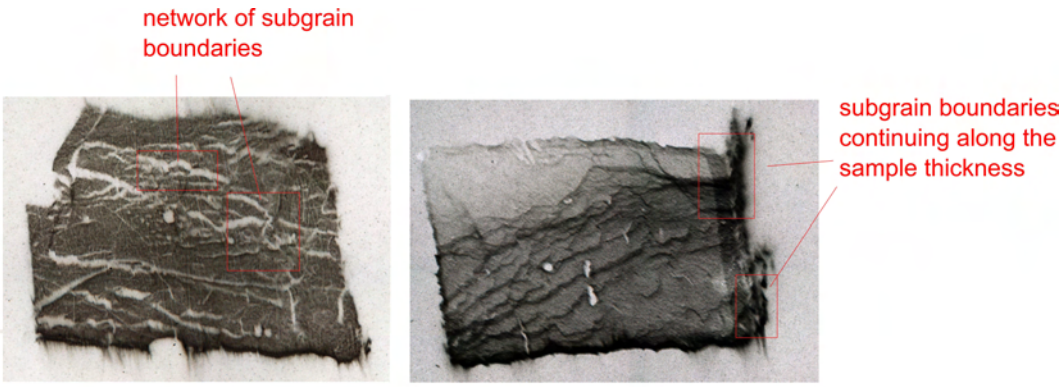

Figure 4.23: Two examples of subgrain boundary in CZT samples

they generates an extinction contrast in the image. The extinction contrast can produce very different effects on the topography image, in fact depending on the orientation of the extended defect with respect to the beam entrance surface. In figure 4.22 is shown a well defined grain boundary, with several smaller ramifications in the bottom part of the sample.

In this case the subgrain boundary appears darker with respect to the CZT crystal. This means that the deformation of the crystalline structure near the defect produces an overlap between the two emerging beams. The same type of defect can produce a bright feature in the case of the emerging beams to be separated by the interaction with the defect. In figure 4.23 the X-ray diffraction topography image of two sample are shown. In both cases the dominant defects that is present in the sample are grain boundary.

In figure 4.23, the picture on the left was acquired with a particular geometry that made it possible to see part of the lateral surfaces. Many subgrain boundaries in the image are crossing the sample in the entire thickness. In this case the defects can produce a strong deformation on the electric field leading to the shortcut of the contacts in the near defect region and the local cancellation of the detector response.

4.2.1 Study of the effect of post grown annealing on the crystal structure

The removal of Te inclusions present in the ingots is a current issue in the CZT technology. The lowering of the concentration and the reduction of the average dimensions of the inclusions is crucial for the quality of the CZT based devices. The standardization of a post growth annealing procedure for the removal of the inclusion has been attempted by several research groups. The annealing process in high temperature and in a Cd rich atmosphere, has been tested and it has been successful in the removal of all inclusions for long annealing time. The temperature necessary for the annealing process is above 600 °C. Unfortunately after the annealing the electrical properties of the material, in particular the resistivity, are deteriorated. So far no recovery process was successful in completely restoring the resistivity, that after the process decreases of several orders of magnitude. It is interesting to analyze the effect of the annealing on the crystal structure, since the temperature used in the annealing process can be up to 850 °C. The effect of annealing was studied on a EV Products sample. The sample sizes are 20 mm x 20 mm and 2,5 mm thickness. the annealing was working properly in the removal of the Te inclusions. In figure 4.24 is shown a IR image acquired with a 10x magnification before the annealing. In the image are clearly visible a large number of small Te inclusions. After the annealing almost all the Te inclusions are gone (figure 4.25), just a small number of very small inclusions are presents (the dark spots in the image are just dust on the sample holder).

In figure 4.26 is shown the WXDT of the same sample before and after the annealing process at 700 °C in Cd overpressure for 10 hours (plus 10 hours of cycle). In the left picture the topography image before the annealing shows some subgrain boundary, in the rest of the surface the sample is very uniform. After the annealing the WXDT image appear completely blurred, the crystal structure is completely destroyed by the temperature, the is no lattice order. This degradation interests only the surface layers of the sample, and after some deep polishing (about 200 μm) the crystallinity is restored. After the polishing

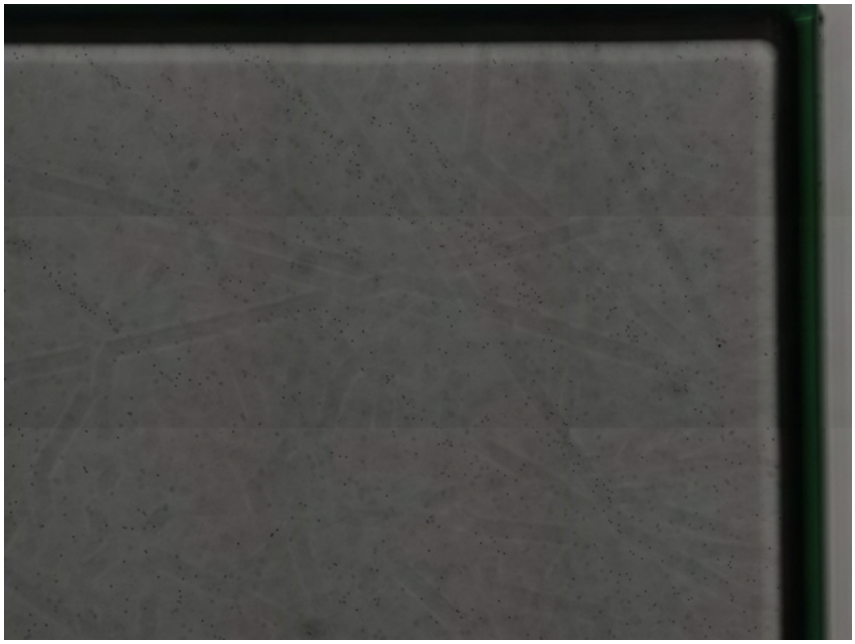

Figure 4.24: IR image of the top right corner of the sample

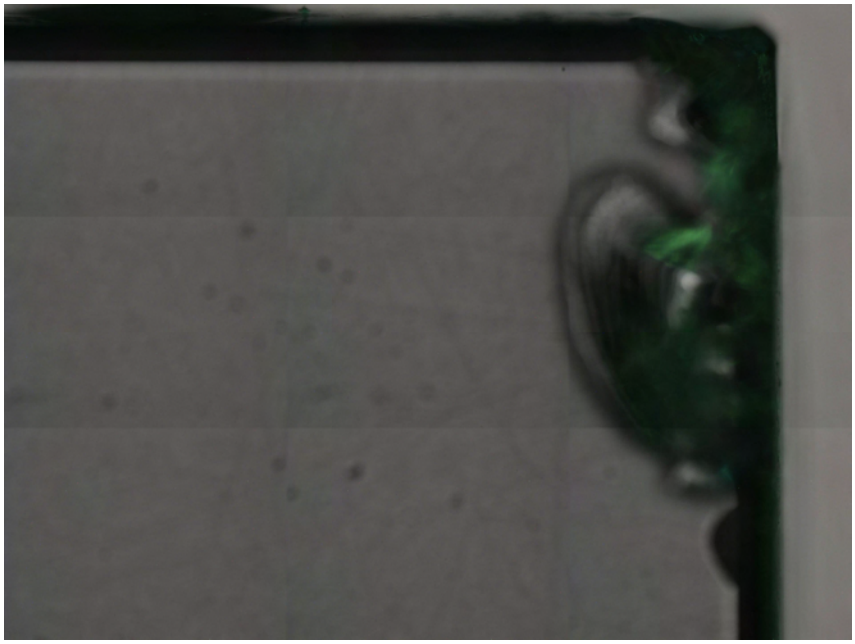

Figure 4.25: IR image of the top right corner of the sample

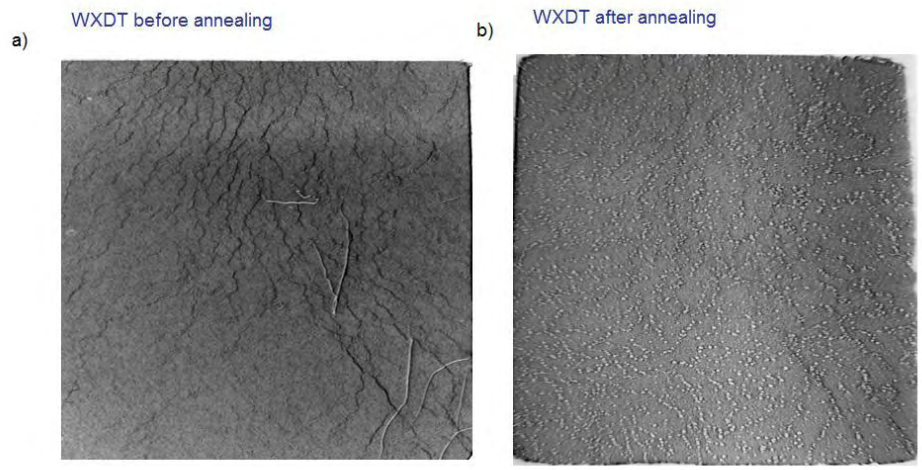

Figure 4.26: WXDT of a eV sample before and after the annealing process

the sample appears as in figure 4.26 part b), several defects are present now in the image. The holes-like features are the effect of the Te inclusions moving out of the CZT matrix. The movement of the Te inclusions produces a net of dislocations perpendicular to the sample surfaces. The annealing process is introducing bigger defects then the ones it's removing. The annealing process is therefore effective on the removal of Te inclusions, but heavily degrades the crystal structure of the sample. The same effect was found in all the samples annealed in high temperature, not depending on the growth conditions and technique.

4.3 IR microscopy

The device properties of CZT detectors are strongly affected by the concentration and size of the Te inclusions present in the CZT crystals. The density of Te inclusions, as well as their size, is strictly connected with the growth process. For the melt growth techniques it's very difficult to obtain an ingot with Te inclusions with a maximum size of a few micron, for the melt growth it's instead possible, but the growth rate is reduced drastically. The presence of Te inclusions can be monitored by measuring the equilibrium vapor pressure at high temperature. If the tellurium phase is present the total pressure is dominated by the tellurium vapor pressure, however with this technique all the information about the size and spatial distribution of the inclusions is lost. Moreover, this is a destructive technique, because the sample is completely pulverized. For an accurate study of the Te inclusions, the most versatile tech-

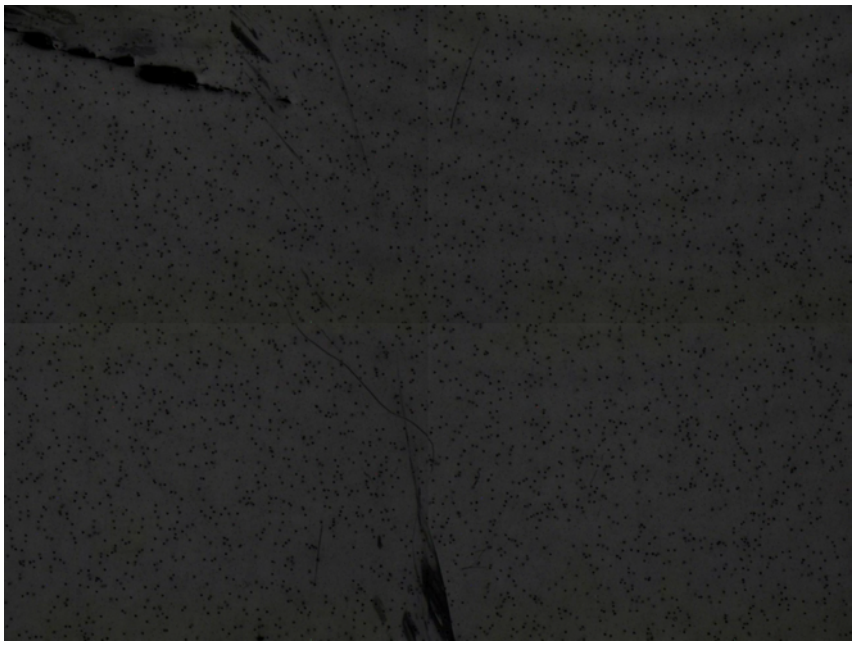

Figure 4.27: A collapsed image, resulting from the focusing on the same plane of several images acquired at different depth

nique is the near infrared (IR) microscopy. For the acquisition of the images a silicon camera is used, CZT is in fact transparent to the IR for energies below the energy gap, while the Te inclusions are opaque. The use of a specific software for the image reconstruction permits to obtain a composed image where are included the information on all the sample area and thickness. The main limitation to this technique is the depth of field of the image, that is limited by the objective lens, only a part of the inclusions are on focus in a single acquisition. CZT sample are usually very thick, several millimeters, and it's hence very important to obtain information about the entire thickness. This limitation was overcome by creating a collapsed image: in this case a set of images is acquired at different depth and then focused on the same plane.

The resulting image is shown in 4.27. All the Te inclusions are on focus in this picture. In figure 4.28 an entire CZT wafer is studied. the image is acquired in the middle of the sample thickness, using a 2.5x objective lens. The image is composed by multiple frames that are still visible in the image, the size of the frames depends from the objective lens used, in the case of 4.28 a) the frames are 3 mm by 2.2 mm. The acquisition of a large image add further information with respect to a single frame image. Figure 4.28 a) provides a complete map of all the extended defects present in the wafer, the analysis of the Te inclusions is instead secondary in this case. Grain boundaries attract secondary phases, as well as impurities, and hence are visible in the IR image. IR microscopy is then

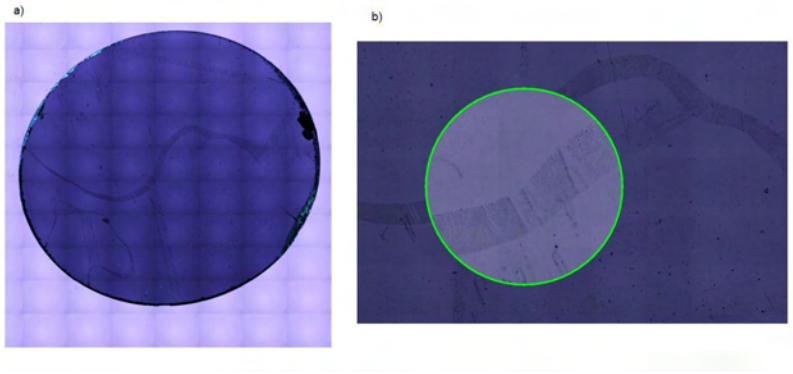

Figure 4.28: Infrared transmission image of a CZT wafer: a) image of the entire surface, Te inclusions decorate extended defects in the sample, grain boundaries and twins; b) magnification of a decorated grain boundary crossing the wafer

very important for the identification of the single extended defect. The large grain in figure 4.28 is crossing the entire thickness of the sample and is present from one side of the sample to the other, a magnification of the same defect is shown in figure 4.28 part b), the Te inclusions are here perfectly visible.

With the IR microscopy it is also possible to identify dislocations, the latter are in fact frequently decorated with tellurium inclusions. In figure 4.29 is shown a dislocation net present in a sample. A single dislocation, because of the small dimension, is usually very difficult to identify with WXDT.

The identification of the extended defects in a large wafer is very useful because it gives information where to cut the samples. In fact by naked eye it's not always possible to identify the presence of such defects, especially after the polishing procedure, rough surfaces in fact enhance the direction of the light scattered from the different crystallographic orientations. The effect of a grain boundary can be very heavy on the detector response. In figure 4.30 the effect of a well defined grain boundary (in the upper part of the sample) and twins (vertical, in the center); the response in the presence of the grain boundary is completely canceled. In the case of a single electrode detector, the total response of the device is the sum of the part with a good crystal quality and the part with almost no response, the resulting peak will be broadened by the second contribution; in the case of a pixel contact structure this can lead to the complete not functioning of some pixels. It is important to underline that the twin in image 4.30 is less decorated with Te inclusions with respect to the grain boundary and the charge loss in the X-ray response map is less pronounced. This is a confirmation of the trapping effect of the Te inclusions that is much higher then the effect of the extended defect itself. The selection

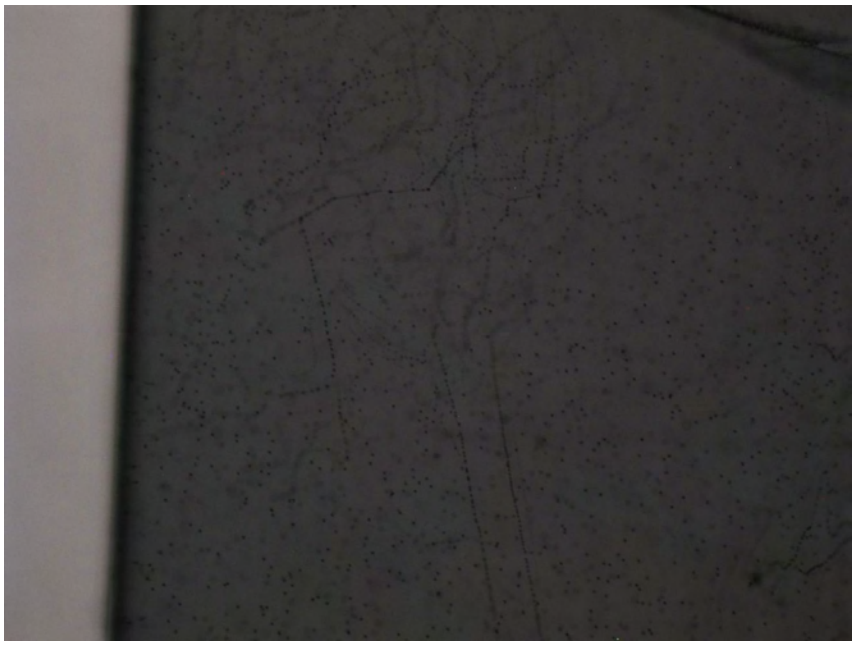

Figure 4.29: Dislocation patterns inside a CZT sample

of a completely extended defect free part of the crystal is therefore extremely important for the spectroscopic resolution of the devices. Te inclusions causes as well a loss in the charge collection. In this case, since the inclusions are present everywhere in the sample, it's very important to control the size and concentration of this secondary phase.

At the Brookhaven National Laboratory, an optical bench is dedicated to the study of Te inclusions. The setup is illustrated in the first chapter, a large number of samples from different ingots were tested. The aim of such a large study was to set a correlation between the growth implementations (especially on the purity of the starting elements and the gas during the growth) and the influence of the growth technique (with and without the boron oxide encapsulation). The size of the inclusions is a critical step in the fabrication of CZT radiation detectors. The bigger the Te inclusions are the heavier will be the effect on the charge collection degradation. The first set of sample studied showed a large number of big Te inclusions, as shown in 4.31 In this image the biggest Te inclusions are between 30 and 40 μm, the concentration is 6 10^6 cm^{-3} both the dimension and the concentration of the inclusions are too high to obtain a good spectroscopic response. Moreover by inclusions are present at very high concentration: between 10^3 and 10^4. The study on more recent ingots showed a decrease in the concentration of the inclusion and a better control on the crystal growth process, corresponding to a general reduction of the inclusions dimensions. In figure 4.32 are shown the Te inclusion size distri-

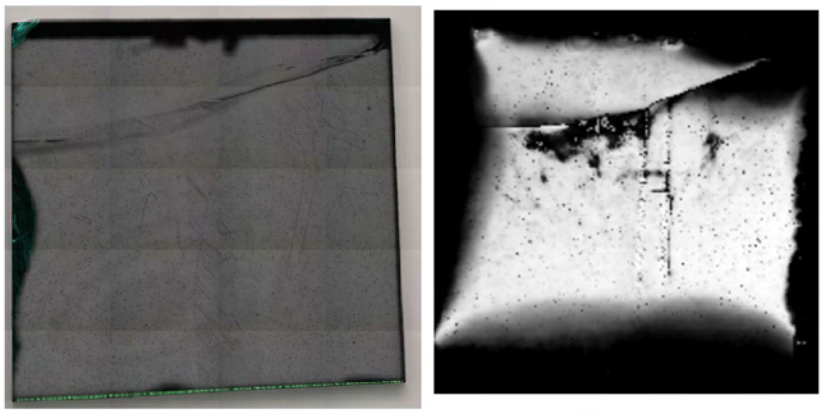

Figure 4.30: IR image and X-ray response map of a sample with extended defects, the grain boundary and the twins are clearly visible in both images

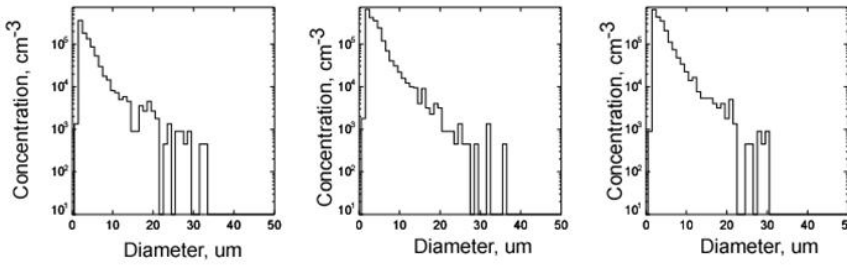

Figure 4.31: SIze distribution of Te inclusions in a CZT IMEM crystal grown by boron oxide vertical encapsulation

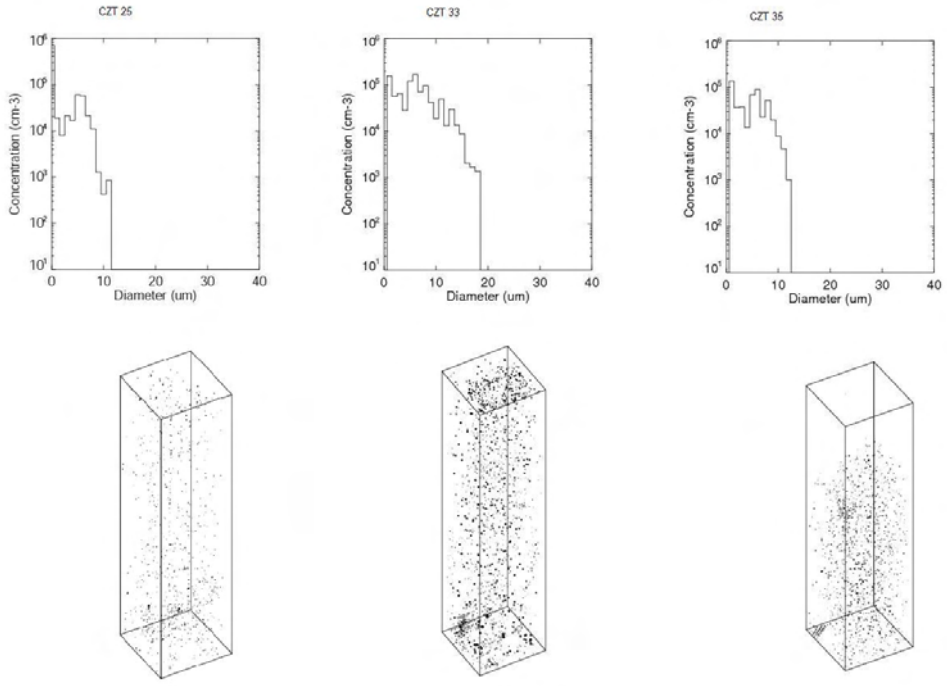

Figure 4.32: Te inclusion size distribution for three different ingots, in general the inclusion dimensions have been reduced, but the concentration is still high. The 3D reconstruction is also shown in the lower part of the image

bution and the 3D reconstruction of three samples from different ingots. With respect to the first analyzed ingots, the new samples show a better control of the inclusion dimensions, in all the tested samples the maximum dimension is lower then 20 μm, more tolerable for the correct functioning of the final device. In the case of the second sample, CZT 33, the concentration is higher with respect to the others, and by looking at the 3D reconstruction, the majority of the inclusions are in the near surface region. This means that the surface were not properly polished for this specific sample, adding more features to the inclusions counting and hence the real inclusion concentration is probably lower. However, for all the samples the total concentration of the inclusions is still high, further improvements are still needed to reduce the concentration and improve the device properties.

CHAPTER 5

Experimental results: detector characterization

5.1 Study of the CZT-metal interface

5.1.1 Current-voltage characteristic

The CZT samples are prepared as described in the "Cutting and polishing section", following a careful procedure for the preparation of an optimal surface. The removal of the damaged parts after the cutting is very important and strongly influences the detector properties. The damaged layers in fact contain a high concentration of inclusions that can results in a deformation of the electric field. The surface roughness represents as well a critical parameter in the realization of good radiation detectors [68]. The presence of residual impurities, mostly due to the polishing procedures, on the surface before the contact deposition can lead to the formation of an interlayer between the metal contact and the CZT. This layer strongly alters the characteristic of the contact. However this problem can be easily avoided by cleaning the samples with several baths in organic boiling solvents, like acetone, isopropanol and trichloroethylene. The Br-methanol etch removes all the possible residual on the surface and the native oxide, but it's well known to produce a Te rich surface that rapidly oxidize in air. The resulting oxide is more conductive with respect to the bulk CZT and hence the drawbacks of this procedure must be taken into account [65] [66] [67]. A bad polishing can also affect the contact properties, a rough surface origins a bad adhesion of the metal to the CZT surface. The polishing procedure used at IMEM produces a good surface. As confirmed by the AFM measurement the roughness is confined in the range $\leq 1nm$. The study of the

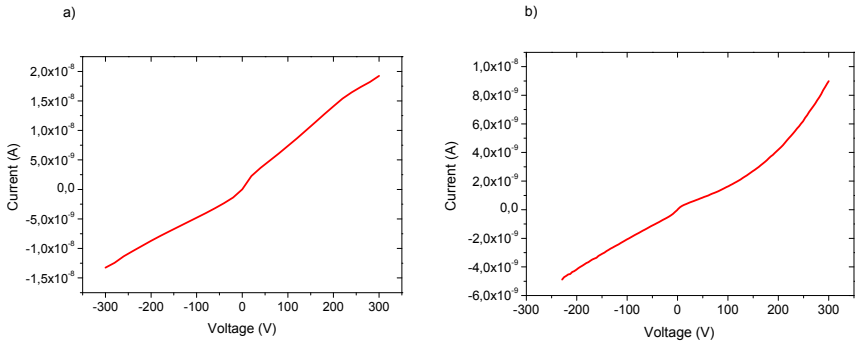

Figure 5.1: The two typical behavior found in the IMEM CZT samples. In a) the increasing resistance behavior, at low voltages the resistance value is lower and then increase for high voltages. b) The resistance decrease with the increase of the applied bias

contact properties was the aim of my master degree and represent an accurate analysis of the effect of the surface preparation and the passivation process on the IV characteristics of the Au evaporated contact [64]. The contact deposition techniques available at IMEM are the thermal evaporation and the electroless technique. The electroless deposition is a very quick way to deposit a metal on the surface of the semiconductor and produces a very good current voltage characteristic with low surface leakage currents. The used solution was a 4% $AuCl_3$ water solution, as reported in (insert citation)the optimal deposition time for the Au solution is 1 minute, after that time the reaction does not evolves and the total amount of metal is deposited. The current voltage characteristics as reported in [16] are directly connected with the spectral resolution of the devices, and in particular the behavior at high bias. The author classifies three different curves: the increasing resistance, the linear behavior and the decreasing resistance. The optimal curve for the spectral response was found to be the increasing resistance. For the IMEM samples only two kind of curves were found: the increasing and the decreasing resistance 5.1. The two behaviors corresponds to a completely different response in the presence of the X-ray sources.

A clear example of the importance of the IV characteristics on the detector performance is shown in figure 5.2. The image shows the two IV characteristics and the corresponding spectroscopic response of two sample irradiated with an ^{241}Am X-ray source.

The two samples were cut from the same wafer, of the same crystals ensuring the higher possible similarity between the crystal properties of the two samples. Also the thickness (2mm) and the dimensions (7 x 7 mm^2) are the same. The two samples differ in the IV characteristics, sample 024-04-d shows

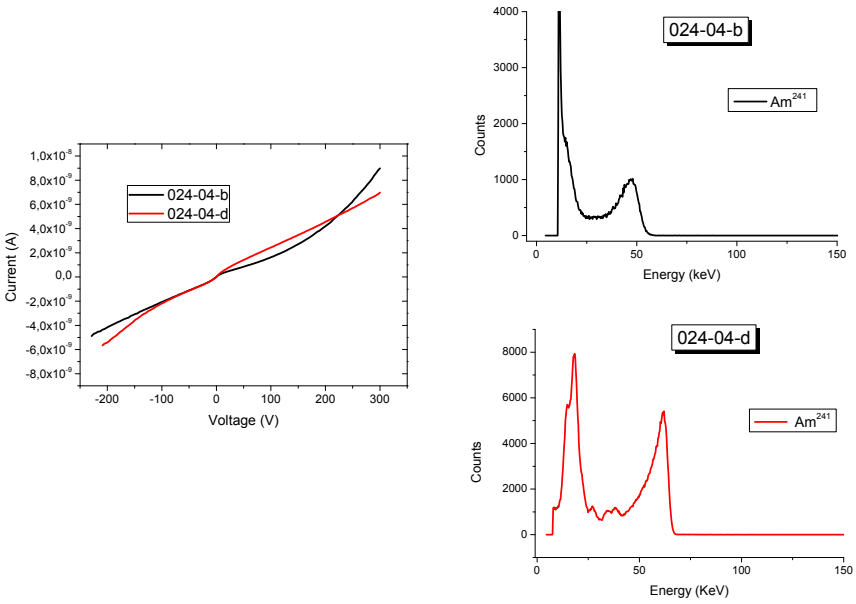

Figure 5.2: The different spectroscopic response and the corresponding IV characteristics of two CZT samples cut from the same wafer, they have the same thickness and the same surface area. The IV curve with an increasing resistivity shape shows a very good ^{241}Am spectrum, while the sample with the decreasing resistivity characteristic has a bad response. It is important to underline that the current value itself is not a significant parameter for the determining of the good functioning of the device, in fact in this case the current value is similar.

the increasing resistivity curve, sample 024-04-b the decreasing resistivity one. The same contact deposition technique was used for both the samples: electroless gold, for 1 minute on each side. The two IV curves do not differ much in terms of the current flowing in the devices, in fact for negative biases the 024-04-d sample shows higher current with respect to 024-04-b. The positive slope has instead the opposite behavior, in both cases, anyway, the current value are comparable. The main different consists in the curve shape, for 024-04-b the current voltage curve has an exponential increase at high voltages (above 150V), the 024-04-d shape is instead showing the characteristic linear characteristic in the high voltage region. The trend showed in 024-04-b to increase exponentially the currents flowing in the device is enhanced in presence of the radiation source, and hence when the charge carriers are generated, leading to a strong contribution of the noise in the device, as shown in the ^{241}Am spectrum. Since any other characteristic of the device seem to similar (the $\mu\tau$ products are almost identical, the Te inclusion density are similar and the Zn concentration is the same since the sample are cut from the same position in the growth axis) the main differences are ascribed to the IV curves. This dramatic change in the current voltage behavior may be due to the different surface condition, related to a non reproducibility of the effectiveness of the cleaning procedure or to a different field distribution. The study of the contacts by means of the RBS and XRF techniques (illustrated in the next section) highlighted a much higher damage in the case of the 024-04-b with respect to the 024-04-d: the thickness of the layers with a different stoichiometry with respect to the bulk is almost three time higher in sample 024-04-b. This measurement shows one of the main limits of the electroless technique, the poor reproducibility in the contact characteristics [70].

RBS and XRF analyses

The two deposition techniques, thermal evaporation and electroless deposition of gold, were studied using the combination of two techniques: Rutherford Backscattering (RBS) and X-ray fluorescence. The measurements were performed by Dr. A. Raulo at the University of Napoli Federico II. The recorded spectra were analyzed using the SIMNRA 4.4 software package. The study pointed out two different behaviors for the deposition techniques. The thermal evaporation affects a small region under the metal contacts, usually confined in a region up to 1500 Å, this region presents a deviation from the bulk composition mostly due to the creation of an oxidized region near the surface. For the electroless deposition technique the behavior is completely different. In this case several layers can be identified by the software modeling. As reported

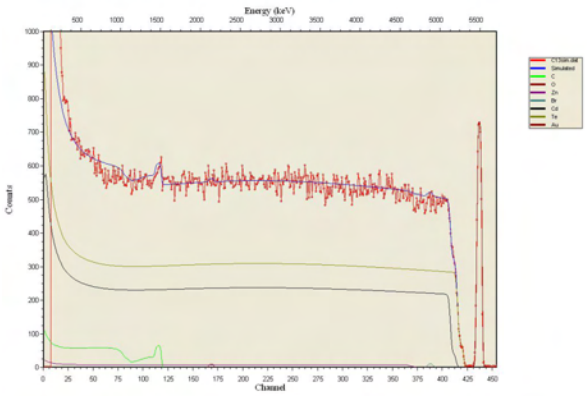

Figure 5.3: RBS spectrum of a CZT sample with thermal evaporated gold contacts

in [69] during the reaction with chloride the Cd ions leave the materials and pass in the solution, the metal ions, in this case Au, deposits on the surface creating the electrode. The electroless process leaves a layer near the surface with a decreased Cd concentration, due to the migration of the ions, and the typical Cd vacancies. The stoichiometry of the first layers is strongly deviated from the bulk one, the presence of various oxide layer was also identified in the study. The total damaged layer, that comprehends all the different layers that do not present the stoichiometry of the bulk, is much higher for the electroless contacts.

The deposited metal layer is thicker then the expected value from the literature [70], and shows a maximum value of 70 nm for the Cd terminating surface. The reaction is favorite by the excess of Cd due to the orientation of the [111] oriented surface and consequently the deposition is higher on one of the two surfaces. In [70] are also studied the Pt electroless contacts, the metal deposited layer is much thinner for the Pt chloride solution, only 10 nm, even if the deposition times were 4 minutes and 10 minutes. The I-V characteristics are dominated by the surface conductive paths generated after the deposition and the resulting currents are very high. The passivation of the surface was found to be ineffective, the current level after the passivation process is still very high. It is hence impossible to use such contact solution for the realization of radiation detector devices.

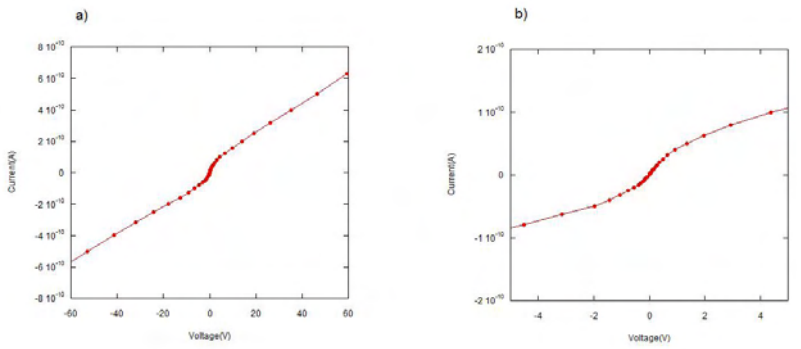

Figure 5.4: IV curve showing the two slopes for low and high applied voltages. b) low voltage region, the contribution of the bulk is highlighted by the blue line

5.2 Calculation of the resistivity from the low voltage region of the IV curve

The resistivity value of semiconductor materials is usually calculated using standard procedures like the four point probe (Van der Pauw [71]) method. In the case of semi-insulating materials this method is not efficient in the measurement of the resistivity, because the four contacts are deposited on the same surface and the measured currents are mostly surface contributions, while the bulk current is difficult to measure with this technique. The measurement of the resistivity with the Co.Re.Ma. technique is the optimal solution, because it can measure the value on a micron scale, giving the information on large area samples. However it requires the acquisition of the machine and long measurement times. The problem was overcome by calculating the resistivity from the low voltage region of the IV curve. This method was firstly proposed by [41], and it's based on the consideration that for very low biases (usually in the -1/1 voltage region) the current is dominated by the bulk contribution, while the surface become more important at higher voltage. This two behavior are visible in the IV curve, because there is an evident transition in the curve generating two different slopes.

An example of the change in the slope for the low voltage region is shown in figure 5.4. Using this technique a large number of samples were measured, the resulting resistivity is above 10^{10} Ω·cm. Some of the measured values are reported in table 5.1

Table 5.1: CZT resistivity values

Sample name	Resistivity ($\Omega\cdot$ cm)
015	$1{\cdot}10^{10}$
$016-02-\mathrm{a}$	$1.6{\cdot}10^{10}$
$016-06-\mathrm{a}$	$3{\cdot}10^{10}$
$020-\mathrm{d}$	$1.5{\cdot}10^{10}$
$020-03-\mathrm{b}$	$2.6{\cdot}10^{10}$
$020-07-\mathrm{f}$	$1.05{\cdot}10^{10}$
$021-07-\mathrm{b}$	$1.45{\cdot}10^{10}$
$024-04-\mathrm{d}$	$2.8{\cdot}10^{10}$
$025-03-\mathrm{a}$	$1.31{\cdot}10^{10}$

5.2.1 Study of the electric field uniformity by means of the Pockels Effect

The role of the electric field is primary in the functioning of the radiation detectors. The charge carriers generated by the interaction of the photon with the absorber, move toward the collecting electrode and induce the signal in the external circuit. The rate of carriers that are actually collected is strongly connected to the intensity and the electric field profile. The importance of the electric field is even higher for a device technology, as in the case of semiconductor radiation detectors, that requires the development of several millimeters thick samples. It is very difficult to obtain a uniform electric field over such long thicknesses. It is well known that CdTe radiation detectors experience a degradation of the device properties with the time, commonly called polarization effect. The electric field profile changes with time, after a bias is applied. In a period of few hours the space charge zone expands inside the device, up to a complete depletion of the field. Polarization has a dramatic effect on the operation of the devices, in order to obtain a complete recovery of the device it is in fact necessary to turn off the bias and wait for a proper time before the collection properties are restored. The substitution of CZT in the device reduces the polarization effect, since the electric field profile is more stable. A set of CZT samples was tested at IMM-CNR in Lecce, under the supervision of Dr. A. Cola, the analyzed samples are listed in table 5.2 The sample preparation requires the realization of planar contacts on the two surfaces. The lateral surfaces, corresponding to the entrance and exits surfaces of the radiation, should be carefully polished, in fact the surface quality is strictly connected to the transparency to the radiation. The optimal sample orientation is illustrated in figure 5.5, the Pockels effect in the directions shown in the figure is maximal.

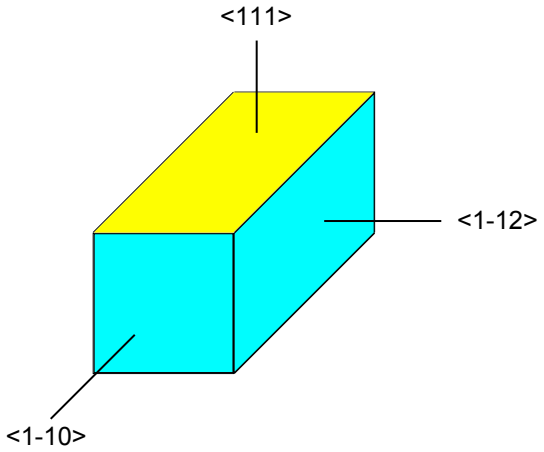

Figure 5.5: Sample orientation for the measurement of the Pockels effect

Table 5.2: CZT samples for the Pockels effect measurements

Sample name	Contacts	Contact area(mm^2)	Sample thickness(mm)
022 boronox · enc ·	Au-Au electr.		7.1
022 boronox · enc ·	Au-In electr.		7.1
016 −04 − fboronox · enc ·	Au-Au electr.	10.3 x 9.8	1.1
024 −07 − fnoboronox · enc ·	Au-Au electr.	6.7 x 6.5	1.93
025 −03 − inoboronox · enc ·	Au-Au electr.	5.3 x 4.5	1.91

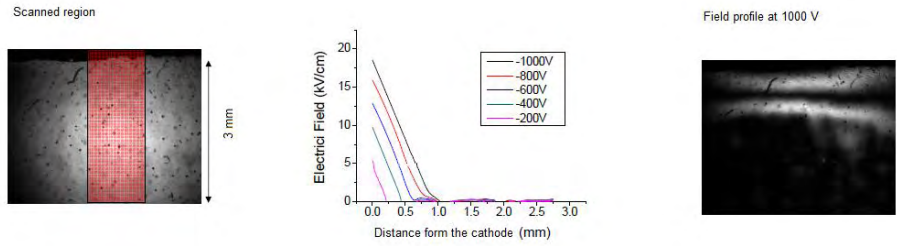

Figure 5.6: Electric field profile in sample 022 with the Au-Au contact configuration

The samples have all similar thicknesses and shapes except for the first one, sample 022, that is much thicker and bigger then the usual ones. The aim of the study of this sample was to see the behavior of the electric field on a sample with bigger dimensions then the usual ones. For the first sample the behavior of the electric field is completely different with respect to the following ones. The electric field decreases almost linearly from the cathode, presenting the same slope for all the applied biases. Considering the thickness of the sample, 7.1 mm, the electric field value is moderate also at a voltage of 1000 V. The electric field profile was studied over a 3 mm thick region in the top part of the sample and near the center of the device.

The extension of the electric field over the sample is very limited, for a 1000 V bias the field decays after less then 1 mm, as shown in figure 5.6. The measurement were performed without external lights. The field profile does not change by inverting the polarization, the electric field is still confined under the cathode. The fringes present in the image are indicating that the electric field is decreasing from the cathode side to the anode. The residual birefringence of the sample (the birefringence in absence of the electric field, 0 V) is quite high, this is usually associated with internal unreleased stresses). The electric field profile is completely different for the other samples, in the case of thinner detectors it is easier to control the uniformity of the electric field. After the first set of measurement one of the contacts was removed and a new In electrode deposited, creating a Shottky like diode. The presence of the In electrode, however does not affect too much the field distribution 5.7. The most notable difference is a slight increase in the region where the electric field is present. Despite the presence of two different metals on the two sides the profile appears symmetrical, this can be ascribed to the very high thickness of the sample. As shown in 5.2 the contact deposition technique was the same for all the samples, in order to concentrate more on the properties of the material itself, instead to provide a characterization of the deposition

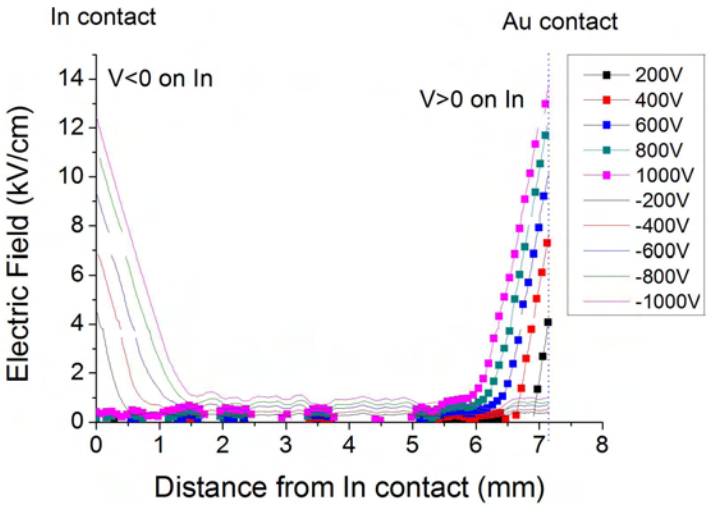

Figure 5.7: Electric field profile in sample 022 with the In-Au contact configuration

techniques. The sample were selected from different ingots, comprehending the two different growth techniques, with and without boron oxide encapsulation. The measurement on sample 022 was performed without any filter, and hence the sample received the entire amount of light. This has probably influenced the measurement degrading the profile because of the too intense radiation. For the second set of samples the Pockels effect was measured using several filters (from 800 to 1500 nm). For this second experiment, in conditions of low flux, the uniformity of the electric field is highly improved. A strong correlation was found between the electric field distribution and the intensity of the incident radiation 5.8, this is probably due to the high number of carriers generated in condition of high flux.

The field profile was very uniform for all the samples, in particular for the 016-04-f, but this is probably due to the reduced thickness of this particular specimen, rather then to the different growth technique, in fact this sample is almost half of the others.

In figure 5.9 the electric filed is almost flat, except for a small decrease in the anode direction. Among CZT detectors this can be considered a very successful result, considering the difficulties in the obtaining of a uniform electric field in CZT devices. For this specific measurement a ODG=2 filter was used. A very similar profile was found for the sample 024-07-f, the profile shows a more pronounced decrease, but the uniformity is anyway very good.

For the last sample, 025-03-i the quality of the lateral surfaces does not allow a deep analysis of the sample as a function of the applied bias, but it possible only a study at high voltage (1000 V), because the Pockels signal is too

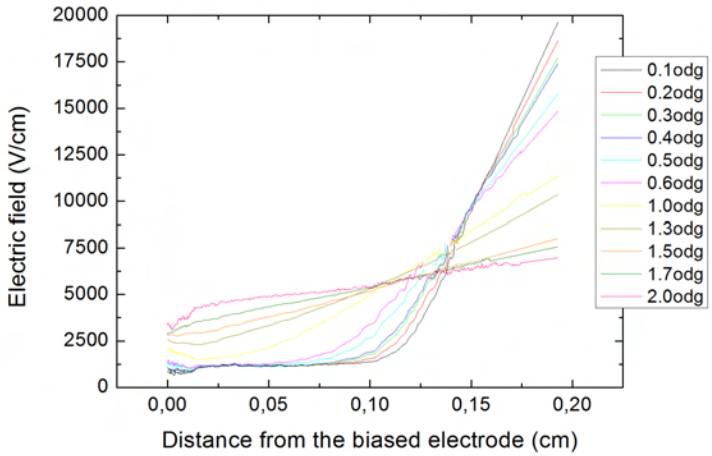

Figure 5.8: Electric field distribution as a function of the optical filter. *odg* stay for Order of magnitude

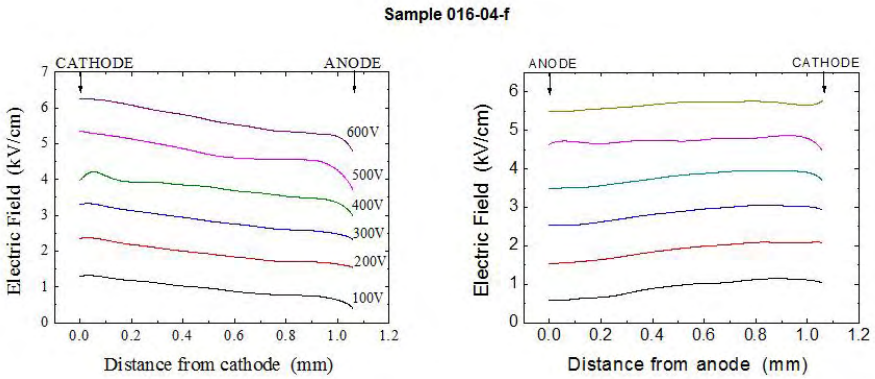

Figure 5.9: Electric field distribution of sample 016-04-f

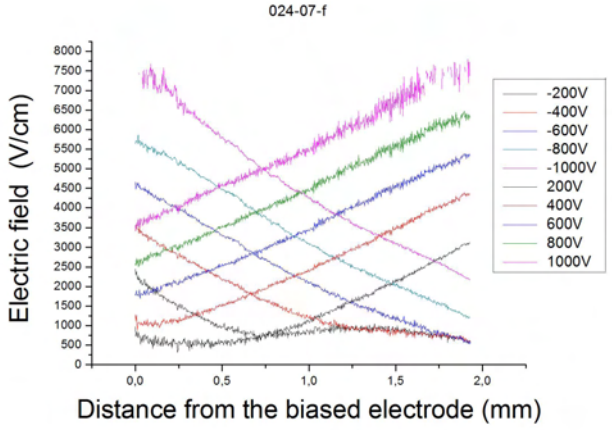

Figure 5.10: Electric field distribution of sample 024-07-f

low. The dependence of the electric filed from the radiation intensity is similar to the one observed for all the other samples. The study of the electric field uniformity in IMEM samples revealed a very good uniformity in low intensity condition for all the samples, the increase in the radiation intensity corresponds to a reduction of the field under the cathode. Since the radiation is below the energy gap of the material the effect of the intensity on the electric field can be related to the ionization of a deep level, probably the one responsible of the high resistivity of the material. The best result is obtained for thin detectors (1-2 mm).

5.3 CZT Spectroscopy

The detector performance is usually qualified by the photopeak resolution and the peak to valley ratio of the photopeak. During the PhD research period a large number of ingots were grown at IMEM, several samples from every ingot were studied in order to obtain a full characterization of the crystal. The spectroscopic characterization of the material has been an intense work, consisting of the testing of over 100 CZT prototypes. For CZT detectors, the resistivity is higher with respect to CdTe and hence the standard bias applied to the device is higher with respect to the one used for CdTe detectors. It is commonly to accept 100 V/mm as the minimum bias to have an electric field sufficient to drift the charge carriers. While testing the IMEM devices several parameters were studied in order to obtain the best resolution in the acquired spectrum. The optimal shaping time of the amplifier and voltage were deeply analyzed for several of the studied samples. In general the behavior of the IMEM sample was found to be very reproducible. A strong homogeneity of the characteristics was found between the ingots and in particular between the samples cut from the same ingot. The characteristics of the device were similar, but the general quality of the detectors was monotonically increased during the period of the PhD research. The acquisition method was setup in order to have the best reproducibility in the measurement. The spectra were all acquired without the collimation of the sources and by keeping constant the distance between the source and the measuring box. The spectra were acquired one hour after the biasing, so the sample internal electronic configuration is stable after a relatively long stay in the dark and under polarization condition. The first test discriminates between the samples with good enough qualities: if the photopeak is resolved at 100 V per mm, further investigations are done, to find the optimal configuration. The samples are biased at different voltages and with different sources, the optimal bias is chosen by looking at the FWHF

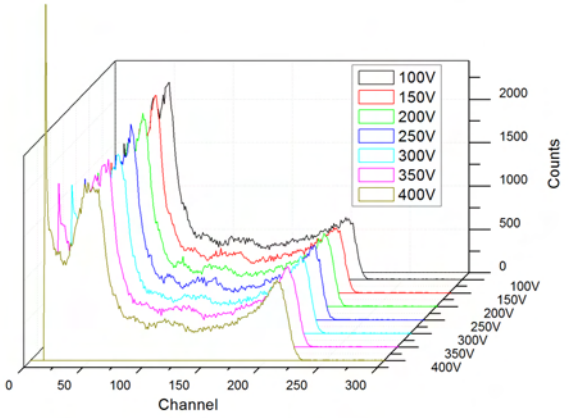

Figure 5.11: Sample 016-02-a, X-ray response with the ^{241}Am source at different biases

of the characteristics photopeak of every X-ray source.

In figure 5.11 is shown the study of the detector response as a function of the applied bias on a CZT sample grown at IMEM, sample name is 016-02-a. The Au electrodes are deposited using the electroless technique on the entire surface of the sample (5 by 5 mm), the sample thickness is 1.1 mm. The first set of measurements shown was acquired in PPF configuration, with the X-ray source irradiating the electrode surface. The starting applied bias is the standard 100 V, this value was increased up to 450 V. The results obtained for this samples can be extended to represent the behavior of all the IMEM grown material, since all the ingots seems to have similar results. The first comment on this measurement is that IMEM grown CZT can tolerate very high bias, it was measured up to 600 V per mm. The noise level is hence very limited also for high biases, this is due to the very high resistivity values for IMEM CZT samples, as measured from the IV curve.

While the low energy part of the spectrum is not very affected by the increase of the bias, also fro the 400 V spectrum the peak to valley ratio of the 13-17 KeV part is good. The energy resolution however is a little degraded, since at high voltages the two peaks appear convolved in one single emission. The spectra evolution in 5.11, shows an enhancement of the charge collection efficiency with increasing the bias voltage, represented by the shift of the photopeak to higher channels. The fit of the photopeak comprehends two contributions. The main peak is fitted by a gaussian curve that cover the majority of the events; the trapping part, consistent of an asymmetric tail on the low energy part of the peak, is fitted by a GMG (modified gaussian), this contribution has to be considerably smaller with respect to the main part fitted

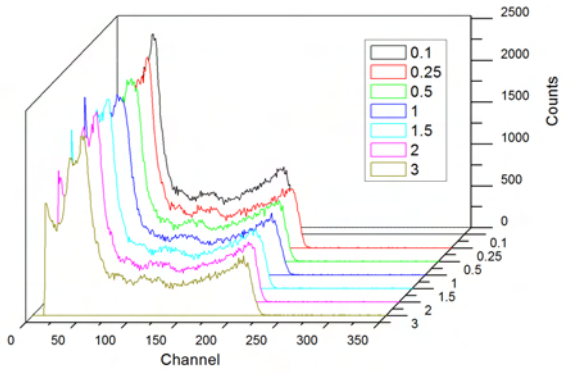

Figure 5.12: Sample 016-02-a, X-ray response with the ^{241}Am source while selecting different shaping times in the amplifier. the value of the shaping time is expressed in μs

with the gaussian. This second contribution is not influent when calculating the FWHM of the peak (that is in fact obtained only from the gaussian curve), but is fundamental when the total events of the photopeak need to be counted.

The evaluation of the optimal shaping time of the main amplifier was performed at different energies using several X-ray sources. in figure 5.12 is shown the study for the ^{241}Am source, all the measurement were performed at the standard bias of 100 V. The measurement was done in PPF and PTF configuration, the results for the second configuration is shown in figure 5.13.

In figure 5.14 and 5.15 are reported the behavior of the energy resolution and charge collection efficiency (CCE) respectively, of the measurement shown in figure 5.12 and 5.13. The CCE is normalized to the photopeak centroid of the fully deposited energy for the 60 KeV in the two configurations. The best energy resolution, calculated on all energies scanned with the available X-ray sources, was obtained with 2 μs, the corresponding CCE is 97%. A direct comparison of figures 5.12 and 5.13 shows a strong improvement of the spectroscopic response in the PTF configuration measurements. This fact is quite surprising because, in the PTF configuration all the distances between the electrodes are uniformly illuminated at the same time. Tailing effect is strongly reduced in the spectra shown in 5.13. This can be due to a different perturbation of the internal electric field in the two configurations. The sensitivity of IMEM grown CZT sample to the intensity of the incoming light was already shown in a previous section. Due to the small fraction of the ionized centers, a small fraction of photo generated carriers can in fact strongly modify the net charge. The poor

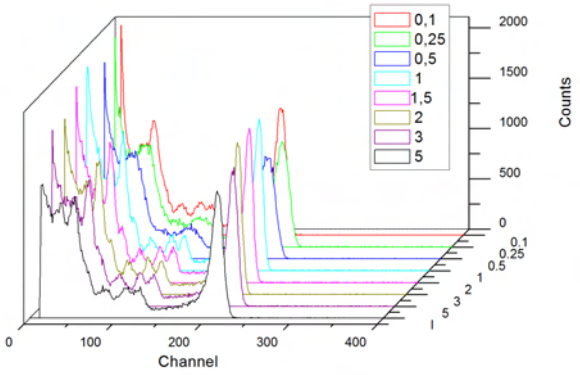

Figure 5.13: X-ray response to the ^{241}Am source of sample 016-02-a at different shaping times, the spectra were acquired in PTF configuration

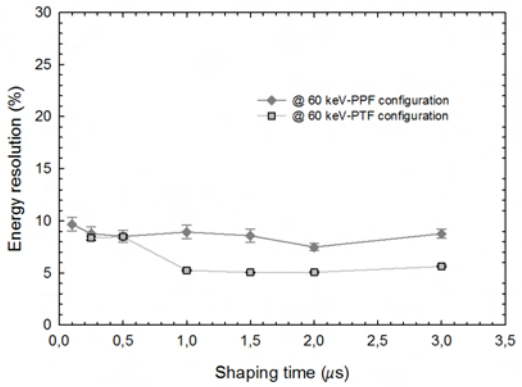

Figure 5.14: Energy resolution vs. shaping time

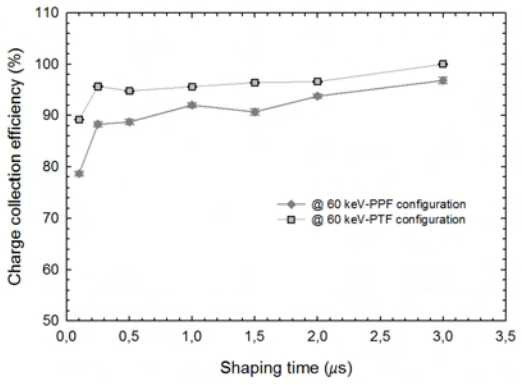

Figure 5.15: Charge collection efficiency vs. shaping time

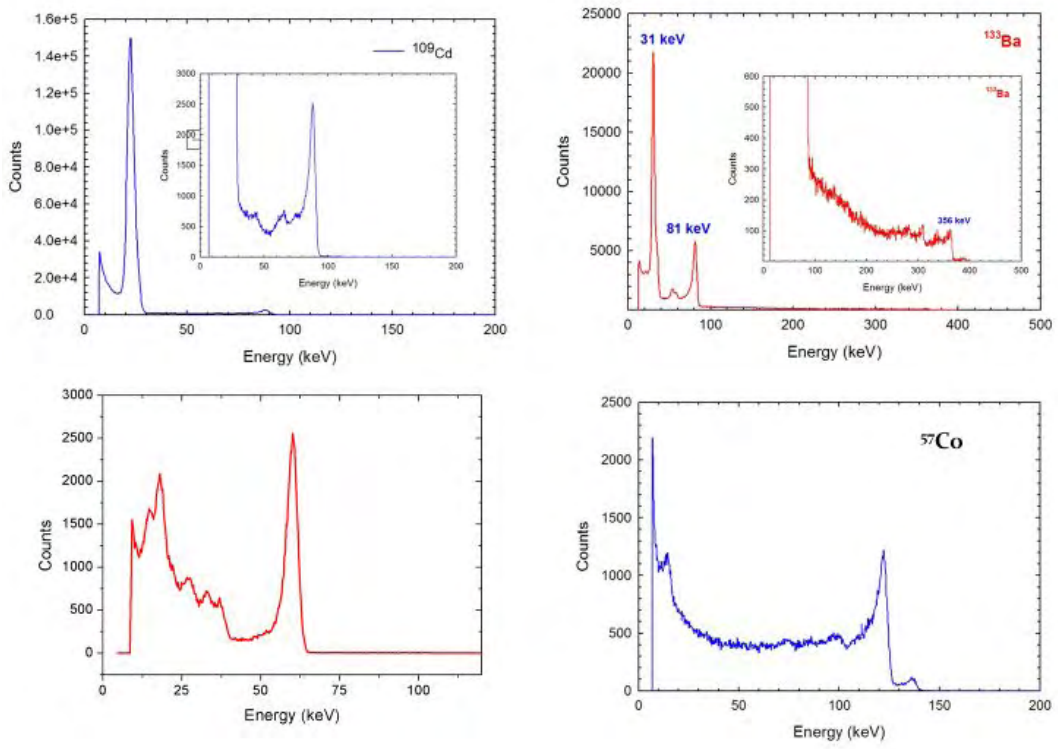

Figure 5.16: Spectroscopic results of the IMEM CZT samples obtained for a recently grown ingot

hole trapping can create an accumulation of positive charge at the cathode and induce a local perturbation of the electric field.

During the PhD period, the efforts done in the optimization of the crystal growth and the device technology have lead to a great improvement in the detector quality. The starting elements purity was increased, they are all 7N materials, and also the growing environment was purified by using 7N grade inert gas. This improvement in the growth was matched with the realization of more stable electrodes and a particular attention in the surface quality and preparation. The amelioration consists in a strong reduction of the energy resolution with the standard X-ray sources commonly used, the most recent results (figure 5.16 are: 6% for the 60 KeV of the ^{241}Am, 3.2% for the 122 KeVof the ^{57}Co, 4.9% for the 88 KeV of the ^{109}Cd source. The improvement was not only consisting in a better energy resolution, but also the range of energy that can be detected was enlarged. Recent measurements have shown the detectability of energies up to 356 KeV (Ba source) and with a specific electrode configuration (the coplanar grid) also the 660 KeV emission of the ^{137}Cs was revealed. The reproducibility of the results is also much higher in the recent ingots. The

exploration of energies higher then 100 KeV, was challenging for the first grown ingots, but the improvement in the transport properties made it possible to detect also high energies. In the first examined ingots for medium high energies, in the range between 60 and 120 KeV, it was possible to detect the peak only by strongly increasing the applied bias up to 400-600 V/mm. At the more regular voltage of 100 V/mm only the peaks at lower energies (typically the 13-17 KeV region for the Am source and the 22 KeV for the Cd) were clearly resolved. In figure 5.17 is shown the response at 100V of a CZT device studied at the beginning of the PhD. The detector thickness is 1mm, so the applied bias can be intended also as V/mm. The peaks at 13.9 KeV and 17.7 KeV can be seen as well as the convolution of the two escape peaks, the 60 KeV emission is however very weak for this voltage. This behavior is very common in the first ingots analyzed. The increase of the counts on the higher energy peaks is as well common, as it's shown in figure 5.18 the 60 KeV emission is now visible, with a fair energy resolution (FWHM: 6.8%). In figure 5.19 is shown the device response at 400 V/mm for the three standard sources commonly used: at this very high bias also the 122 KeV emission of the ^{57}Co source emerges. The shape of the high energy peaks (figure 5.18 and 5.19) suggest that the poor resolution at relatively low voltages is mostly due to the trapping effect. This hypothesis is supported by the general amelioration of the spectral resolution observed for the first studied samples when the measurement was carried out in PTF geometry. As shown in figure 5.20 the 60 KeV appears very narrow with respect to the one acquired in the same conditions but in the PPF configuration (figure 5.19), moreover the ratio between the low energy part of the spectrum and the 60 KeV is in agreement with the value expected from the emission intensity of the source. The energy resolution of the 60 KeV peak is in this case 4.9%. The effect of trapping is in this case lesser, as it's possible to notice from the strong reduction of the typical tail on the low energy side of the peak. In the PTF configuration in fact the photon are impinging the device on the side and hence the events are generated undergo the exponential decay at every depth inside the sample. In the PPF configuration the events are entering from the irradiated sourface and are exponentially absorbed at a fixed depht. In the case of the PTF geomerty the high energy part is, for some photons, generated near the electrodes and fully collected with a minimum influence of the trapping, with the PPF geometry this is not possible since the high enegy events are however generated deeply inside the device.

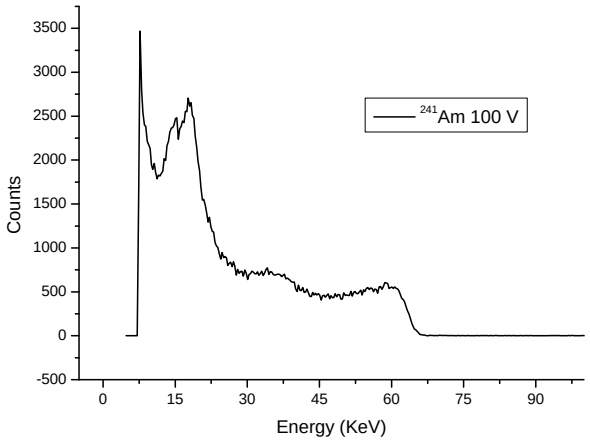

Figure 5.17: Spectroscopic response at 100 V with the ^{241}Am source. The peak at 60 KeV is barely resolved.

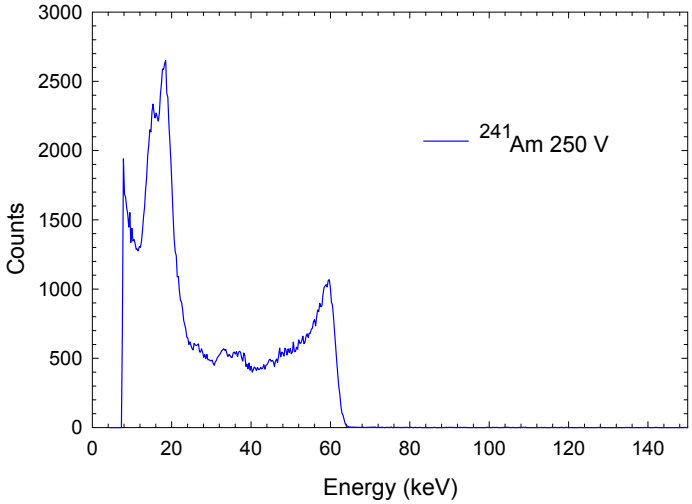

Figure 5.18: Spectroscopic response at 250 V with the ^{241}Am source. The peak to valley ratio of the 60 KeV peak is much higher (FWHM: 6.8%).

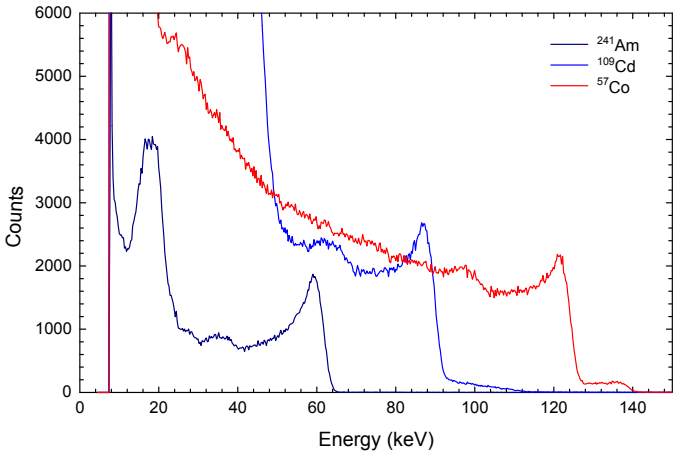

Figure 5.19: Spectroscopic response at 400 V with the Am, Cd and Co sources. Despite a reduction of the energy resolution in the low energy part of the spectrum, the photopeaks up to 122 KeV can be detected.

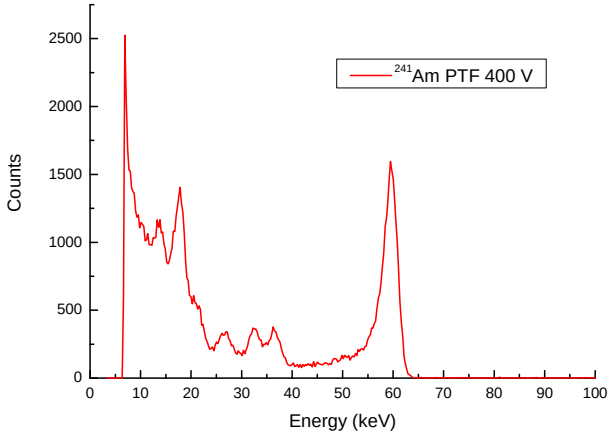

Figure 5.20: Spectroscopic response at 400 V with the ^{241}Am source acquired in PTF geometry. The peak to valley ration is strongly increased in this configuration. The ratio between the low energy peaks and the 60 KeV peak is as well improved, as expected from the expected intensity of the emissions.

5.4 X-ray response mapping

The presence of defects influences the detector spectroscopic quality by degrading the response, typically a broadening of the photopeak FWHF is observed or the presence of a tail in the low energy side of the peak. With an uncollimated source it's possible to observe the overall response of the device and the degradation appear as a convolution of all the defect contributions. Whit the X-ray response mapping system, the effect on the peak formation of every defect is observed, because a single photopeak is recorded for every position of the raster scan. The X-ray response map reproduces an image of the entire sample, for every point in the map is reported the peak position, and hence the charge collection efficiency. The contrast of the resulting image reconstructs the defect patterns in the sample. The X-ray response map of a set of IMEM samples was studied at the National Synchrotron Light Source (NSLS) inside the Brookhaven National Laboratory. The NSLS facility contains a beamline (X27B) entirely dedicated to the study of the response map for x-ray detectors. The beam is a x-ray synchrotron emission tunable between a few KeV up to 30 KeV. For the measurement on IMEM sample the energy of the beam was 24 and 25 KeV. For a high resolution image it's recommended a raster scan of 20-25 μm, with this resolution is possible to see the small features present in the sample. The sample were all analyzed by setting the amplifier at 200 and 2 μs, the acquisition time is 0.5 seconds for every point.The collected data are elaborated by a dedicated IDL routine, the output is a 2D image of the response map, a 3D image and the reverse 3D image. By clicking on a specific point on the map the program provide the corresponding peak. It is also possible to select a restricted area on the plot and then work on that defined area. This may be extremely useful in the study of a specific defect. The IMEM sample tested at the beamline were all spectroscopic grade and the majority showed a very uniform response. In figure are shown the X-ray response maps of some of the tested sample, the image contrast is very uniform corresponding to a high uniformity in the device charge collection properties.

The response homogeneity obtained from the map in figure shows a small fluctuation in the detector response. The histogram in figure is obtained from the map data and does not take into account the effect of the electronics on the broadening of the peak. The value of the uniformity shows a fluctuation about 2%. A very good point of the IMEM grown material is the reproducibility of the good spectroscopic response in a large number of the tested samples. A heavy degradation of the device property is always associated with the presence of an extended defect. Some samples were intentionally prepared including a grain boundary inside the device active area, in order to have a quantification

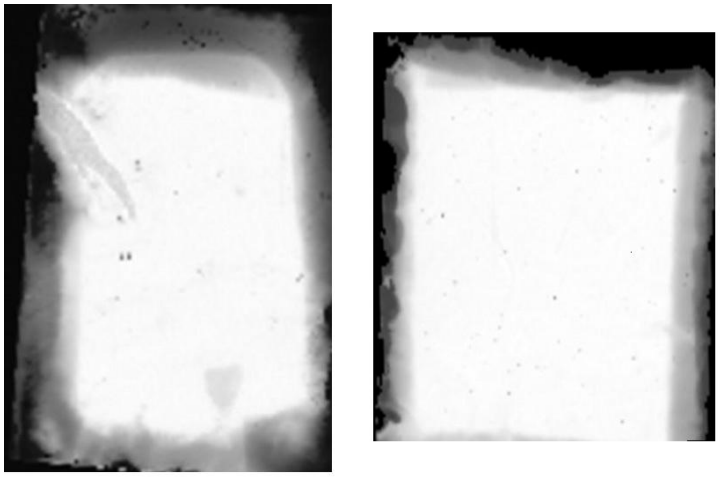

Figure 5.21: 2D X-ray response maps of 2 IMEM samples

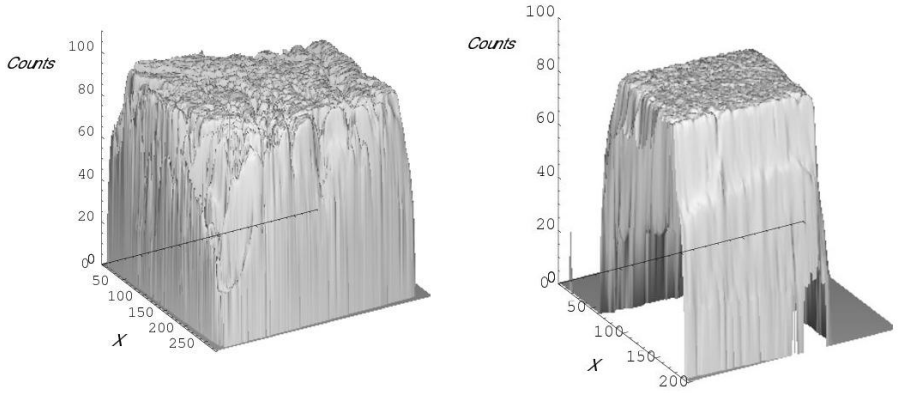

Figure 5.22: 3D X-ray response maps of 2 IMEM samples, the 3D image underline the uniformity of the response

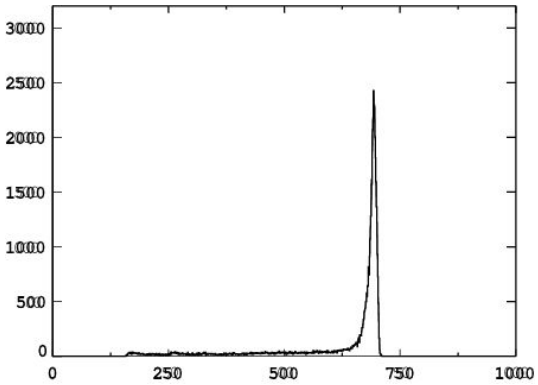

Figure 5.23: Histogram obtained from the X-ray response map. In the y-axis is reported the number of pixels, in the x-axis the position of the peak (in channels)

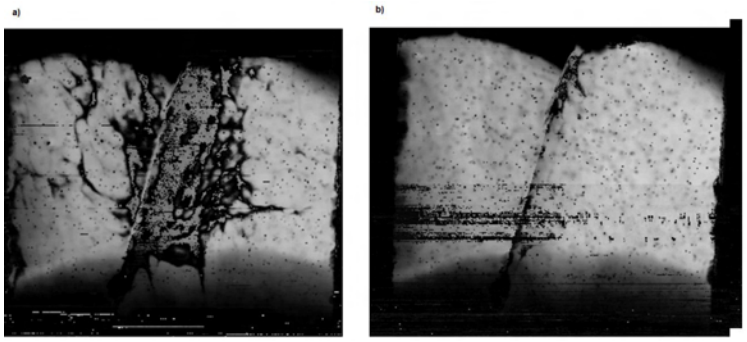

Figure 5.24: Effect of the flux on the detector response in the presence of an extended defect: a) using a 20 μm collimator and b) reducing the beam area (collimator 10 μm) and hence the impinging flux

of the degradation effect of an extended defect on the properties of a relatively small device.

The degradation effect of the grain boundary in the detector device is related to the flux of photons impinging the surface. The number of events generated inside a radiation detector device influences the electric field profile, hence in condition of high flux the degradation is enhanced, the effect is particularly high in the case of a synchrotron source because of the high flux ($> 10^7$ photon/s). The studied sample presented a big grain boundary crossing the entire sample, the electric field is distorted in the near edge region of the sample, resulting in a bending of the X-ray image.

The flux was varied by changing the collimator size, the 10 x 10 μm collimator is the smallest available at the beamline and strongly decrease the flux of photon impinging the surface. While measuring in condition of high flux the size of the used collimator was double: 20 x 20 μm. The effect of degradation

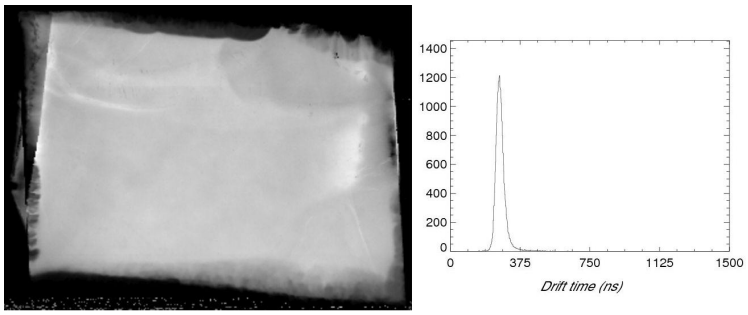

Figure 5.25: A very uniform X-ray response map corresponds to a narrow distribution in the drift times for electrons

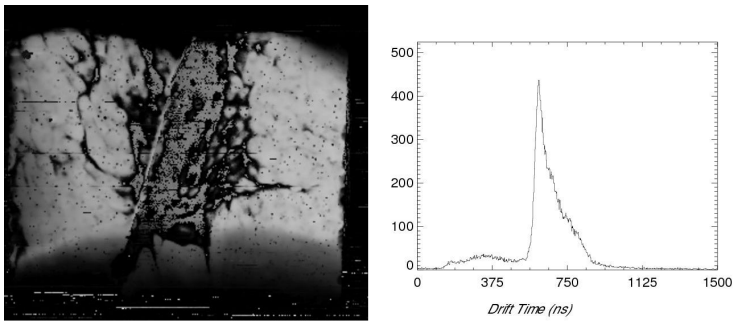

Figure 5.26: The presence of a grain boundary in the sample strongly affect the charge carriers drift time, the peak is broad and shift to higher values of drift times

due to the high flux is not present in samples that do not contain extended defects, the detector response is the same with the two different collimator. The response in the case of a sample containing extended defects vary strongly by changing the collimator. An example of this effect is shown in figure 5.24. The a) image acquired in high flux condition presents a large degraded region expanding from the defect, in b) instead the damage is confined along the grain boundary, the horizontal lines present in b) are ascribed to a fluctuation in the beam intensity during the measurement. The behavior of defects as electron traps was frequently proposed as an explanation of the effective mechanism of degradation in the presence of grain boundaries or similar features as well as Te inclusions. For this reason the drift time of electrons was calculated and then the obtained value related to the presence of extended defects. For the acquisition of the drift times a LeCroy Waverunner was employed to digitize and record the output signals(waveforms)from the charge sensitive preamplifier (a commercial eV-Product preamplifier, eV-5093). A number of 200 waveforms were acquired for every measurement.

The values obtained for the drift times in different samples seems to have a direct correlation with the presence of extended defects (and the corresponding degradation of the response) and the broadening in the distribution of drift times, together with an increase of the mean value. In samples that do not present such defects the drift time appears as a gaussian distribution around the average value, with a small spread of drift times.

5.5 Transport properties: $\mu\tau$ product

The $\mu\tau$ product represent a good indicator of the transport properties of the device, being related to the diffusion length of the carriers. The $\mu\tau$ product is usually calculated from the fitting of the curve obtained by changing the applied voltage and measuring the corresponding shift in the peak position (in channel number). The measurement can be performed with different radiation sources: alpha particle, an X-ray source with a low energy emission, a laser or by means of photocurrent measurement. The peak position is identified by a gaussian fit of the photopeak. In this work both the alpha particle and the X-ray source techniques were used. The resulting curve is fitted with the Hecht equation, considering only the electron part of the equation, since electrons are the only carriers drifting trough the device and contributing to the photopeak formation in the used configuration . In fact the irradiated electrode is the cathode, and with both sources the events are occurring very near to the entering surface. The measurement require the same electronic equipment as the measurement of the spectroscopic response with a standard X-ray source: a charge sensitive preamplifier and an amplifier, together with a HV supplier. The peak position is identified by a gaussian fit of the photopeak. Because of the importance of the measurement of the $\mu\tau$ value in judging the material and device properties the measurement was performed independently, in different laboratories, on the same set of samples. The measurement with the alpha particle source was performed in Naples by Dr. A.Raulo and in by me at the Brookhaven National Laboratory. The measurements with the X-ray source at INAF-IASF and at the Brookhaven National Laboratory, in the first case the 22 KeV emission of the $^{1}09$Cd source was used and in the second the 60 KeV emission of the $^{2}41$Am. A strong increase in the $\mu\tau$ product value was registered in recent ingots, with respect to the first measurement, and the increase in the charge transport properties was also confirmed by the better energy resolution and quality of the X-ray spectra.

In figure 5.27 and 5.28 are shown some of the resulting fitting. The obtained values for electrons is between 1 and 6 $10^{-}3$ cm^2/V for both kind of sources.

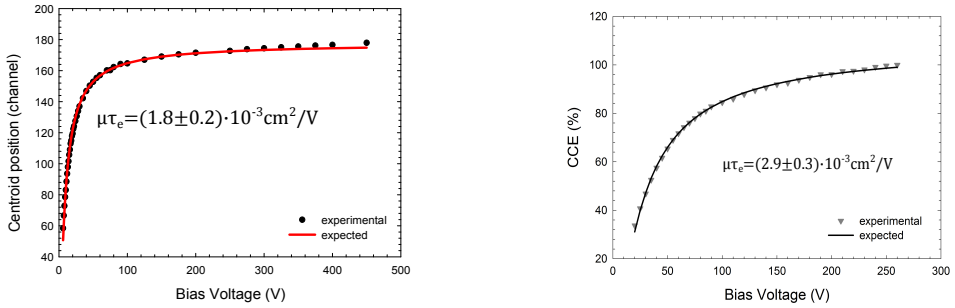

Figure 5.27: $\mu\tau$ product of two samples obtained by fitting the centroid position of the 22 KeV emission of ^{109}Cd source with the electronic part of the Hecht equation

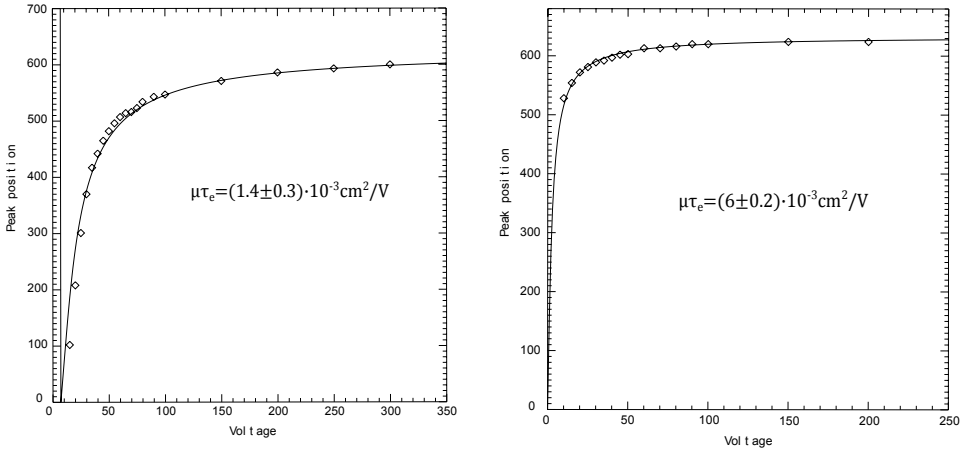

Figure 5.28: $\mu\tau$ product of two samples obtained by fitting alpha emission with the electronic part of the Hecht equation

The measurement of the $\mu\tau$ product for holes was not possible, because in the hole measurement configuration, the anode irradiated with the source and the holes collected on the opposite electrode, no photopeak was present in the spectrum. This means that the value of the $\mu\tau$ for holes is very small. A confirmation of this is given by the measurements performed at ESRF, in Grenoble, at the high energy beamline A15. The samples were irradiated at different energies in PTF configuration (planar transverse field), at different depth on the sample side, the beam size was 10 x 10 μm. In this configuration, since the events are generated at different depths, both the charge carriers are contributing to the peak formation. In this case the complete Hecht equation is used to fit the experimental data and the $\mu\tau$ product value is obtained for electrons and holes. The obtained value for holes is 5 $10^{-}5$, perfectly compatible with the previously observed absence of a photopeak in the hole measurement configuration.

5.6 Correlation between the IR image and the X-ray response map

A very interesting result that can be obtained from performing a complete characterization of a sample, is the possibility to make a correlation between the used techniques. In this way, it's possible to understand the role of defects on the functioning of the device. The IR image itself in fact is not able to give any information about the role of the identified inclusions in the operation of the sample as detector. In the same way the X-ray response map is not sufficient to uniquely identify the defects present in the device. Despite the large amount of samples analyzed with the technique, here I am going to present a detailed study on one single sample, since the result we have reached for this sample can be intended as a general result for IMEM grown CZT sample. All the images presented in this section are belonging to sample 024-04-d, this sample was deeply studied in INAF-IASF, the optimal bias was obtained from the photopeak FWHM at different polarizations, the optimal shaping time was found to be 2 μs, the spectroscopic response was studied with several X-ray sources. This sample was then studied during my stage at the Brookhaven Nation Laboratory, where I performed the measurements shown in this section. First, it was measured the X-ray response map, the beam energy is 25 KeV and the raster scan resolution 20 x 20 μm. The sample was biased with 100V per mm (total 200V), shaping time 2 μs and gain 200. The two maps are shown in figure 5.29, the two maps are quite different, because of the relatively small penetration depth of the 25 KeV photons. The homogeneity is very good for

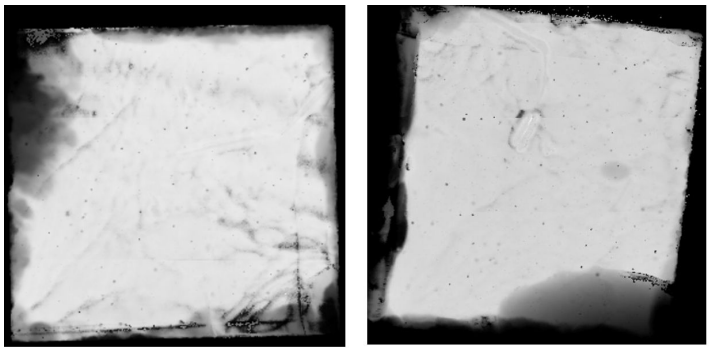

Figure 5.29: X-ray response maps of sample 024-04-d: side 1 and 2. The difference between the two maps is ascribed to a relatively penetration depth of the photon at 25 KeV

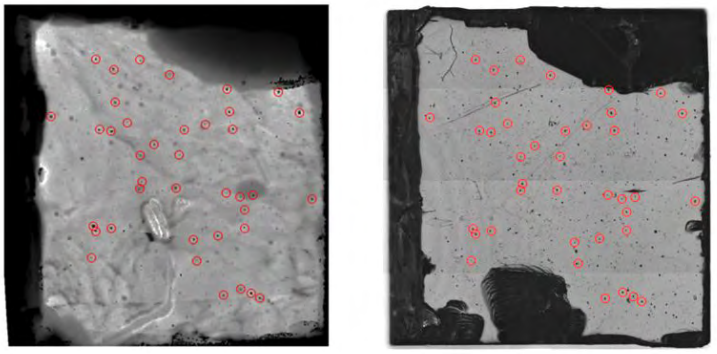

Figure 5.30: Correlation between the X-ray response map and the IR collapsed image. Several Te inclusions present in both images were randomly selected in the sample.

both maps, the big dark part present in the second map is simply a missing corner in the device and not a defect.

The first step of the study was to correlate the X-ray response map with the transmitted IR image. The electrode were removed by using a very soft alumina paste polishing, in order to minimize the removed area and limit the lost of information. The IR image of the polished sample was acquired at BNL using the Nikon Microscope, the collapsed image was created from a set of 10 images acquired at different depth inside the sample. The largest Te inclusions present were found to be about 30 μm in diameter. The collapsed image was then directly compared with the X-ray response map, the two images are shown in figure 5.30. The X-ray response map contrast was enhanced in order to have a more defined picture of the features present that now appear more clear in the map.

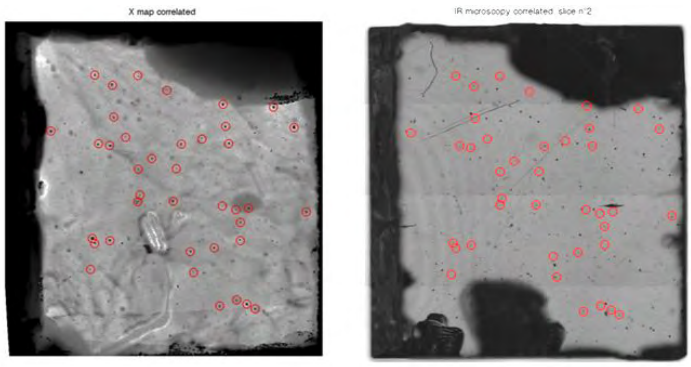

Figure 5.31: Correlation between the X-ray response map and a bottom IR image. Only a small number of Te inclusions identified in the X-ray map belong to this region of the sample

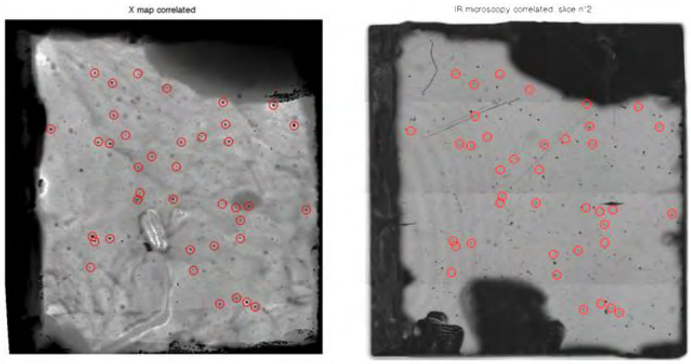

Figure 5.32: Correlation between the X-ray response map and the IR collapsed image. Several Te inclusions present in both images were randomly selected in the sample.

The new contrast underline the presence of several dot like features, from the comparison with the IR map is possible to identify the dots as Te inclusions. This comparison confirm that Te inclusions have an active role in the degradation of the detector response. In figure 5.30 some of the features present in both images were selected with red circles, the features were chosen randomly covering the entire device surface and with different dimensions. By splitting the collapsed image in its original components, it's possible to reconstruct the position inside the sample of the selected inclusions and correlate it with the influence on the collection efficiency. The X-ray response map is then correlated with an IR image collected in the bottom region, corresponding to the near anode area in the X-ray map, and a IR top image, that is cathode region in the X-ray map.

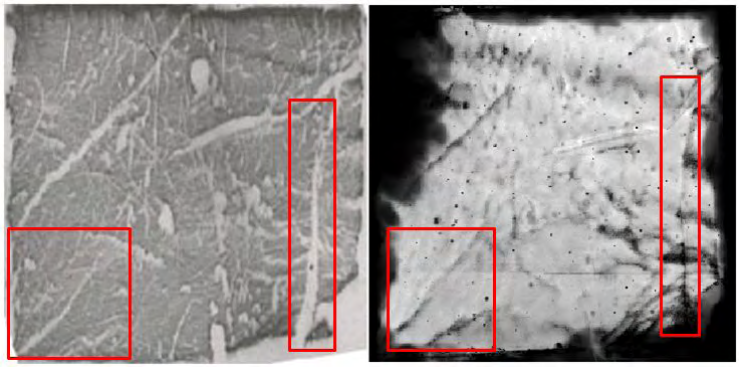

Figure 5.33: Correlation between the X-ray response map and the WXDT image. Several features are present in both maps.

The comparison with the bottom and top IR image shows a strong dependence between the position of the inclusions and the role in the X-ray response map. In figure 5.31 the comparison shows that only a small number of the identified inclusions belong to this part of the sample. The inclusions that have an influence on the collected X-ray map are only the big ones (diameter 30 μm). The top image instead comprehends the majority of the events. The X-ray response map in fact is acquired by irradiating the cathode, corresponding to the top part of the IR image. This means that the photons are absorbed in the layer corresponding to the first 200-300 μm considering the impinging energy of 25 KeV. The Te inclusions present in the IR top image are in the region where the photons creates the electron-hole pairs. The effect of trapping is hence extremely marked for those inclusions. In this region, figure 5.32, also small inclusions can be identified in the X-ray response map. The size of inclusions that can be seen in the map is limited by the raster scan resolution of the X-ray map.

5.7 Correlation between the WXDT and the X-ray response map

The presence of extended defects identified in the X-ray response map can be correlated with the images acquired using the WXDT. The grain boundaries and twins inside the detector affect the collection properties of the device, the defects act as traps and performs a severe degradation in the formation of the peak. The correlation between the two techniques is shown in figure 5.33.

The X-ray response map is acquired as explained in the previous section and is corresponding to the side 2 of sample 024-04-d in figure 5.29. The WXDT

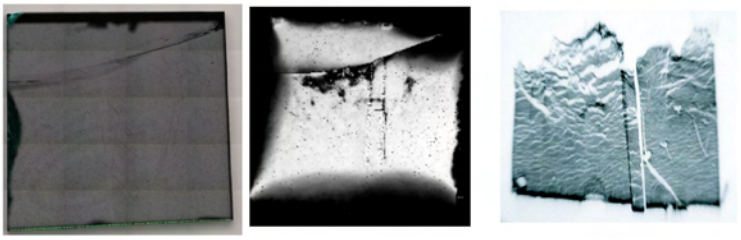

Figure 5.34: Correlation between the X-ray response map, the WXDT image and the IR collapsed image for a CZT sample. The extended defects can be identified with all the three techniques.

picture is acquired in reflection geometry, with a white X-ray beam with energy up to 50 KeV. The penetration depth is about 50 μm. In the WXDT image is not possible to identify Te inclusions and single dislocation are difficult to locate because of the reduced dimensions, however, dislocations arranged in groups can be seen. In figure 5.29 grain and subgrain boundaries are present in the two images, these are the most common defects in CZT samples, beside Te inclusions. From the comparison of a different sample, shown in figure it possible to notice a different behavior in the charge collection degradation, if the defect is not heavily decorated by Te inclusions the degradation effect is lower. In figure 5.34 this effect is shown, the vertical twin, crossing almost the entire sample and clearly identified in the WXDT is affecting the X-ray response map in a relatively small way, with respect to the grain boundary in the upper part of the image.

The grain boundary is strongly decorated with Te inclusions. The upper part of the WXDT shows a very distorted region corresponding to the presence of the grain boundary and a big degradation of the response. The distortion around the twins is instead not present and the degradation is limited to the twin walls.

CHAPTER 6

Conclusions

CZT has emerged as a very promising material in the realization of a RT X-ray detector technology able to move from a strict research environment to the industrial world. The study presented in this work is a complete summary of the state of art for the CZT detectors produced at IMEM. The work includes the use of several techniques, very different each other, for the analysis of both the material and the device properties. Considering the large number of samples studied the material and the device technology has been performed. The aim of this thesis is to acquire a large amount of information from different techniques and then correlate together all the information with the crystal growth in order to create a feedback between the observed properties and the growth technology.

The first part of the thesis is focused on the study of the ingot homogeneity. The near band gap emission is related to the Zn concentration, being the energy gap of the material dependent on the Zn content and the temperature. At a fixed temperature the Zn profile can be extracted from the PL spectrum. The Zn profiles obtained showed an anomalous behavior in the first to freeze part. In the early stage of crystallization Zn content does not follow the normal freeze equation, instead of a monotone decrease from the tip to the bottom of the crystal, the Zn concentration increase for the first 2 centimeters and then follow the normal freeze equation decreasing monotonically. This particular shape of the curve is however pretty common in the literature, several publications from different groups report the same behavior for the Zn profile. This particular feature of the Zn profile is commonly ascribed as an effect of the supercooling

occurring in the first stages of the growth. After a careful analysis several considerations lead to a discard of this explanation in favor of a poor control of the nucleation site inside the ampoule. The growth does not start from the tip but, most likely from the ampoule walls and then proceeds in both directions toward the tip and the bottom of the ingot, this means that usually crystal growers have not a strong control on the nucleation during the growth of CZT by the Bridgman technique.

The second information obtained from the PL map is the growth interface shape. The lines that connect the point in the map with the equal content of Zn represent also the interface at a given point inside the ingot. It was found that the presence of Boron during the growth produces a convex or concave interface. Moreover the influence of a quartz disk on the top of the melt was found to influence the shape of the growth interface. The growth interface can hence be controlled to produce the convex interface, preferred because it helps the single crystal growth. The study of the material properties comprehends also the WXDT, white X-ray diffraction topography. It consist in the irradiation of the sample with a white synchrotron X-ray beam with energies up to 50 KeV and the acquisition of the diffracted spots on a X-ray sensitive film. This technique shows the presence of extended defects inside the samples. The presence of such defects can profoundly affect the detector response, in this work it was shown how in the near defect area the detector response is completely canceled. The identification of grain boundaries or twins is therefore fundamental in the selection of the part of the wafer to be dedicated to the realization of high performance detectors. In IMEM sample WXDT shows the presence of subgrain, grain boundaries and twins. The presence of Te inclusions can instead be checked with IR microscopy. Several images of IMEM samples were acquired giving an accurate reconstruction of the 3D distribution of inclusions and calculating the Te inclusions concentration and size distribution. The maximum size of the inclusions decreased during these years starting from 30 μm in the oldest ingots, but decreasing down to 10-15 μm. The concentration was decreased as well.

The second part of the thesis is focused on the study of the devices in order to characterize the material. The sample are cut, polished and prepared for the contact deposition. Two different deposition techniques were used, in both cases the electrode metal was Au. The metal-semiconductor interface was studied by means of RBS and XRF, combining the results the thickness of the deposited gold layer and the extension of the damaged layers under the electrodes was

studied. The damaged layer was found to be much larger in the case of the electroless deposition with respect to the thermal evaporation. The quality of the deposited metalization was firstly studied measuring the current-voltage characteristic. This measurement is particularly important because from the low current region of the curve it can be calculated the resistivity value, that is impossible to measure with standard techniques, like Van der Pauw method. The studied ingots are all high resistivity with values above 10^{10} Ω cm. The quality of the metal-CZT interface was studied by means of the Pockels effect. With this technique the electric field profile can be detected, with a correlation to the birefringence of the material. The electric field profiles obtained for IMEM samples showed a very good uniformity and a strong dependence of this value on the intensity of the impinging light. This latter fact suggest the presence of a deep level inside the energy gap.

The transport properties were studied, the $\mu\tau$ product was calculated by fitting the shift of the alpha particle emission as a function of the applied bias with the Hecht equation. The obtained values are in the range between 2 and 6 10^{-3} cm^2/V for the electrons. The $\mu\tau$ product value was strongly improved during the PhD period, due to a particualr attention on the purity of the starting material. The $\mu\tau$ product for holes was calculated from the complete Hecht equation and it's estimated to be 10^{-5} cm^2/V. This value is in agreement with the expected limited mobility of holes. The spectroscopic response of the material was studied with several X-ray source. The study was carried out with ^{241}Am, ^{109}Cd, ^{57}Co and ^{133}Ba. The detector showed a good spectroscopic behavior up to 400 KeV and a high reproducibility of the good results in a large number of samples.

The spectroscopic response of the device was also studied using the X-ray microscale mapping. With this technique the sample response can be detected with collimation down to 10 x 10 μm. The maps showed in this work were acquired with a 20 x 20 μm resolution and using a 25 KeV synchrotron X-ray emission. The corresponding map showed a good homogeneity of IMEM samples and a strong reproducibility of the good results. Almost all the samples analyzed at the beamline showed a good response. The technique allows also the identification of defects as the degradation effect connected with their presence is showed in the map. The most interesting results were obtained from the correlation of the measurements with different techniques on the same samples. The comparison between the X-ray microscale map, the WXDT and the IR image allowed to set a direct correlation between the defect and the

damage occurring in the charge collection. During this work several samples and ingots were tested leading to the understanding of some of the mechanisms involved in the realization of CZT radiation detector devices, with a particular attention to the crystal growth related problems.

CHAPTER 7

Appendix

7.1 SURECA ASI Flight Campaign June 2010 (Svalbard)

The detector group took part to The SURECA ASI flight campaign, producing a CZT prototype with IMEM material. The SURECA-BIT-IO campaign is an Italian stratospheric balloon project funded and managed by the Italian Space Agency (ASI).The purpose of SURECA-BIT-IO flight was to test a new Iridium based telemetry system called BIT (Bidirectional Iridium Telemetry) and to perform scientific measurements with a scientific instrument package based on CZT . The main purposes of the flight of the CZT system are to determine the count rate from 30 to several hundred KeV of X- and gamma rays and charged particles as a function of latitude, longitude and altitude and to verify the performance and the robustness of CZT sensors developed entirely with Italian technology in a pseudo space environment and to assess their suitability for the realization of space compact radiation monitors. The CZT sensor module (figure 7.1) has successfully flown from Svalbard to Canada in 4 days (17-20 June 2010) during the ASI flight campaign. During the flight this system was able to record the background count rate profile of both particles and photons (40-400/500 KeV) at arctic latitudes for several hours (about 28 hours) along all the balloon orbit and it has continued to accumulate data on the on PC-104 on board compact flash also after landing for about 16 hours.

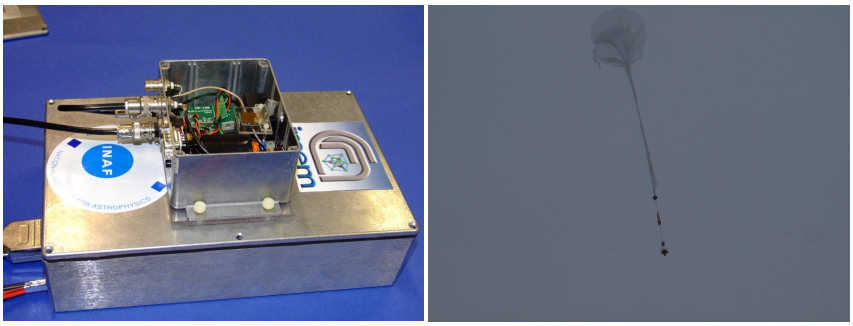

Figure 7.1: CZT sensor module and the SURECA stratospheric ballon during the flight.

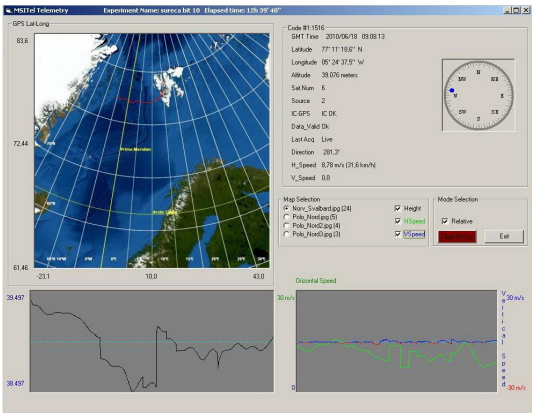

Figure 7.2: Data acquisition during the SURECA flight campaign

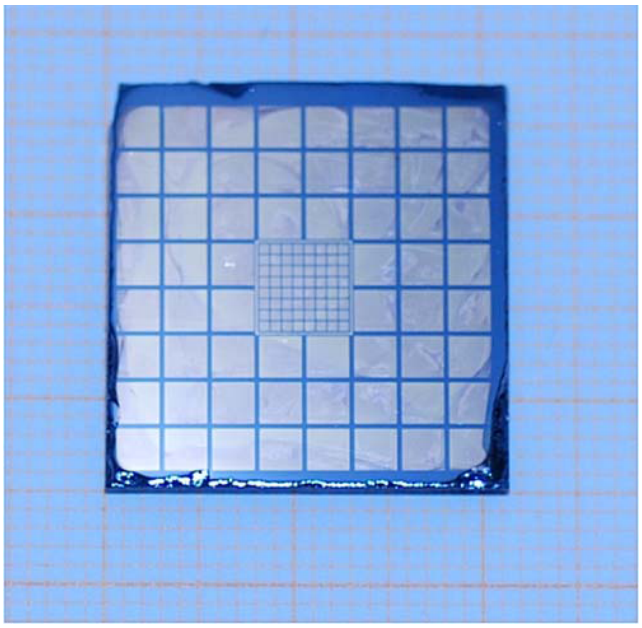

Figure 7.3: The geometry studied for the experiment and the corresponding Compton prototype

7.2 High efficiency Compton module with low instrumentation noise based on innovative techniques for the γ ray detection from the space

The project consisted in the realization of a CZT device with a pultipixel configuration made with spectroscopic grade IMEM material. The sample is a large area detector, the dimensions of the prototype are 25 x 25 mm, the thickness is 2 mm. The contact geometry has been optimized for the technological application: two pixel sizes are chose a central part with 500 μm pixels and a surrounding part with 2.2 mm pixels in order to evaluate the detector response on two different scales. The used geometry is shown in figure 7.3.

Between the inner small pixel and the larger ones there is a guard ring. The spectroscopic characteristics of the material used for the realization of the prototype were previously studied on a wafer cut next to it. The $\mu\tau$ value was 2 10^{-3} cm^2/V, the FWHM of the 60 KeV for the Am source was 5%. The energy resolution of the spectra acquired for this material is very good, especially in the low energy region, with a very low noise.

7.3 Publication List

7.3.1 ISI publications

- M.Zha, A.Zappettini, D.Calestani, L.Marchini, L.Zanotti e C.Paorici *Full-encapsulated CdZnTe crystals by the vertical Bridgman method*, Journal of Crystal Growth, vol 310, pp. 2072-2075

- L. Marchini, A. Zappettini, E. Gombia, R. Mosca, M. Pavesi *Study of Surface Treatment Effects on the Metal-CdZnTe Interface*,IEEE Transactions on nuclear science, vol 56, pp.1823-1826

- A.Zappettini, M.Zha, L.Marchini, D.Calestani, R.Mosca, E.Gombia, L.Zanotti, M.Zanichelli, M.Pavesi, N.Auricchio, E.Caroli *Boron Oxide Encapsulated Vertical Bridgman Grown CdZnTe Crystals as X-ray Detector Material*, IEEE Transactions on nuclear science paper number 101109/TNS.2009.2016964

- M.Zanichelli, M.Pavesi, A.Zappettini, L.Marchini, M.Manfredi *Characterization of Bulk and Surface Transport Mechanisms by means of the Photocurrent Technique*, IEEE Transactions on nuclear science, vol 56, pp. 3591-3596

- J.K. Polack, M.Hirt, J.Sturgess, N.D.Sferrazza, A.E.Bolotnikov, S.Babalola, G.S.Camarda, Y. Cui, S.U.Egarievwe, P.M.Fochuk, R.Gul, A.Hossain, K.Kim, O.V.Kopach, L.Marchini, G. Yang, L.Xu, R.B.James *Variation of electric shielding on virtual Frisch-grid detectors*, Nuclear Instruments and Methods in Physics Research A, A 621, pp. 424-430

- N.Zambelli, L.Marchini, M.Zha, A.Zappettini *Three-dimensional mapping of tellurium inclusions in CdZnTe crystals by means of improved optical microscopy*, in press, Journal of Crystal Growth

- L.Marchini, N.Zambelli, G.Piacentini, M.Zha, D.Calestani, E. Belas, A.Zappetti *Characterization of CZT crystals grown by the Boron Oxide Encapsulated Vertical Bridgman technique for the preparation of X-ray imaging detectors*, in press, Nuclear Instruments and Methods in Physics Research A

- G.S. Camarda, K.W. Andreini, A.E. Bolotnikov, Y. Cui, A. Hossain, R. Gul, K.-H. Kim, L. Marchini, L. Xu,G. Yang, J.E. Tkaczyk, R.B. James *Effect of extended defects in planar and pixelated CdZnTe detectors* , in press, Nuclear Instruments and Methods in Physics Research A

- N. Auricchio, L. Marchini, E. Caroli, A. Cola, I. Farella, A. Donati, A. Zappettini *Spectroscopic response of CZT detectors obtained by the boron oxide encapsulated vertical Bridgman method*, accepted, IEEE Transactions on nuclear science

7.3.2 Conference records

- M.Pavesi, M.Zanichelli, E.Gombia, R.Mosca, L.Marchini, M.Zha, A.Zappettini, E.Caroli, N.Auricchio, B.Negri *CZT X-ray detectors obtained by the boron encapsulated vertical Bridgman method*, Hard X-Ray and Gamma-Ray Detector Physics IX Conference Proceedings, Proc. SPIE, Vol. 6706,(2007), paper number 6706-32

- L.Marchini, A.Zappettini, E.Gombia, R.Mosca, M.Pavesi "Study of Surface Treatment Effects on the Metal-CdZnTe Interface" published in"2008 IEEE Nuclear Science Symposium Conference Record" , paper number: R12-68

- A.Zappettini, M.Zha, L.Marchini, D.Calestani, R.Mosca, E.Gombia, L.Zanotti, M.Zanichelli, M.Pavesi, N.Auricchio, E.Caroli *Boron Oxide Encapsulated Vertical Bridgman Grown CdZnTe Crystals as X-ray Detector Material*, 2008 IEEE Nuclear Science Symposium Conference Record, paper number : R05-1

- M.Zanichelli, M.Pavesi, A.Zappettini, L.Marchini, M.Manfredi *Characterization of Bulk and Surface Transport Mechanisms by means of the Photocurrent Technique*, 2008 IEEE Nuclear Science Symposium Conference Record, paper number: R12-12

- N. Auricchio, L. Marchini, E. Caroli, A. Donati, A. Zappettini,M. Zanichelli, M. Quadrini. *Spectroscopic response of CZT detectors obtained by the boron encapsulated vertical Bridgman method*, 2008 IEEE Nuclear Science Symposium Conference Record, paper number: R12-30

- K. H. Kim, A. E. Bolotnikov, G. S. Camarda, L. Marchini, G. Yang, A. Hossain, Y. Cui, L. Xu, and R. B. James *Detector Performance of Ammonium-Sulfide-Passivated CdZnTe and CdMnTe Materials*, Hard X-Ray, Gamma-Ray, and Neutron Detector Physics XII, Proc. SPIE vol. 7805 (2010)

- L. Xu, A. E. Bolotnikov, A. Hossain, K-H. Kim, R. Gul, G. Yang, G. S. Camarda, L. Marchini, Y. Cui, R. B. James, Y. Xu, T. Wang, W. Jie

Extended defects in as-grown CdZnTe, Hard X-Ray, Gamma-Ray, and Neutron Detector Physics XII, Proc. SPIE vol. 7805 (2010)

- L.Marchini, A.Zappettini, M.Zha, N.Zambelli, A. Bolotnikov, G. Camarda, R.B. James, *Crystal defects and Charge Collection efficiency in CZT X-Ray and gamma detectors*, 2010 IEEE Nuclear Science Symposium Conference Record paper number R02-05

Bibliography

[1] F. Zanio, *Semiconductors and Semimetals*, Academic Press (1978)

[2] M. Fiederle, A. Fauler, J. Konrath, V. Babentsov, J. Franc and R. B. James, *Comparison of undoped and doped high resistivity CdTe and (Cd,Zn)Te detector Crystals* Nuclear Science, IEEE Transactions on, 51, 1864 (2004)

[3] M. L. Cohen and J. R. Chelirowsky, *Electronic and Optical properties of Semiconductors* (Springer, New York, 1988)

[4] B. K. Ridley, *Quantum processes in Semiconductors*, (Oxford University Press, 1982)

[5] J. Singh, *Physics of Semiconductors and their Heterostuctures*, (McGraw-Hill, New York, 1993)

[6] J. A. Van Vechten and T. K. Bergstresser, *Electronic Structures of Semiconductor Alloys*, Phys. Rev. B, 1, 3351 (1970)

[7] D. Kranzer, *Hall and drift mobility of polar p-type semiconductors. II. Application to ZnTe, CdTe, and ZnSe*, Journal of Physics C: Solid State Physics, 6, 20, 2977(1973)

[8] J.s Steininger, A. J. Strauss and R. F. Brebrick, *Phase Diagram of the Zn-Cd-Te Ternary System*, J. Electrochem. Soc., 32, 3866 (1970)

[9] T. Yu and R. Brebrick, *The Hg-Cd-Zn-Te phase diagram*, Journal of Phase Equilibria, 13, 476 (1992)

[10] N. Peyghambarian, S. W. Koch and A.Msyrowicz, *Introduction to Semiconductor Optics* (Prentice hall, 1993)

[11] P. Plumelle and R. Vandevyver, *Lattice Dynamics of ZnTe and CdTe*, Physica status solidi (b), 73, 271 (1976)

[12] J. M. Rowe, R. M. Nicklow, D. L. Price and K. Zanio, *Lattice dynamics of cadmium telluride*, Phys. Rev. B, 10, 671 (1974)

[13] C. Paorici and L. Zanotti, *La tecnologia di crescita dei semiconduttori monocristallini. La crescita da fuso* (Wiley, 1973)

[14] F. Seitz, *Imperfections in nearly Perfects Crystal* (Wiley, 1952)

[15] M. Fiederle, C. Eiche, M. Salk, R. Schwarz, K. W. Benz, W. Stadler, D. M. Hofmann and B. K. Meyer, *Modified compensation model of CdTe*, J. of Appl. Phys., 84, 6689 (1998)

[16] M. Schieber, R.B. James and T.E. Schlesinger, *Semiconductors for Room Temperature Nuclear Detector Applications* (Elsevier, 1995)

[17] M. Zha, F. Bissoli, A. Zappettini, G. Zuccalli, L. Zanotti and C. Paorici, *Heat treatment in semi-closed ampoule for obtaining stoichiometrically controlled cadmium telluride*, Journal of Crystal Growth, 237, 1720 (2002)

[18] A. Zappettini, M. Zha, M. Pavesi and L. Zanotti, *Boron oxide fully encapsulated CdZnTe crystals grown by the vertical Bridgman technique*, Journal of Crystal Growth, 307, 283 (2007)

[19] S. Jain, *Photoluminescence study of Cadmium Zinc Telluride*, Master Thesis, West Virginia University, (2001)

[20] T. E. Schlesinger, J. E. Toney, H. Yoon, E. Y. Lee, B. A. Brunett, L. Franks and R. B. James, *Cadmium zinc telluride and its use as a nuclear radiation detector material*, Materials Science and Engineering: R: Reports, 32, 103 (2001)

[21] J. E. Toney, B. A. Brunett, T. E. Schlesinger, J. M. Van Scyoc, R. B. James, M. Schieber, M. Goorsky, H. Yoon, E. Eissler and C. Johnson, *Uniformity of $Cd_{1-x}Zn_xTe$ grown by high-pressure Bridgman*, Nuclear Instruments and Methods in Physics Research Section A: Accelerators, Spectrometers, Detectors and Associated Equipment, 380, 132 (1996).

[22] J. M. Francou, K. Saminadayar and J. L. Pautrat, *Shallow donors in CdTe*, Phys. Rev. B, 41, 12035 (1990).

[23] E. Molva, J. L. Pautrat, K. Saminadayar, G. Milchberg and N. Magnea, *Acceptor states in CdTe and comparison with ZnTe. General trends*, Phys. Rev. B., 30, 3344 (1984).

[24] B. Henderson and G.F. Imbusch, *Optical Spectroscopy of Inorganic Solids* (Clarendon Press, 1982).

[25] R.E. Halsted, M.R. Lorenz and B. Segall, *Band edge emission properties of CdTe*, Journal of Physics and Chemistry of Solids, 22, 109 (1961).

[26] A. R. Lang, *Techniques and Interpretation in X-Ray Topography*, Diffraction and Imaging Techniques in Material Science, 2, 623 (1978).

[27] B.K. Tanner, *High resolution X-ray diffraction and topography for crystal characterization*, Journal of Crystal Growth, 99, 1315 (1990)

[28] A. Authier, S. Lagomarsino and B.K. Tanner, *X-ray and Neutron Dynamical Diffraction: Theory and Applications*, NATO ASI Series (1996)

[29] P. Rudolph, A. Engel, I. Schentke and A. Grochocki, *Distribution and genesis of inclusions in CdTe and (Cd,Zn)Te single crystals grown by the Bridgman method and by the travelling heater method*, Journal of Crystal Growth, 147, 297 (1995)

[30] R. J. Pieper and A. Korpel, *Image processing for extended depth of field*, Applied Optic, 10, 1449 (1983)

[31] A.E. Bolotnikov, N.M. Abdul-Jabbar, O.S. Babalola, G.S. Camarda, Y. Cui, A.M. Hossain, E.M. Jackson, H.C. Jackson, J.A. James, K.T. Kohman, A.L. Luryi and R.B. James, *Effects of Te Inclusions on the Performance of CdZnTe Radiation Detectors* IEEE Transaction on Nuclear Science, 55, 2757 (2008)

[32] N.Zambelli, *Sviluppo di uno strumento per la rivelazione tridimensionale delle inclusioni di tellurio in cristalli di CZT*, Master Thesis, University of Parma (2010)

[33] A.E. Bolotnikov, G.S. Camarda, G.A. Carini, Y. Cui, L. Li and R.B. James, *Cumulative effects of Te precipitates in CdZnTe radiation detectors*, Nuclear Instruments and Methods in Physics Research Section A, 571, 687 (2007)

[34] D.J. William, *Narrow Gap Cadmium Based Compounds*, INSPEC,(1994)

[35] W.Sang, K. Wang, J. Min, J. Teng, Q. Zhang, Y. Qian, *A novel two-step chemical passivation process for CdZnTe detectors*, Semiconductor Science and Technology, 20, 343 (2005)

[36] K.-T. Chen, D.T. Shi, H. Chen, B. Granderson, M.A. George, W.E. Collins, A. Burger and R.B. James, *Study of oxidized cadmium zinc telluride surfaces*, Journal of Vacuum Science Technology A, 15, 850 (1997)

[37] S. M. Johnson and S. Sen and W. H. Konkel and M. H. Kalisher, *Optical techniques for composition measurement of bulk and thin-film* $Cd_{1-y}Zn_yTe$, Journal of Vacuum Science and Technology B, 9, 1897 (1991)

[38] M. Roumie, M. Hageali, K. Zahraman, B. Nsouli and G. Younes, *Characterization of electroless Au, Pt and Pd contacts on CdTe and ZnTe by RBS and SIMS techniques*, Nuclear Instruments and Methods in Physics Research Section B, 219-220, 871 (2004)

[39] G. W. Wright, R. B. James, D. Chinn, B. A. Brunett, R. W. Olsen, J. M. Van Scyoc III, W. M. Clift, A. Burger, K. Chattopadhyay, D. T. Shi and R. C. Wingfield, *Evaluation of* NH_4F/H_2O_2 *effectiveness as a surface passivation agent for* $Cd_{1-x}Zn_xTe$ *crystals*, SPIE Hard X-Ray, Gamma-Ray, and Neutron Detector Physics II, 4141, 324 (2000)

[40] Q. Li and W. Jie, *Surface passivation and electrical properties of p - CdZnTe crystal*, Semiconductor Science and Technology, 21, 72 (2006)

[41] M. Prokesch and C. Szeles, *Accurate measurement of electrical bulk resistivity and surface leakage of CdZnTe radiation detector crystals*, Journal of Applied Physics, 100, 14503 (2006)

[42] R. Stibal, J. Windscheif and W. Jantz, *Contactless evaluation of semi-insulating GaAs wafer resistivity using the time-dependent charge measurement*, Semiconductor Science and Technology, 6, 995 (1991)

[43] S. M. Johnson, S. Sen,W.H. Konkel, M.H. and Kalisher, *Optical techniques for composition measurement of bulk and thin film* $Cd_{1-y}Zn_yTe$, Journal of Vacuum Science Technology B, 9, 1897 (1991)

[44] W.G. Pfann *Techniques of Zone Melting and Crystal Growing*, SOlid State Physics, Academic Press (1957)

[45] L. L. Zheng and D. J. Larson *Thermoelectric effects on interface demarcation and directional solidification of bismuth*, Journal of Crystal Growth, 180, 293 (1997)

[46] V. Babentsov, J. Franc, A. Fauler, M. Fiederle and R.B. James, *Distribution of zinc, resistivity, and photosensitivity in a vertical Bridgman grown $Cd_{1-x}Zn_xTe$ ingot*, Journal of Crystal Growth, 310, 3482 (2008)

[47] V. Carcelen, N.Vijayan, E.Dieguez, A.Zappettini, M.ZHa, L.Sylla, A. Fauler and M. Fiederle, *New approaches to enlarge the grain size of bulk CdZnTe(CZT) crystals*, Journal of Optoelectronics and advanced materials, 10, 3135 (2008)

[48] A. Cola, I. Farella, A. M. Mancini, W. Dusi and E. Perillo, *Electric field distribution and charge transport properties in diode-like CdTe X-ray detectors*, Nuclear Instruments and Methods in Physics Research Section A, 568, 406 (2006)

[49] L. Marchini, N. Zambelli, G. Piacentini, M. Zha, D. Calestani, E. Belas and A. Zappettini, *Characterization of CZT crystals grown by the boron oxide encapsulated vertical Bridgman technique for the preparation of X-ray imaging detectors*, Nuclear Instruments and Methods in Physics Research Section A, In Press, Corrected Proof (2010)

[50] A. Cola, I. Farella, N. Auricchio and E. Caroli, *Investigation of the electric field distribution in x-ray detectors by Pockels effect*, Journal of Optics A, 8, 467 (2006)

[51] P.F. Fontein, P. Hendriks, F.A.P. Blom, J.H. Wolter, L.J. Giling and C.W.J. Beenakker *Spatial potential distribution in $GaAs/Al_xGa_{1-x}As$ heterostructures under quantum Hall conditions studied with the linear electro-optic effect*, Surface Science, 263, 91 (1992)

[52] A. Tanaka, Y. Masa, S. Seto and T. Kawasaki, *Zinc and selenium co-doped CdTe substrates lattice matched to HgCdTe*, Journal of Crystal Growth, 94, 166 (1989)

[53] K. Suzuki, S. Seto, S. Dairaku, N. Takojima, T. Sawada and K. Imai, *Drift Mobility and Photoluminescence Measurements on High Resistivity Cd1-xZnxTe Crystals Grown from Te-Rich Solution*, Journal of Electronic materials, 25, 1241 (1996)

[54] P.Capper *Segregation of Zn and Se in CdTe*, Properties of Narrow Gap Cadmium based Compounds, 501 (1994)

[55] L. Marchini, A. Zappettini, E. Gombia, R. Mosca, M. Lanata and M. Pavesi, *Study of Surface Treatment Effects on the Metal-CdZnTe Interface*, IEEE Transactions on Nuclear Science, 56, 1823 (2009)

[56] S. Adachi and T. Kimura, *Refractive index dispersion in ZnCdTe ternary alloys*, Journal of Applied Physics, 32, 3866 (1993)

[57] A. Many, *igh-field effects in photoconducting cadmium sulphide*, Journal of Physics and Chemistry of Solids, 26, 575 (1965)

[58] K.Hecht, *Zum Mechanismus des lichtelektrischen Primaerstromes in isolierenden Kristallen*, Zeitschrift fuer Physik A Hadrons and Nuclei, 77, 235 (1932)

[59] J.D.Wiley, *Polar Mobility of Holes in III-V Compounds*, Phys. Rev. B, 4, 2485 (1971)

[60] J. Toney, PhD thesis, Carnegie Mellon University (1998)

[61] A. Zappettini, F. Bissoli, L. Zanotti, M. Zha, C. Broglia and C. Paorici, *Stoichiometric deviations and partial-pressure measurements in solid-vapour cadmium telluride system*, Materials Chemistry and Physics, 66, 138 (2000)

[62] R. Grill and A. Zappettini, *Point defects and diffusion in cadmium telluride*, Progress in Crystal Growth and Characterization of Materials, 48-49, 209 (2004)

[63] U. Becker and P. Rudolph and R. Boyn and M. Wienecke and I. Utke, *Characterization of p-Type CdTe Bridgman Crystals by Infrared Extinction Spectra*, Physica status solidi (a), 1209, 653 (1990)

[64] L. Marchini, *Cristalli di CdZnTe per la rivelazione dei raggi X*, Master thesis, University of Parma (2007)

[65] M. A. George, W.E. Collins, K.T. Chen, Z. Hu, S.U. Egarievwe, Y. Zheng and A. Burger, *Study of electroless Au film deposition on ZnCdTe crystal surfaces*, Journal of Applied Physics, 77, 3134 (1995)

[66] J. G. Werthen, J.-P. Haring, A. L. Fahrenbruch and R. H. Bube, *Effects of surface preparation on the properties of metal/CdTe junctions*, Journal of Applied Physics, 54, 5982 (1983)

[67] I.M. Dharmadasa, J.M. Thornton and R.H. Williams, *Effects of surface treatments on Schottky barrier formation at metal n CdTe contacts*, Applied Physics Letters, 54, 137 (1989)

[68] G. W. Wright, G. Camarda, E. Kakuno, L. Li, F. Lu, C. Lee, A.Burger, J. I. Trombka, D. P. Siddons and R. B. James, *Effects of surface roughness on large-volume CdZnTe nuclear radiation detectors and removal of surface damage by chemical etching*, SPIE Hard X-Ray and Gamma-Ray Detector Physics V, 5189, 306 (2004)

[69] D.De Nobel, Philips Res. Repts.,14, 361 (1959)

[70] A.Raulo, L.Marchini, G.Paternoster, E.Perillo, P.Paiano, A.M.Mancini, M.Zha and A.Zappettini, *Ion Beam (RBS) and XRF Analysis of Metal Contacts Deposited on CdZnTe and CdTe Crystals*, IEEE Nuclear Science Symposium Conference records (2010)

[71] L.J.van der Pauw, *A method of measuring specific resistivity and Hall effect of discs of arbitrary shape*, Philips Res. Repts., 13 (1958)

[72] M.Muehlberg, P.Rudolph, C.Genzel, B.Wermke and U.Becker, *Crystalline and chemical quality of CdTe and $Cd_{1-x}Zn_xTe$ grown by the Bridgman method in low temperature gradients*, Journal of Crystal Growth, 101 (1990)

[73] Y.Xu, W.Jie, P.Sellin, T.Wang, L.Fu, G.Zha and PVeeramani, *Characterization of CdZnTe Crystals Grown Using a Seeded Modified Vertical Bridgman Method*, IEEE Tansaction on Nuclear Science, 56, 2808 (2009)

[74] M.Azoulay, S.Rotter and G.Gafni, *Zinc segregation in CdZnTe grown under Cd/Zn partial pressure control*, Journal of Crystal growth, 117, 276 (1992)

[75] P.N.Luke, *Unipolar charge sensing with coplanar electrodes-application to semiconductor detectors* Tansaction on Nuclear Science, 42, 207 (1995)

[76] Y.Eisen and A.Shor, *CdTe and CdZnTe materials for room-temperature X-ray and gamma ray detectors*, Journal of Crystal growth, 184-185, 1302 (1998)

[77] G.S. Camarda, A. E. Bolotnikov, Y. Cui, A. Hossain, S.A. Awadalla, J. Mackenzie, H.Chen and R.B. James, *Polarization Studies of CdZnTe Detectors Using Synchrotron X-Ray Radiation*, IEEE Transactions on Nuclear Science, 55, 3725 (2008)

[78] A.Musa, J.P.Ponpon, J.J. Grob, M.Hage-Ali, R.Stuck and P.Siffert, *Properties of electroless gold contacts on p-type cadmium telluride*, Journal of Applied Physics, 54, 289 (1983)